Universiteit
Leiden
The Netherlands

# The first steps of planet formation : studying grain growth with millimetre interferometers

Lommen, D.J.P.

**Citation**
Lommen, D. J. P. (2009, April 23). *The first steps of planet formation : studying grain growth with millimetre interferometers*. Retrieved from https://hdl.handle.net/1887/13752

| | |
|---|---|
| Version: | Corrected Publisher's Version |
| License: | Licence agreement concerning inclusion of doctoral thesis in the Institutional Repository of the University of Leiden |
| Downloaded from: | https://hdl.handle.net/1887/13752 |

**Note:** To cite this publication please use the final published version (if applicable).

# The first steps of planet formation

## Studying grain growth with millimetre interferometers

# The first steps of planet formation
## Studying grain growth with millimetre interferometers

PROEFSCHRIFT

ter verkrijging van
de graad van Doctor aan de Universiteit Leiden,
op gezag van de Rector Magnificus prof. mr. P. F. van der Heijden,
volgens besluit van het College voor Promoties
te verdedigen op donderdag 23 april 2009
klokke 15.00 uur

door

Dave Jacobus Petronella Lommen
geboren te Grubbenvorst
in 1977

Promotiecommisie

| | | |
|---|---|---|
| Promotor: | Prof. dr. E. F. van Dishoeck | |
| Co-promotores: | Dr. H. J. van Langevelde | |
| | Dr. C. M. Wright | (University of New South Wales, Canberra) |
| Overige leden: | Prof. dr. C. Dominik | (Universiteit van Amsterdam; Radboud Universiteit Nijmegen) |
| | Dr. M. R. Hogerheijde | |
| | Prof. dr. K. Kuijken | |
| | Prof. dr. J. P. Williams | (University of Hawaii) |

There are more things in heaven and earth, Horatio,
Than are dreamt of in your philosophy.
*Hamlet Act 1, scene 5, 159*

# Table of contents


**1 Introduction** **1**

1.1 Star formation . . . . . 1
1.2 Grain growth and planet formation . . . . . 4
1.3 Observing the evolution of young stellar objects . . . . . 7
1.3.1 A classification of young stellar objects . . . . . 7
1.3.2 Observing the growth from submicron to micron sizes with the 10-$\mu$m silicate feature . . . . . 8
1.3.3 Observing the growth from gravel to boulders at long wavelengths . . . . . 9
1.4 Millimetre interferometers . . . . . 10
1.5 This thesis . . . . . 11

**2 SMA observations of young discs: separating envelope, disc, and stellar masses in class I YSOs** **15**

2.1 Introduction . . . . . 16
2.2 Observations . . . . . 18
2.3 Results . . . . . 18
2.3.1 Continuum data . . . . . 18
2.3.2 Line data . . . . . 19
2.4 Discussion and interpretations . . . . . 21
2.4.1 Envelope and disc masses . . . . . 21
2.4.2 Keplerian rotation and stellar masses . . . . . 29
2.5 Conclusions . . . . . 30

**3 Investigating grain growth in discs around southern T-Tauri stars at millimetre wavelengths** **33**

3.1 Introduction . . . . . 34
3.2 Observations . . . . . 36
3.2.1 Source selection . . . . . 36

3.2.2 ATCA observations . . . 36
3.2.3 SMA observations . . . 37
3.3 Results . . . 39
3.3.1 Source fluxes . . . 39
3.3.2 Are the sources resolved? . . . 41
3.3.3 Opacity index . . . 43
3.3.4 Disc masses . . . 48
3.3.5 Molecular line emission . . . 49
3.4 Discussion and interpretations . . . 50
3.4.1 Grain growth . . . 50
3.4.2 Comparison with Spitzer infrared data . . . 50
3.4.3 Comparison with Herbig-Ae/Be stars . . . 51
3.5 Concluding remarks . . . 53

**4 Grain growth across protoplanetary discs: 10-$\mu$m feature versus mm slope 55**
4.1 Introduction . . . 56
4.2 Observations . . . 57
4.2.1 Source selection and Spitzer data . . . 58
4.2.2 SMA observations . . . 60
4.2.3 ATCA observations . . . 60
4.2.4 CARMA observations . . . 61
4.2.5 VLA observations . . . 61
4.3 Results . . . 64
4.3.1 Mm and cm source fluxes and disc masses . . . 64
4.3.2 Millimetre slopes . . . 67
4.3.3 Results from Spitzer infrared observations . . . 68
4.3.4 10-$\mu$m feature vs mm slope . . . 70
4.4 Modelling . . . 76
4.4.1 Disc model parameters and SEDs . . . 76
4.4.2 10-$\mu$m feature vs mm slope . . . 78
4.5 Discussion . . . 82
4.6 Conclusions . . . 85
4.7 Appendix: observations . . . 86
4.8 Appendix: results . . . 91

**5 Large grains in discs around young stars: ATCA observations of WW Cha, RU Lup, and CS Cha** **103**
5.1 Introduction . . . 104
5.2 Observations . . . 107
5.2.1 WW Cha . . . 108
5.2.2 RU Lup . . . 108
5.2.3 CS Cha . . . 108
5.3 Results . . . 110
5.3.1 WW Cha . . . 110
5.3.2 RU Lup . . . 112
5.3.3 CS Cha . . . 114
5.4 Discussion and interpretation . . . 121
5.4.1 WW Cha . . . 121
5.4.2 RU Lup . . . 123
5.4.3 CS Cha . . . 125
5.4.4 Large grains in protoplanetary discs . . . 126
5.5 Conclusions . . . 127

**Bibliography** **129**

**Publicatielijst** **137**

**Nederlandse samenvatting** **139**

**Curriculum vitae** **145**

**Nawoord** **147**

# Chapter 1

# Introduction

The Milky Way contains about 200 billion stars, of which the Sun is only one unremarkable example. We live on Earth, one of eight planets[1] revolving around the Sun in a more or less flat plane. It was suggested a long time ago that our Sun is not the only star with planets (Epicurus 300 B.C.; Bruno 1584). However, it was only at the beginning of the last decade of the twentieth century that a planet outside of our solar system was found (Bailes et al. 1991). This planet is orbiting a neutron star, the remnant of a massive star whose life ended in a supernova, and probably this planet had a very different formation history than our own Earth. In 1995, a planet was discovered around a star more similar to our Sun, 51 Peg (Mayor & Queloz 1995). Since then, more than 300 planets outside our solar system, so-called exoplanets, have been found.

Planets are generally accepted to be the by-products of stars, which are formed when interstellar clouds of gas and dust collapse under the forces of gravity. The details of this formation process are still largely unknown and this thesis is part of the world-wide effort to unravel the secrets of star and planet formation.

## 1.1 Star formation

Between smaller and larger groups of stars, there are clouds of gas and dust permeating the Galaxy, so-called Giant Molecular Clouds (GMCs). These clouds can be stable over periods of millions upon millions of years, with gas pressure and turbulence working against the gravity that might otherwise pull the clouds together. Magnetic fields may also alter the dynamical state of a molecular cloud sufficiently to prevent gravitationally unstable regions from collapsing (Shu et al. 1987). At some point in time, however, these clouds will become unstable and

[1] Pluto was demoted from a planet to a dwarf planet (e.g., Binzel 2006). The eight planets of the solar system are, with increasing distance from the Sun: Mercury, Venus, Earth, Mars, Jupiter, Saturn, Uranus, and Neptune.

start to collapse under their own gravity. This may happen when, for instance, a supernova goes off nearby and sends a pressure wave through the cloud. This may cause the neutral particles in the cloud to decouple sufficiently from the charged particles (ambipolar diffusion, e.g., Mouschovias 1977), so that the support from magnetic fields can be overcome. While hydrodynamical turbulence can perhaps prevent global collapse, it can never completely prevent local collapse (Klessen et al. 2000) and the cloud will start to fragment. Locally within the cloud, the forces of gravity become larger and overcome the gas pressure. Several clumps of material will start to collapse and one GMC may eventually harbour hundreds or even thousands of dark cores, several of which may eventually form stars and planets.

With pressure at least temporarily overcome, the dark core will continue to collapse. However, in every cloud and core a net quantity of angular momentum is present which prevents the core from collapsing spherically symmetrically and a flattened structure must form. Material moves inwards through the structure under the force of gravity while angular momentum moves outwards and thus a disc-like structure with a bulge in the centre is naturally formed. As more and more material falls onto the disc and the central protostar, the system can no longer get rid of the excess angular momentum by moving it outward through the disc. Consequently, possibly in conjunction with the magnetic field present in the disc, jets are formed close to the central structure. These jets eject material from either pole in the system, forming outflow cavities in the surrounding envelope in the process. Thus, while in the outer part of the system material from the envelope is still raining down on the disc, in the centre some of the material is ejected and returned to the interstellar medium. In this phase, the system is an embedded young stellar object, class I in the Lada classification (Lada & Wilking 1984, and below). A schematic picture of a class I object is shown in the top panel of Fig. 1.1.

After several hundred thousand years, the envelope is dispersed and we are left with a young stellar object, consisting of a protostar surrounded by a protoplanetary disc. The temperature in the core of the central object is not yet high enough for the fusion of atomic hydrogen and it derives most of its luminosity from conversion of gravitational potential energy into kinetic energy and hence heat. The disc around it has initially a consistency similar to that of the interstellar medium, implying that some 99% of the mass is gas with the remaining 1% being dust. The dust grains are silicate- and carbon-based and in the colder regions they are covered with icy layers of, e.g., water, carbon dioxide, and methane. They have sizes in the range of 0.003 $\mu$m up to ~0.1 $\mu$m. It is from these tiny grains that

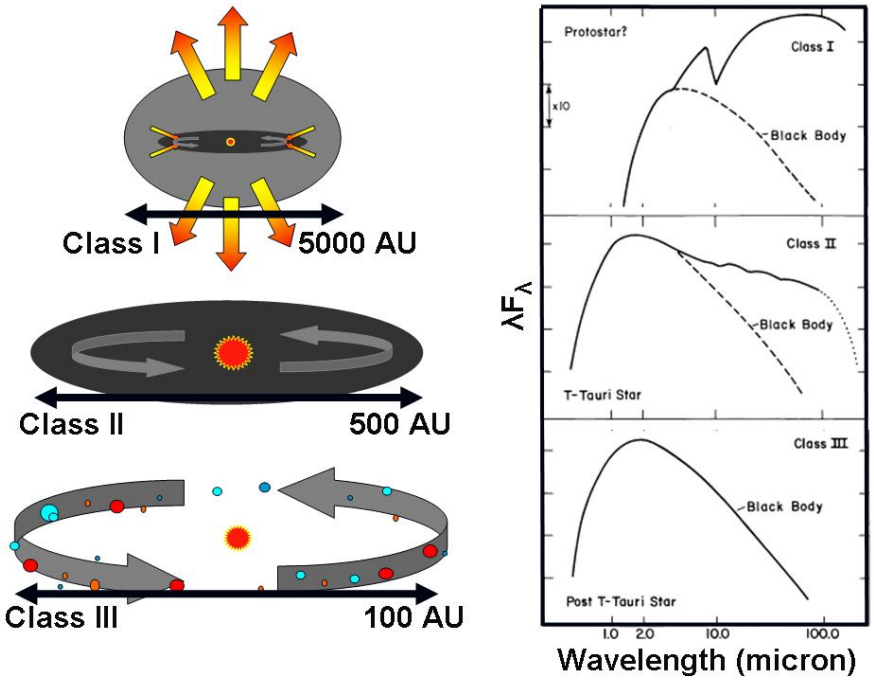


Figure 1.1: An overview of the three so-called Lada classes of star formation (Lada & Wilking 1984). On the left, schematic representations of the geometry of the system are given, in which the protostar, the circumstellar disc, the envelope, and eventually the pre-planetary system can be distinguished. On the right, characteristic spectral energy distributions are shown (see Sect. 1.3.1).

eventually planets are formed. The evolution of a low-mass young stellar object is depicted by a cartoon in Fig. 1.1.

This thesis is mainly concerned with these circumstellar discs in young stellar objects. Using observations and computational models we will address the following questions. When does the disc form? How large is it? When, how fast, and where in the disc do grains grow? Can we test the evolution of envelope, disc, and stellar mass shown in Fig. 1.2 (based on Hueso & Guillot 2005)?

A natural way to describe the structure of a circumstellar disc is through the regions that can be probed with different kinds of observations. Light is very efficiently scattered by small particles and thus we can see circumstellar discs out to large distances from the star through optical and near-infrared scattered light.

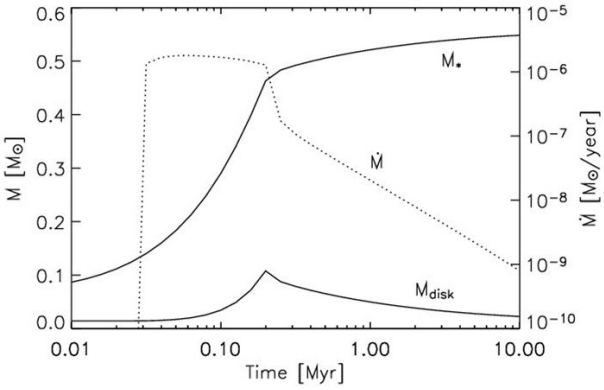


Figure 1.2: Schematic picture of the mass evolution of the disc and the central star (based on Hueso & Guillot 2005). The dotted line shows how the stellar accretion rate changes over time.

However, these observations only graze the disc surface. Mid-infrared images and spectra probe the atmosphere of the disc, but only the warmer regions. These regions may conveniently be called the inner disc, typically located within a few AU from the young star. The outer disc, then, is best studied at (sub)millimetre and centimetre wavelengths. At these wavelengths, most of the emission is optically thin and the bulk of the disc matter can be probed. Finally, a region that cannot be observed directly but is inferred from disc modelling is the so-called "dead zone" in the mid-plane of the inner disc. This is a somewhat quiescent region with less turbulence than elsewhere in the disc. However, it is important in the sense that planetesimals may actually be formed near or in the "dead zone," as we will see below. A schematic picture of a protoplanetary disc with the most important regions is shown in Fig. 1.3.

## 1.2 Grain growth and planet formation

The formation of kilometre-sized planetesimals from what originally are submicron-sized dust grains was studied in the classic work by Weidenschilling (1980) and a comprehensive recent review can be found in Youdin & Johansen (2008). The most important processes involved are described in this Section and summarised in Fig. 1.4.

The first step in the long road from interstellar-sized grains to planets is when

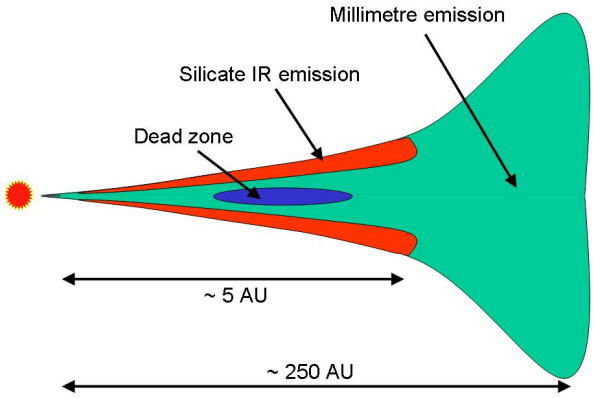


Figure 1.3: A schematic picture of a protoplanetary disc. Indicated are the outer disc, the atmosphere of the inner disc, and the low-turbulence "dead zone." The mid-infrared emission, including the silicate features around 10 and 20 $\mu$m, originates in the atmosphere of the inner disc, while (sub)mm observations basically probe the entire disc. Picture based on a presentation by Carsten Dominik.

grains less than a micron in size grow to sizes of a few microns. The particles will behave in the ensuing gas as smoke in the air: they move in Brownian motion under the influence of the gas molecules and will occasionally collide with each other. Upon collision, two grains will usually stick at the very low relative velocities of a few cm $s^{-1}$ produced by Brownian motion (Dominik & Tielens 1997; Paszun & Dominik 2006; Blum & Wurm 2008). Models and laboratory experiments show that grain growth from interstellar, submicron sizes to particles of several milli- or centimetres in size is straightforward and fast.

Once the particles have reached sizes in the order of centimetres, they become more likely to fragment upon collision (Blum & Wurm 2000). However, it turns out that the largest particles will still grow if collisional charging and electrostatic reaccretion (e.g., Blum 2004; Blum & Wurm 2008) or reaccreation by gas flow (e.g., Wurm et al. 2001; Sekiya & Takeda 2003) are taken into account. In this way the dust grains may grow to decimetres in size.

The growth of objects larger than decimetres in size can as yet not be studied in the laboratory. Furthermore, at these large sizes, the interaction of the particles with the surrounding disc becomes more important and the problem is at-

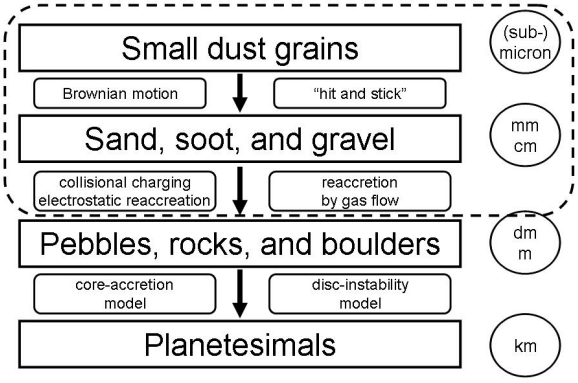


Figure 1.4: An overview of the most important porcesses governing the growth from (sub)micron-sized dust grains to millimetre- and centimetre-sized pebbles, decimetre- and metre-sized boulders, and finally to planetesimals. The dashed line encompasses the grain sizes which are observationally studied in this thesis. Picture based on a presentation by Jürgen Blum.

tacked with numerical models, in which a large part of, or even the whole disc are taken into account. Johansen et al. (2007) formed planetesimals and dwarf planets through gravitational collapse in the mid-plane of turbulent discs. However, they required metre-sized bodies as a starting point for the scenario. Lyra et al. (2008a) started with grains of 1 up to 100 cm and found that these could grow to objects the size of Mars within several thousand years, when trapped in waves at the edge of the quiescent, almost turbulence-free "dead zone" in the centre of protoplanetary discs. A rather more complete picture was subsequently drawn by Brauer et al. (2008a,b), who started with microphysics including Brownian motion, differential settling, and turbulent coagulation (Brauer et al. 2008a) and subsequently formed kilometre-sized bodies near the "snow line" in a few thousand years (Brauer et al. 2008b).

Two competing models exist for the formation of gas giants such as Jupiter and Saturn in our own solar system and most of the planets orbiting other stars found so far. In the core-accretion model (e.g., Safronov & Zvjagina 1969; Goldreich & Ward 1973; Hayashi et al. 1985; Pollack et al. 1996), a heavy-element core is built by the accretion of planetesimals, much as described in the previous paragraph.

As the core becomes more massive, its ability to accrete gas from the surrounding disc increases. At some point the core may become massive enough for rapid accretion of gas and a gas giant is formed. In the disc-instability scenario (e.g., Kuiper 1951; Cameron 1978; Boss 1997), a sufficiently massive disc will fragment into dense cores. These clumps can contract to form gas giants much in the same way as proto-stellar systems are formed from their parental cloud (see previous Section). Though some problems still exist for both scenarios, it is interesting to note that some 90% of the exoplanets found so far can be reasonably well explained with the core-accretion model, while the remaining 10% could have been formed through the disc-instability model (Matsuo et al. 2007).

It thus seems that the processes leading from small grains to large planets are fairly well understood. However, all models will eventually have to be tested against experiments, or in the case of astronomy, observations. The observations of young stellar objects are the subject of the following Section.

## 1.3 Observing the evolution of young stellar objects

### 1.3.1 A classification of young stellar objects

Lada & Wilking (1984) introduced an empirical classification of young stellar objects, based on their spectral energy distributions (SEDs) in the infrared (see Fig. 1.1). The SEDs of class I objects are completely dominated by emission from the circumstellar envelope, which entirely obscures the central star. In class II objects, the envelope has been dispersed and the central star has become visible. A strong excess over the photosphere of the star is still present, though, due to the warm gas in the circumstellar disc. Over time, also the gaseous disc is lost due to accretion processes and photo-evaporation and what is left is an SED which is dominated by the central star and only has a small excess due to the dust in a debris disc. Though this classification has proved extremely useful, it is not foolproof. For example, a system without an envelope that is viewed edge-on may produce a class I SED. Van Kempen et al. (2009) found for a sample of more than 40 young stellar objects in Ophiuchus that were at some point classified as class I objects, that less than half were indeed genuine class I as originally defined in the Lada classification. Different observables have been proposed to determine the evolutionary stage of a young stellar object (e.g., Robitaille et al. 2006) and Crapsi et al. (2008) concluded that one of the best diagnostics to determine whether an object is embedded or not is by comparing the single-dish flux to the interferometric flux at (sub)millimetre wavelengths (see also below).

### 1.3.2 Observing the growth from submicron to micron sizes with the 10-$\mu$m silicate feature

Since new stars are formed from the interstellar medium, the dust composition is initially also the same as that of the interstellar medium. More particularly, the initial dust size distribution is that of the interstellar medium, with a typical size of ~0.1 $\mu$m. Due to coagulation, these dust grains will grow, first to sizes of a few $\mu$m and later to larger sizes, and the high temperature locally in the inner disc will anneal the mostly amorphous grains to more crystalline structures. These very first steps of grain growth can be observed in the infrared, most notably using the silicate features around 10 and 20 $\mu$m. These features can be observed from the ground as was done by, e.g., Meeus et al. (2001) and Przygodda et al. (2003). Over the last several years, a large number of interferometric observations have been obtained in the infrared, in particular using the MIDI instrument (Leinert et al. 2003) operating on the Very Large Telescope (Glindemann et al. 2000) around 10 $\mu$m. Ground-breaking results were obtained by van Boekel et al. (2004), who used MIDI to observe the Herbig-Ae star HD 144432. The observations clearly showed the presence of more crystalline material in the inner disc, whereas the dust in the outer disc was predominantly amorphous. Furthermore, both the change from amorphous to more crystalline grains as well as the growth of submicron sizes to sizes of several microns have been observed by the Infrared Space Observatory (ISO, Malfait et al. 1998; van Boekel et al. 2005). More recently, the Spitzer Space Telescope was used to observe the infrared spectra of many more, also considerably weaker young stellar objects (e.g., Furlan et al. 2006; Kessler-Silacci et al. 2006). A large range of 10-$\mu$m features was observed, ranging from strong, peaked features to weak, flat-topped features. Comparison with synthetic spectra of small grains showed that the different features can be quite naturally explained with grain growth: the 10-$\mu$m feature is strong and peaked for interstellar grains of about 0.1 $\mu$m in size, whereas the feature is largely gone by the time the grains have reached sizes of ~6 $\mu$m (see Fig. 1.5). However, processes other than grain growth have been proposed to explain the evolution of the 10-$\mu$m feature. For example, if large grains settle to the mid-plane, they no longer contribute to the 10-$\mu$m feature, which would thus over time attain the stronger and more peaked shape associated with the smallest grains (Dullemond & Dominik 2008).

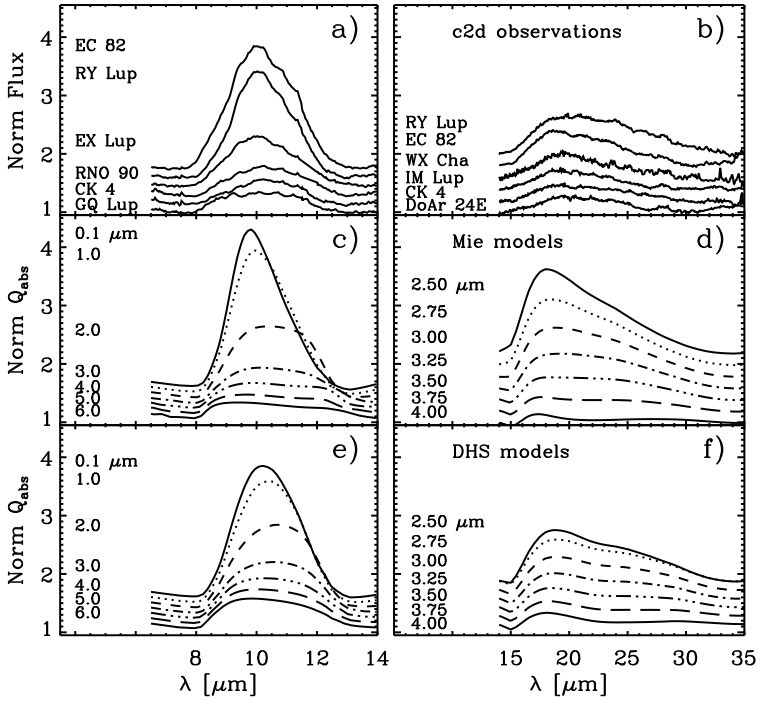


Figure 1.5: The evolution of the 10- and 20-$\mu$m silicate features. *Upper panel*: observations from the Spitzer "c2d" Legacy programm. *Middle panel*: synthetic spectra created using filled homogeneous spheres. *Bottom panel*: synthetic spectra created using a distribution of hollow spheres (from Kessler-Silacci et al. 2006).

### 1.3.3 Observing the growth from gravel to boulders at long wavelengths

Growth to larger sizes can only be observed at longer wavelengths and seminal work on this was done by Beckwith et al. (1990) and Beckwith & Sargent (1991). They observed a large number of young stellar objects at submillimetre (submm) and millimetre (mm) wavelengths with single-dish telescopes and determined the (sub)mm slope of the spectral energy distribution. They found slopes $\alpha \approx 2$, where $F_\nu \propto \nu^\alpha$. The interstellar medium has values around $\alpha = 3.7$ (cf. Draine 2006) and the shallower mm slope found for the dust in circumstellar discs was interpreted as grain growth. Indeed, numerical models of dusty discs predict that the (sub)mm slope becomes shallower when larger grains are included (e.g.,

Dullemond & Dominik 2004a). However, the observed shallow slopes can also be caused by small, optically thick discs. Furthermore, there may be contributions from a (remnant) circumstellar envelope. It is therefore necessary to observe these young systems with interferometers to filter out extended emission and resolve the discs spatially in order to unambiguously attribute the shallow spectral slope to grain growth. This has been done in recent years (e.g., Natta et al. 2004; Rodmann et al. 2006; Andrews & Williams 2007) and several dozen young stellar objects with dust of at least mm sizes have been found. Even larger grains, or pebbles, can only be observed at centimetre wavelengths. However, the detection of thermal emission from dust is notoriously difficult at such long wavelengths where the emission is tailing off and other emission mechanisms such as winds or chromospheric activity may also contribute. Wilner et al. (2005) used the Very Large Array to resolve and monitor the pre-main-sequence star TW Hya and found decimetre-sized pebbles in the disc.

## 1.4 Millimetre interferometers

As explained above, the first steps of planet formation are well observed in the infrared and at (sub)mm and cm wavelengths. Observations have shown that dust is processed in the discs around young stars. The next step is to find out where exactly grain processing or growth is taking place. This requires high-spatial-resolution observations, with which the systems can be spatially resolved. The highest spatial resolution is obtained using the telescopes with the largest dishes or mirrors. However, there are physical limitations to how large a single telescope can be. Higher resolution can then be obtained using the technique of interferometry. With interferometry, an object is simultaneously observed with two (or more) telescopes and the signals of the two telescopes are allowed to interfere, either directly or after digitisation. The information that can be obtained in this way has the same spatial resolution as if one were using a telescope with a diameter as large as the distance between the two telescopes.

Interferometric observations of young stellar objects at mm and cm wavelengths are very useful, because they can resolve the circumstellar discs. As long as a disc is unresolved, it is possible that the spectral slope is affected by a very small, optically thick disc. Only if the emission at (sub)mm wavelengths is optically thin, the flux is a rather direct measure of the disc's mass. Furthermore, (sub)mm interferometry allows us to separate disc emission from envelope emission, as is demonstrated in Fig. 1.6 (from Jørgensen et al. 2005). This Figure shows the flux as a function of baseline length for NGC 1333-IRAS 2. Shorter

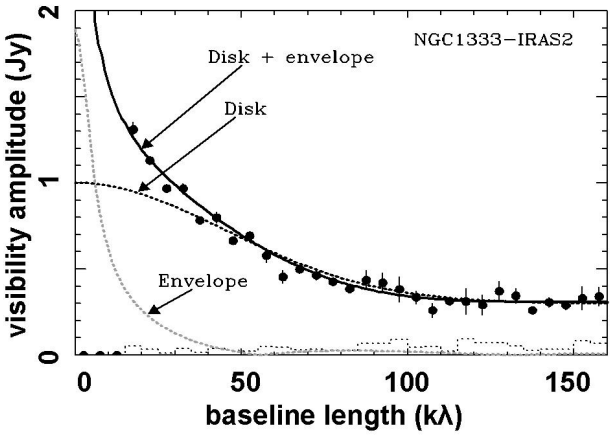


Figure 1.6: The flux as a function of baseline for the embedded young stellar object NGC 1333-IRAS 2, from Jørgensen et al. (2005). Overplotted are the flux due to the circumstellar envelope, constrained by single-dish SCUBA observations (Jørgensen et al. 2002), and the flux due to the resolved circumstellar disc.

baselines probe larger scales and the flux drops towards longer baselines. This can be explained as follows. On the smallest interferometer baselines the telescope has a large beam and the detected flux is that of all the matter included in the beam, in this case the circumstellar disc and the envelope. On the longer baselines the telescope is sensitive to smaller scales and only the flux of the disc is detected. In this way the emission of the disc and that of the envelope can be neatly separated.

## 1.5 This thesis

This thesis is largely aimed at sources in the southern sky and the only mm and cm interferometer that can currently observe the southern-most sources is the Australia Telescope Compact Array (ATCA). We used the ATCA to observe T-Tauri stars in the southern star-forming regions Lupus, Chamaeleon, and Corona Australis at 3 mm and a number of sources at 7 mm, 3.5, and 6.3 cm. The sources in Lupus and Corona Australis were also observed with the Submillimeter Array (SMA) at 1 mm. The SMA is located on Mauna Kea on Hawaii and can still reach several of the star-forming regions in the southern hemisphere. It is also used

to observe two embedded, class I, objects in the $\rho$ Ophiuchi star-forming region. Finally, the more northern Combined Array for Research in Millimeter-wave Astronomy (CARMA) and the Very Large Array (VLA) were used to observe a number of class II objects in Serpens at 1 and 3 mm (CARMA) and at 7 mm, 1.3, 3.6, and 6.2 cm (VLA).

In Chapter 2, we present SMA observations of two embedded sources with young discs. These two young stellar objects were previously classified as class I in the Lada classification. A survey of bright T-Tauri stars in the southern constellations Lupus and Chamaeleon was carried out using the ATCA at 3 mm, the results of which are presented in Chapter 3. The Lupus sources were subsequently observed with the SMA at 1 mm. The results of Chapter 3 were followed up with a larger survey of T-Tauri stars, using the SMA, ATCA, CARMA, and VLA interferometers and the Spitzer Space Telescope in Chapter 4. Finally, in Chapter 5, we show ATCA monitoring observations at centimetre wavelengths of three sources from the sample presented in Chapter 3, allowing us to constrain the physical processes responsible for the emission. RU Lup and WW Cha were the brightest sources in that sample and had fairly shallow millimetre slopes, indicating the presence of large grains.

The main conclusions of this thesis are the following.

- Interferometric observations can separate the discs and envelopes of young stellar objects at (sub)mm wavelengths as well as the objects from their environment. The masses of the envelopes and discs of the class I objects IRS 63 and Elias 29 have been determined, giving ratios of $M_{\rm env}/M_{\rm disc}$ of 0.2 for IRS 63 and 6 for Elias 29. High-spatial-resolution observations of the motion of the molecular gas in the discs are used to determine the masses of the central objects for the first time, $0.37 \pm 0.13$ $M_\odot$ for IRS 63 and $2.5 \pm 0.6$ $M_\odot$ for Elias 29 for a fiducial inclination of 30°, indicating that the central stars have practically reached their final mass (Chapter 2).

- A total of 26 southern discs are detected at mm wavelengths with the SMA, ATCA, and CARMA. Several of these sources are resolved, indicating that the emission is optically thin at these wavelengths. The (sub)mm slope $\alpha$ is determined and found to cluster around 3, where $F_\nu \propto \nu^\alpha$, implying that millimetre-sized grains must be common in the discs of T-Tauri stars (Chapters 3 and 4).

- A correlation is found between the strength of the 10-$\mu$m silicate features and the mm slopes. As the 10-$\mu$m feature probes the surface layers of the inner disc and the mm slope probes the outer disc, this means that

grain growth must be fast throughout the disc. The sources are more or less grouped by star-forming region in the 10-$\mu$m-feature versus mm-slope diagram. Synthetic spectra were created using the radiative-transfer tool RADMC and they show that this grouping can be explained if one assumes that grain growth has progressed further in some of the star-forming regions than in others. However, it may also point to a chemical variation between the different star-forming regions (Chapter 4).

- RU Lup and CS Cha are found to have dust emission up to 7 mm and WW Cha up to 1.6 cm, indicating the presence of pebble-sized grains. Other mechanisms are responsible for the emission at longer wavelengths for RU Lup and WW Cha (Chapter 5).

The study of young stellar objects with (sub)mm and cm interferometers is a relatively young and very exciting field in which many interesting results have been obtained in the past several years. The future of this field is extremely bright. Firstly, the upgrade of the ATCA with the Compact Array Broadband Backend (CABB), which will increase the bandwidth with a factor of 16, is practically finished. This will make surveys of young stellar objects at mm and cm wavelengths in the southern sky much more feasible, which in turn will allow us to obtain the necessary statistics to draw firmer and stricter conclusions. Likewise, the upgrade of the VLA to form the Expanded Very Large Array (EVLA) will increase the continuum sensitivity by a factor of 5 to 20, giving a point-source sensitivity better than 1 $\mu$Jy between 7 mm and 15 cm and accessing the northern skies to similar surveys. The e-MERLIN telescope array, which will provide radio imaging, spectroscopy, and polarimetry with 10-150 milliarcsecond resolution and $\mu$Jy sensitivity at cm wavelengths, is also nearing completion. Next, the Atacama Large Millimeter/submillimeter Array (ALMA) is expected to start operations in a few years time, opening up the southern skies to wavelengths between 0.35 and 3.6 millimeters. The unprecedented spatial resolution at these wavelengths will make it possible to study the growth of grains to pebbles as a function of location in the disc. Finally, the Square Kilometre Array (SKA) is being planned. Construction of the first elements of the SKA is expected to start in 2012, with completion of the array by 2020. The SKA will allow observations at about 1 cm and longer at milliarcsecond resolutions to find rocks and boulders in protoplanetary discs.

# Chapter 2

# SMA observations of young discs: separating envelope, disc, and stellar masses in class I YSOs


## Abstract

Young stars are born with envelopes, which in the early stages obscure the central (proto)star and circumstellar disc. In the class I stage, the discs are still young, but the envelopes are largely dispersed. This makes the class I sources ideal targets for studies of the early stages of discs. We aim to determine the masses of the envelopes, discs, and central stars of young stellar objects (YSOs) in the class I stage. We observed the embedded class I objects IRS 63 and Elias 29 in the $\rho$ Ophiuchi star-forming region with the Submillimeter Array (SMA) at 1.1 mm. IRS 63 and Elias 29 are both clearly detected in the continuum, with peak fluxes of 459 and 47 mJy/beam, respectively. The continuum emission toward Elias 29 is clearly resolved, whereas IRS 63 is consistent with a point source down to a scale of 3″ (400 AU). The SMA data are combined with single-dish data, and disc masses of 0.055 and $\leq$ 0.007 $M_\odot$ and envelope masses of 0.058 and $\leq$ 0.058 $M_\odot$ are empirically determined for IRS 63 and Elias 29, respectively. The disc+envelope systems are modelled with the axisymmetric radiative-transfer code RADMC, yielding disc and envelope masses that differ from the empirical results by factors of a few. $HCO^+$ $J$ = 3–2 is detected toward both sources, HCN $J$ = 3–2 is not. The $HCO^+$ position-velocity diagrams are indicative of Keplerian rotation and allow an estimate of the mass of the central stars. For a fiducial inclination of 30°, we find stellar masses of 0.37 ± 0.13 and 2.5 ± 0.6 $M_\odot$ for IRS 63 and Elias 29, respectively. The sensitivity and spatial resolution of the SMA at 1.1 mm allow a good separation of the discs around class I YSOs from their circumstellar envelopes and environments and the spectral resolution makes it possible to resolve their dynamical structure and estimate the masses of the central stars. The ratios of the envelope and disc masses $M_{\rm env}/M_{\rm disc}$ are found to be 0.2 and 6 for IRS 63 and Elias 29, respectively. This is lower than the values for class 0 sources, which have $M_{\rm env}/M_{\rm disc} \geq 10$, suggesting that this ratio is a tracer of the evolutionary stage of a YSO.



Dave Lommen, Jes Jørgensen, Ewine van Dishoeck, and Antonio Crapsi
Astronomy & Astrophysics 2008, 481, 141

## 2.1 Introduction

Low- and intermediate-mass stars are formed from the graviational collapse of molecular cloud cores. In the earliest stages, the newly-formed protostar remains embedded in the remnants of this core, a cold envelope of dust and gas, which is gradually accreted by the young star (e.g., Shu 1977). Due to the angular momentum initially present in the core, most of the envelope material does not fall directly onto the central protostar but is piled-up in a circumstellar disc (e.g., Terebey et al. 1984). Understanding this interplay between star, disc, and envelope is crucial in order to be able to relate the initial conditions of star formation such as the mass of the protostellar core to the end-product – namely the properties of the young star, and the mass and thus potential of the disc for forming planets. Some of the key questions include: Where does most of the mass reside at a given time? Will all the mass that is seen in prestellar cores or in the envelopes around deeply embedded sources end up in the star, or will a large fraction be dispersed from the system? How do the masses of the circumstellar envelope, the disc, and that of the central star evolve over time, and how long does it take for the circumstellar matter to be accreted onto the star?

Young stellar objects (YSOs) are usually classified according to their slopes in the infrared (IR) wavelength regime. Originally, the LW classification (Lada & Wilking 1984; Lada 1987) ran from the embedded class I, via the optically visible class II or classical T-Tauri stars, to the class III spectral energy distributions of post-T Tauri stars. Later, the class 0 stage was added to this classification (see, e.g., André et al. 1993), where the class 0 sources are distinguished from the class I sources through their high relative luminosity at submillimetre (submm) wavelengths. This classification roughly reflects the evolutionary stage of the YSOs under consideration. The most deeply embedded class 0 sources are thought to evolve through the class I stage while dissipating their circumstellar envelopes. Eventually they become optically visible as pre-main-sequence T-Tauri stars with circumstellar discs.

The class 0 and class II YSOs have been studied quite extensively with high-resolution (sub)millimetre interferometers (e.g., Jørgensen et al. 2007; Andrews & Williams 2007, and references therein). Studies of deeply embedded class 0 YSOs have shown that circumstellar discs are formed early (Harvey et al. 2003; Jørgensen et al. 2004), but in these systems, it is difficult to separate the emission of the disc from that of the envelope. The class I sources, in which a large part of the original circumstellar envelopes has been dissipated, are ideal to study young discs in YSOs. Interferometric studies of class I objects have so far been largely limited to studies at around 3 mm (e.g., Ohashi et al. 1997; Hogerheijde et al.

1997, 1998; Looney et al. 2000). The Submillimeter Array (SMA) allows observations around 1 mm, where the thermal dust continuum emission is an order of magnitude stronger than at 3 mm. Also at these shorter wavelengths it is possible to detect the higher rotational transitions of the molecules that trace the dense gas in the discs and inner envelopes of the young systems, rather than lower-density extended envelope emission.

We here present SMA observations of two class I objects that appear to be in an evolutionary stage where the kinematics of the circumstellar material are no longer dominated by infall. IRS 63 (WLY 2-63, GWAYL 4) and Elias 29 (Elia 2-29, WLY 1-7) are located in the $\rho$ Ophiuchi cloud, taken to be at a distance D = 125 ± 25 pc (de Geus et al. 1989). Spitzer photometry from the "Cores to Disks" Legacy program (Evans et al. 2003) was used to determine the source's infrared colours and their bolometric luminosities and temperatures. IRS 63 and Elias 29 have similar bolometric temperatures, $T_{\rm bol}$ = 351 K and 391 K, respectively, which places them in the LW class I regime. The bolometric luminosities were calculated to be $L_{\rm bol}$ = 0.79 $L_\odot$ for IRS 63 and 13.6 $L_\odot$ for Elias 29. According to their infrared slopes of $\alpha_{2-24\mu m}$ = 0.15 and 0.42, IRS 63 is the slightly more evolved, falling into the "flat-spectrum" class that separates the class I from the class II sources (Greene et al. 1994). The values for $\alpha_{\rm IR}$ quoted here are from un-dereddened observations. Correction for the extinction toward the $\rho$ Ophiuchi star-forming region (e.g., Flaherty et al. 2007) would result in lower values for $\alpha_{\rm IR}$; in other words, the sources may be slightly more evolved than the raw values of $\alpha_{\rm IR}$ suggest. In terms of environment, the two sources are quite each other's opposites. The SCUBA 850 $\mu$m map (Johnstone et al. 2004) from the COMPLETE survey (Ridge et al. 2006) shows that IRS 63 is an isolated compact source. Elias 29, on the other hand, is located in a dense ridge of molecular material, which contains several more YSOs. It is likely that these YSOs were formed from condensations in this molecular ridge.

We present the masses of all main components of class I YSOs, i.e., the central star, the disc, and the envelope, for the first time. IRS 63 and Elias 29 are the first two sources in a larger survey of class I objects studied with the SMA at 1.1 mm. These observations complement the survey of class 0 sources in the PROSAC programme (Jørgensen et al. 2007) and will allow us to trace the similarities and differences of these evolving protostars. The results of the complete campaign will be presented in a future paper. In §2.2, the observations are presented, and the results and implications are discussed in §§2.3 and 2.4. We summarise the main conclusions in §2.5.

## 2.2 Observations

IRS 63 and Elias 29 were observed with the SMA[1] (Ho et al. 2004) on 15 and 17 May 2006, respectively. Weather conditions were good on 15 May, with zenith optical depths at 225 GHz $\tau_{225}$ = 0.04–0.06 (as measured by a tipping radiometer operated by the Caltech Submillimeter Observatory). Conditions were slightly worse on 17 May, with $\tau_{225}$ starting at 0.16, falling to 0.1 during the first half of the night. Physical baselines ranged from 11.6 to 62.0 metres, and the resulting projected baselines ranged from 5.9 to 63.8 k$\lambda$, yielding a resolution of about $4.0 \times 2.3''$ (natural weighting). The correlator was configured to observe the lines of $HCO^+$ $J$ = 3–2 and HCN $J$ = 3–2 together with the continuum emission at 268 and 278 GHz. The line data were taken with 512 channels of 0.2 MHz width each, resulting in a velocity resolution of 0.23 km s$^{-1}$.

Calibration was done using the MIR package (Qi 2005), and imaging was done using the MIRIAD package (Sault et al. 1995). The quasars QSO B1622-297 and QSO B1514-241 served as gain calibrators, and the absolute fluxes were calibrated on Uranus. The absolute flux calibration is estimated to have an uncertainty of ∼20 %. The passbands were calibrated on Callisto and the quasar QSO B1253-055 (3C 279).

## 2.3 Results

The basic results of the observations are shown in Fig. 2.1 and summarised in Table 2.1.

### 2.3.1 Continuum data

Both sources are clearly detected in the continuum at 1.1 mm. Point-source and Gaussian fits were done in the $(u, v)$ plane to determine the peak and integrated fluxes, respectively. A continuum peak flux of 459 mJy bm$^{-1}$ and an integrated flux of 474 mJy were found for IRS 63, at a position which agrees with the 2MASS $K_S$-band position within $0\farcs1$. IRS 63 was also observed with the SMA by Andrews & Williams (2007) at higher resolution at 1.3 mm. Their interferometer flux for IRS 63, to which they refer as L1709 B[2], is consistent with the value here

[1]The Submillimeter Array is a joint project between the Smithsonian Astrophysical Observatory and the Academia Sinica Institute of Astronomy and Astrophysics and is funded by the Smithsonian Institution and the Academia Sinica.

[2]IRS 63 and L1709 B are often referred to as the same source (e.g., André & Montmerle 1994). However, L1709 B would appear to lie about 4 arcmin north of IRS 63 (e.g., Benson & Myers

and a mm slope $\alpha_{\rm mm} = 2.0 \pm 1.0$. The data of Elias 29 are best fitted by two sources. The brightest of the two agrees with the 2MASS $K_S$-band position of Elias 29 within $0\farcs2$, whereas the other source is offset by $3''$. The second peak is attributed to an enhancement in the ridge, from which Elias 29 likely formed, and is designated by "Ridge" in Table 2.1. Elias 29 and the ridge component yield continuum peak fluxes of 47 and 31 mJy bm$^{-1}$, and integrated fluxes of 72 and 28 mJy, respectively.

Plots of the visibility amplitudes as functions of projected baseline for IRS 63 and Elias 29 are shown in Fig. 2.2. Elias 29 shows a steeply rising flux toward the shortest baselines, indicating that an envelope is present around this source. The emission toward IRS 63 does not change appreciably with baseline length, indicating that this source is unresolved up to baselines of 60 k$\lambda$, or down to physical scales of about 400 AU.

Fig. 2.2 also shows the estimated single-dish flux at 1.1 mm. For this, the "mapped" fluxes from André & Montmerle (1994) at 1.25 mm were combined with newly determined 850 $\mu$m fluxes (SCUBA maps from the COMPLETE survey, Johnstone et al. 2004; Ridge et al. 2006). The SEDs are assumed to have a $F_\nu \propto \nu^\alpha$ dependence in this wavelength range, and are interpolated to the 1.1 mm wavelength at which the SMA observations were conducted. Fluxes of 355 and 780 mJy are found for Elias 29 and IRS 63, respectively, with an estimated uncertainty of 25%. These fluxes are significantly larger than the interferometer fluxes and indicate that extended emission is present around the compact components picked up with the SMA. This extended emission may be due to a circumstellar envelope, or to surrounding or intervening interstellar clouds, since the "mapped" regions of André & Montmerle (1994) are rather large, $40''$ and $60''$ for Elias 29 and IRS 63, respectively.

### 2.3.2 Line data

$HCO^+$ $J = 3$–2 is detected toward both sources, whereas HCN $J = 3$–2 is not. Elias 29 appears to be about ten times as strong in $HCO^+$ $J = 3$–2 integrated emission as IRS 63 (see Table 2.1). The emission toward IRS 63 is compact, coincident with the continuum peak, and shows a velocity gradient in the North-South direction, see Fig. 2.3. The integrated emission in the direction of Elias 29 is more extended and can be fitted with two elliptical Gaussians, as is shown in the left panel of Fig. 2.4. The centre position of the smaller Gaussian coincides with the continuum peak, as well as with the infrared position, and is attributed

1989). The source that Andrews & Williams (2007) refer to as L1709 B, is in fact IRS 63.

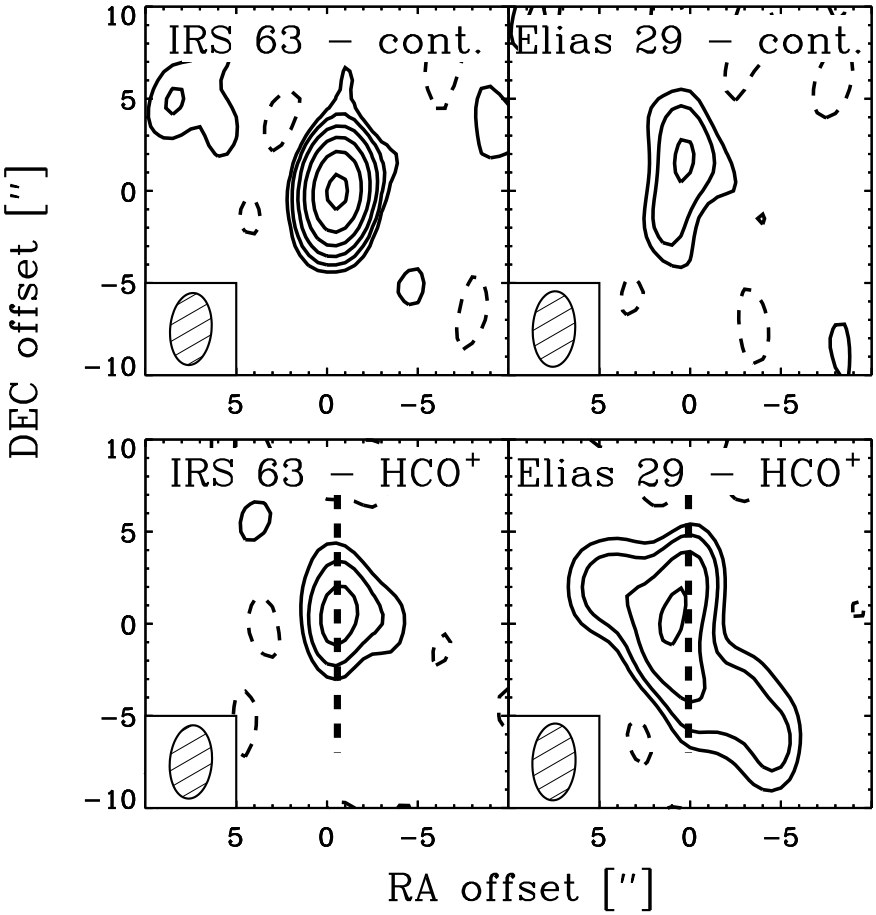


Figure 2.1: SMA images of the 1.1 mm continuum (*top panels*) and integrated $HCO^+$ 3–2 (*bottom panels*) emission. Contours are drawn at 2, 4, 8, 16, 32, and 64 times the respective RMS noise levels, with the RMS being about 6 mJy $bm^{-1}$ for the continuum and about 65 mJy $bm^{-1}$ for the line data. Negative contours are dashed. The positional offsets are with respect to the coordinates of the observational phase centre. The dashed lines indicate how the position velocity diagrams (Fig. 2.7) are directed.

to Elias 29 itself. The second Gaussian has a very elongated shape, offset from the infrared source, and is attributed to a density enhancement in the nearby ridge. The right panel of Fig. 2.4 shows the $HCO^+$ $J$ = 3–2 spectra toward the continuum

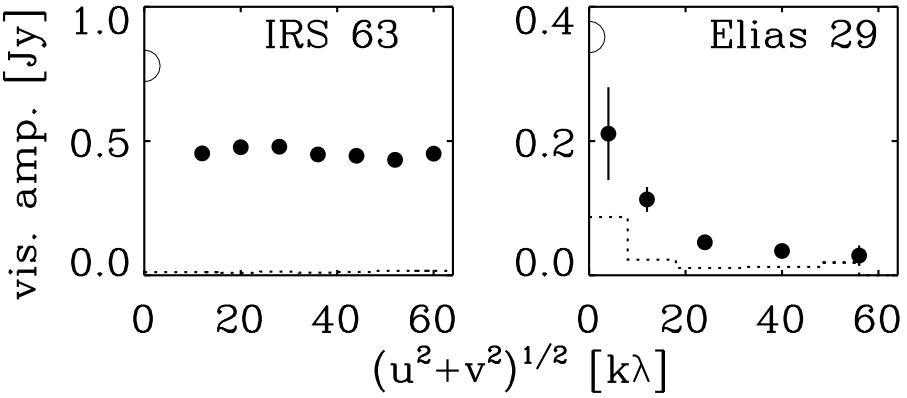


Figure 2.2: Continuum amplitude as a function of projected baseline for IRS 63 (*left panel*) and Elias 29 (*right panel*). The data points give the amplitude per bin, where the data are binned in annuli according to $(u, v)$ distance. The error bars show the statistical $1\sigma$ errors, most often smaller than the data points, and the dotted lines give the expected amplitude for zero signal, i.e., the anticipated amplitude in the absence of source emission. The half-open circles at zero $(u, v)$ distance give the zero-spacing 1.1 mm flux, interpolated between 850 $\mu$m and 1.25 mm single-dish fluxes (André & Montmerle 1994; Johnstone et al. 2004; Ridge et al. 2006, see text).

positions of Elias 29 and IRS 63, binned to 0.9 km s$^{-1}$. The $HCO^+$ $J$ = 3–2 emission toward IRS 63 appears to be centred at $V_{LSR}$ = 3.3 km s$^{-1}$.

## 2.4 Discussion and interpretations

### 2.4.1 Envelope and disc masses

#### Empirical results

A first-order estimate of the disc and envelope masses can be obtained by assuming that the continuum flux of the envelope is resolved out by the interferometer on the longest baselines (Fig. 2.2). Hence, the emission on the longest baselines is solely due to the disc, whereas the single-dish flux comes from the disc and envelope combined. Assuming that the disc and the envelope are isothermal and

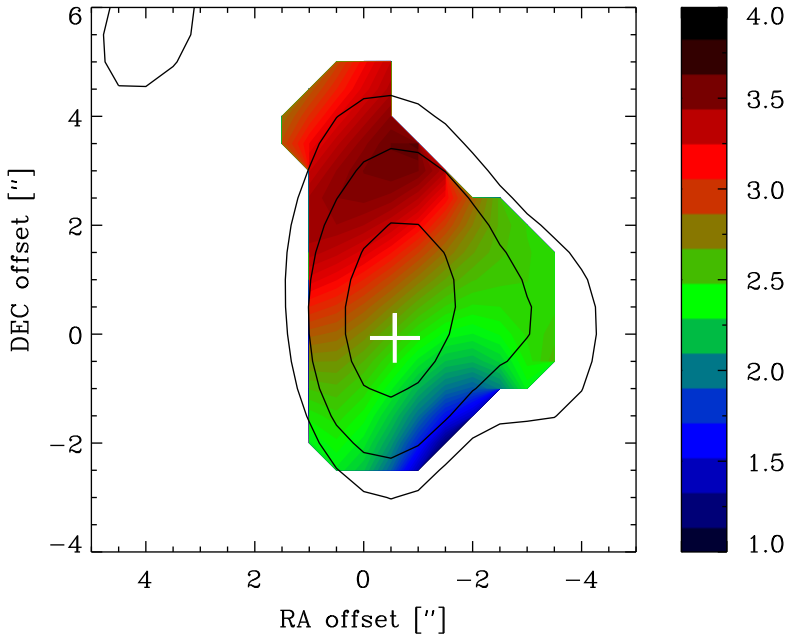


Figure 2.3: First-moment map of IRS 63. Contours are drawn at 2, 4, and 8 times the RMS of 67 mJy bm$^{-1}$. The positional offsets are with respect to the coordinates of the observational phase centre, and the cross indicates the continuum position of IRS 63 from a point-source fit in the $(u, v)$ plane, see Table 2.1. *A colour version of this figure can be obtained from the electronic version of the paper.*

the dust emission is optically thin, the disc mass is given by

$$M_{\rm disc} = \frac{F_\nu \Psi D^2}{\kappa_\nu B_\nu(T_{\rm dust})}, \tag{2.1}$$

where $F_\nu$ is the flux at frequency $\nu$ on the longest baselines, $\Psi$ is the gas-to-dust ratio, $\kappa_\nu$ is the dust opacity at $\nu$, and $B_\nu(T_{\rm dust})$ is the emission from a black body at $T_{\rm dust}$. Using fiducial values for all these parameters – $\Psi = 100$, $T_{\rm dust} = 30$ K, and $\kappa_\nu = 1.18$ cm$^2$ g$^{-1}$ ("OH5" coagulated dust with icy mantles, found in the fifth column of Table 1 of Ossenkopf & Henning 1994, interpolated to the observed frequency $\nu = 273$ GHz) – disc masses of 0.055 $M_\odot$ and 0.007 $M_\odot$ are found for

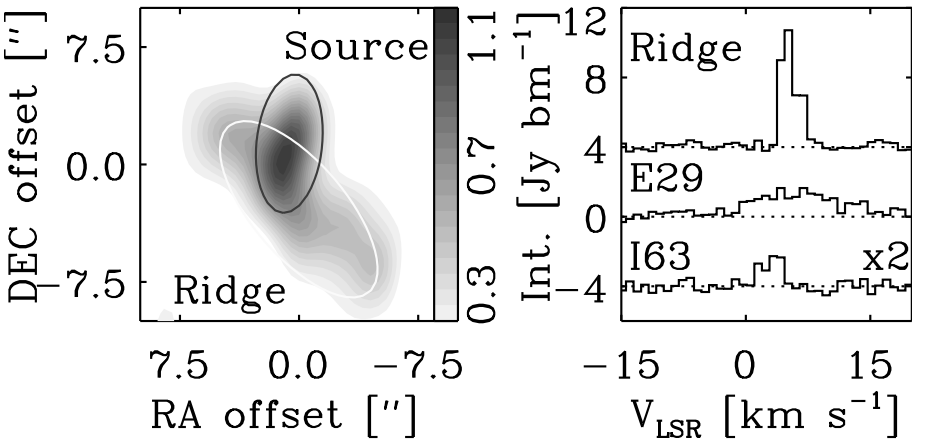


Figure 2.4: *Left panel*: $HCO^+$ $J$ = 3–2 integrated emission toward Elias 29. The grayscale is linear from 0.2 to 1.2 Jy bm$^{-1}$. The emission is fitted with two Gaussians, the one in the North-South direction tracing the emission due to Elias 29, and the other, larger one tracing emission from a density enhancement in the ridge. *Right panel*: spectral lines, integrated over $2 \times 2''$ regions, centred on the continuum positions of Elias 29, of the ridge (shifted by +4 Jy bm$^{-1}$), and of IRS 63 (shifted by -4 Jy bm$^{-1}$), and binned to 0.9 km s$^{-1}$. The $HCO^+$ $J$ = 3–2 emission toward IRS 63 appears to be centred at $V_{LSR}$ = 3.3 km s$^{-1}$.

IRS 63 and Elias 29, respectively. Using the opacity law as quoted by Beckwith et al. (1990), $\kappa_\nu = 10\left(\nu/10^{12}\mathrm{Hz}\right)^\beta$, and taking $\beta = 1$, a dust opacity at 273 GHz of $\kappa_\nu = 2.73$ cm$^2$ g$^{-1}$ is found, and the disc masses decrease to 0.024 $M_\odot$ and 0.003 $M_\odot$ for IRS 63 and Elias 29, respectively.[3] Note that this method to estimate the disc mass is only valid when the disc is unresolved by the observations. If the disc were clearly resolved, the flux on the longest baselines would not include the emission from the outer disc, but only that from smaller radii, unresolved by those baselines. Due to its closeness, the enhancement in the ridge near Elias 29 may contribute to its flux, even on the longest baselines of $\geq$ 50 k$\lambda$ or scales $< 4''$. However, in the estimate of the flux on the longest baselines (Table 2.1), the ridge component was fitted simultaneously with Elias 29, and hence its contribution to the derived disc mass is expected to be minimal.

[3]The opacity law quoted by Beckwith et al. (1990) is $\kappa_\nu = 0.1\left(\nu/10^{12}\mathrm{Hz}\right)^\beta$ for the gas and dust combined, implicitly assuming a gas-to-dust ratio $\Psi = 100$, consistent with our work.

Table 2.1: Results of SMA observations at 1.1 mm.

| | IRS 63 | Elias 29 | Ridge |
|---|---|---|---|
| $F_\nu$ (P)[a] [mJy bm$^{-1}$] | 459 | 47 | 31 |
| RA[a] [J2000] | 16:31:35.65 | 16:27:09.42 | 16:27:09.48 |
| Dec[a] [J2000] | -24:01:29.56 | -24:37:18.91 | -24:37:22.48 |
| RMS[b] [mJy bm$^{-1}$] | 6 | 5 | 5 |
| Circular Gaussian fits to all data | | | |
| $F_\nu$ (G)[c] [mJy] | 474 | 72 | 28 |
| FWHM[c] [arcsec] | 0.55 ± 0.08 | 2.2 ± 0.5 | – |
| Circular Gaussian fits to data ≥16 k$\lambda$ (scales < 13 arcsec) | | | |
| $F_\nu$ (G)[c] [mJy] | 480 | 57 | 27 |
| FWHM[c] [arcsec] | 0.62 ± 0.08 | 1.7 ± 0.7 | – |
| Line data | | | |
| HCO$^+$[d] [K km s$^{-1}$] | 3.1 ± 0.3 | 23.7 ± 2.5 | 23.5 ± 2.5 |
| HCN[d] [K km s$^{-1}$] | < 1.8 | < 3.8 | < 3.8 |

[a] Point source fit in the $(u, v)$ plane.

[b] Calculated from the cleaned image.

[c] Circular Gaussian fit in the $(u, v)$ plane.

[d] Integrated intensities are from a $4 \times 4''$ square around the continuum emission. The synthesised beam is $\sim 4 \times 2.5''$. HCN was not detected; quoted values are $3\sigma$ upper limits.

In a similar fashion the envelope masses in the systems can be found. First, the contributions from the envelopes to the 1.1 mm single-dish fluxes are determined by subtracting the fluxes at baselines $\geq$ 16 k$\lambda$ (see Table 2.1) from the single-dish fluxes as found in Sect. 2.3. The envelope masses are then found by using Eq. (2.1), with the temperatures of the envelopes taken to be 20 K. For an optically thin envelope around stars with luminosities of 0.79 and 13.6 $L_\odot$ applicable to IRS 63 and Elias 29, a temperature of 17–29 K is expected at a radius of 940 AU corresponding to the size of the JCMT single-dish beam (from, e.g., Eq. (2) of Chandler & Richer 2000, taking the opacity index $\beta = 1$). This yields an envelope mass $M_{\rm env} = 0.058$ $M_\odot$ for IRS 63 within a $30''$ radius, where the contribution from the envelope to the total 1.1 mm flux is 38%. Coincidentally, also for Elias 29 an envelope mass $M_{\rm env} = 0.058$ $M_\odot$, within a $20''$ radius, is found. However, in this system the contribution from the envelope to the total 1.1 mm flux is 84%. As for the disc mass, also the envelope mass found for Elias 29 should be

taken as an upper limit because of the closeness of the ridge enhancement. Note, however, that it is unlikely that the bulk of the continuum emission is due to this enhancement, because of the coincidence of the continuum peak with the infrared source and also with the single-dish submillimetre positions. Using the opacities of Beckwith et al. (1990) will lower all masses by a factor of about 2.

### Modelling

To provide more physical grounding to the values for $M_{\rm disc}$ and $M_{\rm env}$ estimated in the previous section, a radiative transfer code was used to fit simultaneously the millimetre interferometry and the spectral energy distributions. IRS 63 and Elias 29 were modelled with a new version of the programme RADMC (e.g., Dullemond & Dominik 2004a). RADMC is an axisymmetric Monte-Carlo code for dust continuum radiative transfer in circumstellar discs and envelopes in which the stellar photons are traced in three dimensions. The code is based on the method of Bjorkman & Wood (2001).

The density structure of the disc is given by (see Crapsi et al. 2007)

$$\rho_{\rm disc}(r,\theta) = \frac{\Sigma_0 (r/R_0)^{-1}}{\sqrt{(2\pi)} H(r)} \exp\left(-\frac{1}{2}\left[\frac{r\cos(\theta)}{H(r)}\right]^2\right), \tag{2.2}$$

where $r$ is the radial distance from the central star and $\theta$ is the angle from the axis of symmetry. The inner radius was fixed to 0.1 AU for IRS 63, and to 0.25 AU for Elias 29, to account for the higher luminosity of the star. At these radii, the temperature is of the order of the dust sublimation temperature. Note that the exact sublimation temperature, and hence the disc inner radius, depends on the exact dust species and local density. The vertical scale height of the disc is given by $H(r) = r \cdot H_0/R_0 \cdot (r/R_0)^{0.17}$, where $R_0$ was left free to vary, and $H_0/R_0$ was arbitrarily fixed to 0.17. Chiang & Goldreich (1997) find $H(r)/r \propto r^{2/7}$. However, that estimate is based on grey opacities and constant surface density, and somewhat smaller flaring is usually more realistic. Hence, we chose $H(r) \propto r \cdot r^{0.17}$. $\Sigma_0$ was scaled to the disc mass, which was also left as a free parameter. The envelope density follows the equation for a rotating, infalling model (Ulrich 1976; Crapsi et al. 2007)

$$\rho_{\rm envelope}(r,\theta) = \rho_0 \left(\frac{r}{R_{\rm rot}}\right)^{-1.5} \left(1 + \frac{\cos\theta}{\cos\theta_0}\right)^{0.5} \times \\ \times \left(\frac{\cos\theta}{2\cos\theta_0} + \frac{R_{\rm rot}}{r}\cos^2\theta_0\right)^{-1}, \tag{2.3}$$

Table 2.2: Model parameters for IRS 63 and Elias 29.

| | IRS 63 | Elias 29 |
|---|---|---|
| Modelling parameters and results | | |
| Stellar luminosity (*fixed*) | 0.79 $L_\odot$ | 13.6 $L_\odot$ |
| Disc inner radius (*fixed*) | 0.1 AU | 0.25 AU |
| Disc outer radius, $R_0$ | 100 AU | 200 AU |
| Disc height at outer radius, $H_0/R_0$ (*fixed*) | 0.17 | 0.17 |
| Envelope outer radius (*fixed*) | 10,000 AU | 10,000 AU |
| Centrifugal radius, $R_{\rm rot}$ | 100 AU | 300 AU |
| Inclination | 30° | 30° |
| Disc mass, $M_{\rm disc}$ | 0.13 $M_\odot$ | 0.004 $M_\odot$ |
| Envelope mass, $M^{\rm a}_{\rm env}$ | 0.022 $M_\odot$ | 0.025 $M_\odot$ |
| Empirical results | | |
| $M^{\rm a}_{\rm env}$ [$M_\odot$] | 0.058 | $\leq 0.058$ |
| $M_{\rm disc}$ [$M_\odot$] | 0.055 | $\leq 0.007$ |
| $M^{\rm b}_{\rm star}$ [$M_\odot$] | $0.37 \pm 0.13$ | $2.5 \pm 0.6$ |

[a] The envelope mass is defined as the mass, not contained in the disc, within a single-dish radius, i.e., 30″/3750 AU for IRS 63, and 20″/2500 AU for Elias 29.

[b] Assuming an inclination $i = 30°$ (see Sect. 2.4.2 for discussion).

where $\theta_0$ is the solution of the parabolic motion of an infalling particle, $R_{\rm rot}$ is the centrifugal radius of the envelope, and $\rho_0$ is the density in the equatorial plane at $R_{\rm rot}$. $\rho_0$ was scaled to accomodate the total envelope mass, and $R_{\rm rot}$, which can have a significant influence on the amplitude as a function of baseline length, was left free to vary. The outer radius of the envelope was fixed to 10,000 AU, where the temperature is similar to that of the ambient interstellar cloud. The parameters, as summarised in Table 2.2, give the best-fit models by eye; a full $\chi^2$ minimization is not warranted by the relatively low resolution and S/N of the data. Our models do not have outflow cavities in the envelopes. Note that the actual physical structure of the envelope (centrifugal radius, outflow cavities, etc.) may considerably affect the mid-IR SED and thus the derived inclination from the models (e.g., Whitney et al. 2003; Jørgensen et al. 2005).

Two different dust species are used in these models, "hot" dust where the temperature is higher than 90 K, and "cold" dust where the temperature is below 90 K. The opacities used are "OH2" (coagulated dust without ice mantles, Ossenkopf &

Henning 1994) for the hot dust, and "OH5" (coagulated dust with thin ice mantles) for the cold dust. The central stars were represented by sources with luminosities of 0.79 and 13.6 $L_\odot$ (IRS 63 and Elias 29, respectively), which were taken to be equal to the bolometric luminosities of the sources, and the temperature structures in the discs and envelopes were then calculated by propagating the stellar photons through the systems.

The results of the modelling are shown in Fig. 2.5. A model with only a 0.055 $M_\odot$ disc reproduces the amplitude as a function of baseline quite well for IRS 63, but fails to produce enough single-dish flux. A 0.35 $M_\odot$ envelope-only model, on the other hand, produces enough single-dish flux in the (sub)mm regime, but falls off too quickly toward longer baselines. To allow for a comparison with the empirical model (Sect. 2.4.1) the envelope mass was defined as the mass, present within the single-dish aperture (i.e., a 30″ radius for IRS 63 and a 20″ radius for Elias 29), and not contained in the disc. A model with both a disc and an envelope is necessary to explain the observations of IRS 63, and the best model consists of a disc of 0.13 $M_\odot$ and an envelope of 0.022 $M_\odot$. This model also fits the observed IRS 63 SED well, if a foreground extinction of $A_V$ = 7 mag is assumed, see Fig. 2.6. The region in which IRS 63 is located has a very high $A_V$ of about 24 mag as found in extinction maps produced by the Spitzer "Cores to Disks" Legacy program (Evans et al. 2003, 2007). These maps measure the large scale ($\sim$ 5′) cloud extinction on the basis of background stars, and therefore includes an extra contribution besides envelope extinction.

The amplitude as a function of baseline for Elias 29 is best explained by a 0.004 $M_\odot$ disc and a 0.025 $M_\odot$ envelope. For this source, no further attempt to model the SED was made, because the close presence of the ridge enhancement makes a model that is axisymmetric on scales larger than several 100 AU unapplicable.

**Discussion**

Even though the disc and envelope masses derived from the empirical and detailed model results differ by up to a factor of a few, we are confident that they are accurate within this range. For example, a significantly larger disc in the IRS 63 model would show a very steep fall-off in the amplitude as a function of baseline length, which is not observed (Fig. 2.5). Likewise, an envelope significantly more massive than 0.022 $M_\odot$ found for IRS 63 would obscure the central star so much that the near- and mid-IR flux would be severly underestimated (Fig. 2.6). In the further discussion, we will use the disc and envelope masses as found by the detailed modelling, but note that the overall conclusions do not change if the

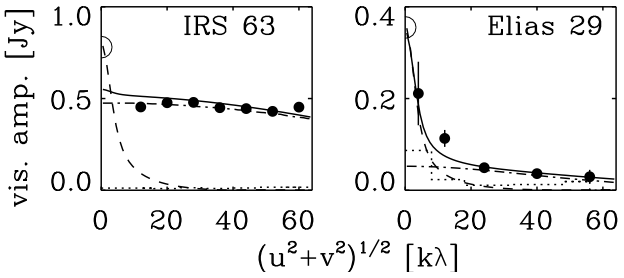


Figure 2.5: Continuum amplitude as a function of projected baseline for IRS 63 (*left panel*) and Elias 29 (*right panel*), with models overplotted. The dashed lines show models, consisting of an envelope only. They fit the single-dish (sub)mm data well, but fall off too fast to longer projected baselines. The dash-dotted lines are from disc-only models. They fit the interferometric data well, but do not have enough flux on the shortest baselines. The solid lines are for the models that provide a good fit to the SED and to the spatial information provided by the interferometric observations. The dotted lines indicate the expected amplitude for zero signal.

empirical results are used.

The envelope masses of IRS 63 and Elias 29 are in the same range as those presented by, e.g., Hogerheijde et al. (1997) for a sample of embedded class I sources in the Taurus-Auriga star-forming region. However, the envelope masses of the deeply embedded class 0 objects are found to be considerably higher, $\gtrsim$ 1 $M_\odot$ (Jørgensen et al. 2002; Shirley et al. 2002; Hatchell et al. 2007). While some fraction of sources may simply originate from lower mass cores, it is clear that all class 0 objects must pass through a stage with $M_{\rm env} \approx 0.1$ $M_\odot$ on their way to the pre-main-sequence stage. A larger sample is needed to address the question whether the mass that was initially present in the envelope will first accumulate in the disc, or whether it will pass through the disc and onto the star directly, leaving the disc in a steady state through the entire class I stage.

An interesting quantity for these YSOs is the ratio $M_{\rm env}/M_{\rm disc}$, as this may be a direct measure for their evolutionary stage. The values for the two objects under consideration here – 0.2 for IRS 63 and 6 for Elias 29 – are quite different, although the value for Elias 29 is rather uncertain due to the contribution of the ridge enhancement to the continuum emission. From these simple arguments, Elias 29 is the less evolved, rather like the deeply embedded class 0 sources in the PROSAC sample (Jørgensen et al. 2007), which show $M_{\rm env}/M_{\rm disc} \gtrsim 10$. IRS 63,

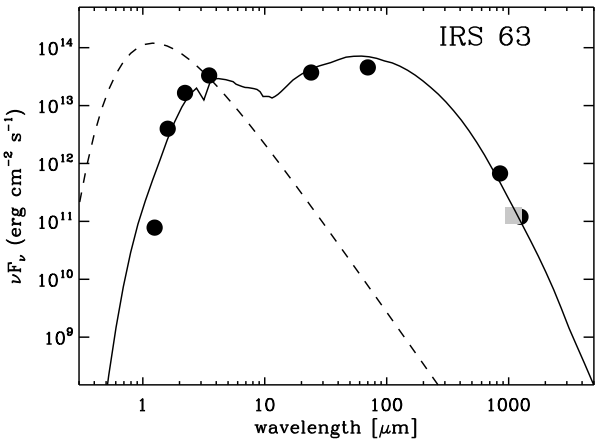


Figure 2.6: Spectral energy distribution of IRS 63 using the model parameters of Table 2 extincted by $A_V$=7 mag (solid line). The dashed line shows the model star, which has a luminosity of 0.79 $L_\odot$, and is represented by a black-body with a temperature of 3 000 K. Overplotted are *JHKL* photometry (Haisch et al. 2002), MIPS 24 and 70 $\mu$m fluxes (c2d[3]), JCMT 850 $\mu$m 60″ integrated flux (COMPLETE), SMA 1.10 mm peak flux (this work; square), and IRAM 1.25 mm 60″ integrated flux (André & Montmerle 1994).

on the other hand, is well on its way toward the optically visible class II or T-Tauri stage, which have $M_{\rm env} \approx 0$. This confirms the notion that the Lada classification is primarily a phenomenological one, not necessarily representing the actual physical stage the YSO is in (see, e.g., Crapsi et al. 2007).

### 2.4.2 Keplerian rotation and stellar masses

Both IRS 63 and Elias 29 show a velocity gradient in the $HCO^+$ emission, which is interpreted as the rotation of a circumstellar disc. The mass of the central object can be estimated from position-velocity diagrams along the major axis of the disc, as indicated in Fig. 2.1. An elliptical Gaussian was fitted to each channel in the $HCO^+$ data in the $(u, v)$ plane, using the MIRIAD task *uvfit*. This yielded a best-fit position per channel with corresponding uncertainties in right ascension and declination, and consequently a declination offset from the phase centre in the

[3]Delivery of data from the c2d Legacy Project: IRAC and MIPS (Pasadena, SSC, Evans et al. 2007).

physical plane. Note that the fitting was carried out in the $(u, v)$ plane, so as not to be hindered by artefacts that may arise in the deconvolution process. Position-velocity diagrams were created by plotting the declination offset as a function of velocity channel, where only coordinates with an uncertainty in the declination of less than $0\farcs5$ were taken into account. Subsequently, the signatures of Keplerian rotation around a point source were fitted to the position-velocity diagrams (Fig. 2.7). In the fitting process, the values for $M_{\rm star}$ (the mass of the central object), the central velocity of the system with respect to the local rest frame, and the declination offset from the source to the phase centre were varied, and a global minimum $\chi^2$ was determined.

Assuming a Keplerian disc seen edge-on ($i = 90°$), a central mass of $M_{\rm star} = 0.09 \pm 0.03$ M$_\odot$ is found for IRS 63. The exact inclination of IRS 63 is hard to determine due to the high extinction in the region. However, an inclination larger than $\sim 45°$ can be ruled out because of the source's brightness at 3–5 $\mu$m (Pontoppidan et al. 2003). Assuming an inclination of 30°, and taking into account the $\sin^2 i$ dependence, the mass of the central object increases to $M_{\rm star} = 0.37 \pm 0.13$ M$_\odot$. For Elias 29, the points attributed to the emission from the dense ridge (Fig. 2.7) were disregarded in the fitting procedure. A lower limit to the central mass of $M_{\rm star} = 0.62 \pm 0.14$ M$_\odot$ is found, under the assumption $i = 90°$. The flatness of the SED limits the inclination of this source to $< 60°$ (Boogert et al. 2002). A fully face-on orientation, on the other hand, is unlikely, given the presence of low surface brightness scattered K-band light (Zinnecker et al. 1988). An inclination $i = 30°$ yields a mass for the central source of $2.5 \pm 0.6$ M$_\odot$. With such a high mass, the central star is likely to emerge as a Herbig-Ae/Be star, once the surrounding envelope is dissipated.

It is interesting to compare the inferred masses to those inferred for optically visible pre-main-sequence stars. With a stellar mass of 0.37 M$_\odot$ and a stellar luminosity of 0.79 L$_\odot$, IRS 63 would be found to have an age of about $5 \times 10^5$ yr, when compared to evolutionary tracks of classical and weak-lined T-Tauri stars in the $\rho$ Ophiuchi cloud (Wilking et al. 2005; D'Antona & Mazzitelli 1997). A similar age would be found for Elias 29 (e.g., Palla & Stahler 1993).

## 2.5 Conclusions

We used the SMA to observe the class I YSOs Elias 29 and IRS 63 at 1.1 mm. The main results are as follows.

- Both sources are detected in the continuum and in the $HCO^+$ $J = 3$–2 line, but not in the HCN $J = 3$–2 line. The $HCO^+$ emission toward IRS 63 is

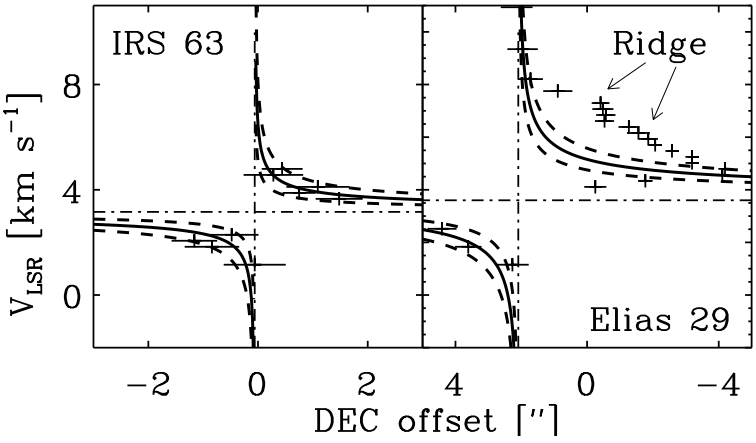


Figure 2.7: Velocity of the $HCO^+$ $J$ = 3–2 line as a function of the declination offset from the phase centre for IRS 63 (*left panel*) and Elias 29 (*right panel*). The solid lines show the results from $\chi^2$ fits to the data, yielding central masses of 0.37 $M_\odot$ (IRS 63) and 2.5 $M_\odot$ (Elias 29) for inclinations of 30°; the dashed lines show formal 99% confidence intervals. Points attributed to the emission from the dense ridge are indicated and are not included in the fit. The declination offsets are different for the two panels.

compact and associated with the YSO, whereas a significant part of the molecular emission in the direction of Elias 29 is due to an enhancement in the ridge from which Elias 29 formed.

- Assuming that the continuum emission toward the sources is optically thin, and that any circumstellar envelope is resolved out by the interferometer on the longest baselines, we find empirical disc masses of 0.055 and $\leq$ 0.007 $M_\odot$ for IRS 63 and Elias 29, respectively. By comparing our interferometer data with single-dish observations, envelope masses of 0.058 $M_\odot$ are derived for both sources, within 30″ radius for IRS 63 and 20″ radius for Elias 29, where the value for Elias 29 should be treated as an upper limit because of the presence of the ridge enhancement.

- Using a radiative-transfer code to create SEDs and amplitude vs $(u, v)$-distance plots for different combinations of disc and envelope masses, we find disc masses of 0.13 $M_\odot$ and 0.004 $M_\odot$ for IRS 63 and Elias 29, respectively, and envelope masses of 0.022 $M_\odot$ and 0.025 $M_\odot$.

- The modelling results yield rather different ratios of $M_{env}/M_{disc}$ for IRS 63 and Elias 29: 0.2 and 6, respectively, with uncertainties of a factor of a few. From this it is concluded that IRS 63 is well on its way to become an optically visible class II source, rather than an embedded class I source. Elias 29, on the other hand, is more like the deeply embedded class 0 sources.

- Velocity gradients in the $HCO^+$ $J = 3$–2 emission are interpreted as signs of Keplerian rotation, and indicate central masses of $2.5 \pm 0.6$ $M_\odot$ for Elias 29 and $0.37 \pm 0.13$ $M_\odot$ for IRS 63, for inclinations of 30°. These masses correspond to ages of a few $10^5$ yr.

With a larger set of sources treated in a similar manner as is presented for IRS 63 and Elias 29 here, it will be possible to constrain models for the evolution of the envelope, disc, and stellar masses through this important stage of YSOs.

## Acknowledgements

We would like to thank the anonymous referee for a very constructive report, which greatly improved the paper. Demerese Salter and Doug Johnstone are thanked for providing us with data from JCMT SCUBA observations. The discussions with the members of the Leiden "AstroChem" group were very useful. We are grateful to Kees Dullemond for providing us with the most recent version of the RADMC package. Partial support for this work was provided by a Netherlands Research School For Astronomy network 2 grant and by a Netherlands Organisation for Scientific Research Spinoza grant.

# Chapter 3

# Investigating grain growth in discs around southern T-Tauri stars at millimetre wavelengths


## Abstract

Low-mass stars form with discs in which the coagulation of grains may eventually lead to the formation of planets. It is not known when and where grain growth occurs, as models that explain the observations are often degenerate. A way to break this degeneracy is to resolve the sources under study. We here aim to find evidence for the existence of grains of millimetre sizes in discs around in T-Tauri stars, implying grain growth. The Australia Telescope Compact Array (ATCA) was used to observe 15 southern T-Tauri stars, five in the constellation Lupus and ten in Chamaeleon, at 3.3 millimetre. The five Lupus sources were also observed with the Submillimeter Array (SMA) at 1.4 millimetre. Our new data are complemented with data from the literature to determine the slopes of the spectral energy distributions in the millimetre regime. Ten sources were detected at better than $3\sigma$ with the ATCA, with $\sigma \approx 1$–2 mJy, and all sources that were observed with the SMA were detected at better than $15\sigma$, with $\sigma \approx 4$ mJy. Six of the sources in our sample are resolved to physical radii of $\sim$ 100 AU. Assuming that the emission from such large discs is predominantly optically thin, the millimetre slope can be related directly to the opacity index. For the other sources, the opacity indices are lower limits. Four out of six resolved sources have opacity indices $\lesssim 1$, indicating grain growth to millimetre sizes and larger. The masses of the discs range from $< 0.01$ to 0.08 $M_\odot$, which is comparable to the minimum mass solar nebula. A tentative correlation is found between the millimetre slope and the strength and shape of the 10-$\mu$m silicate feature, indicating that grain growth occurs on similar (short) timescales in both the inner and outer disc.



Dave Lommen, Chris Wright, Sarah Maddison, Jes Jørgensen,
Tyler Bourke, Ewine van Dishoeck, Annie Hughes, David Wilner,
Michael Burton, and Huib Jan van Langevelde
Astronomy & Astrophysics 2007, 462, 211

## 3.1 Introduction

Discs of dust and gas are observed around many young stars. According to the so-called core-accretion model (Safronov & Zvjagina 1969), planetary systems such as our own Solar System are formed in these circumstellar discs: the solid particles coagulate to form larger grains, which will grow to eventually form planets. The grains mainly consist of carbon and silicates. The silicate grains are readily observed through their 10- and 20-$\mu$m features. Both the change from amorphous to more crystalline grains, as well as the growth of grains from submicron sizes to sizes of several $\mu$m have been observed by the Infrared Space Observatory (ISO, Malfait et al. 1998; van Boekel et al. 2005), and more recently by the Spitzer Space Telescope (Kessler-Silacci et al. 2006). Although the qualitative picture of grain growth has become much clearer over the last few years, several quantitative details are still under discussion. Open questions include for example the timescale over which grain growth occurs and how this relates to the disc's physical structure (e.g., its temperature and density profile). See Dominik et al. (2006) for a recent discussion of both laboratory measurements and theoretical modelling of the aggregation of dust in protoplanetary discs.

A large sample of solar-mass T-Tauri stars have recently been observed with the InfraRed Spectrograph (IRS) on board the Spitzer Space Telescope, in the context of the "Cores to Disks" (c2d) legacy (Evans et al. 2003) and other programmes. Most of the sources in the c2d sample show 10- and 20-$\mu$m amorphous silicate features (Kessler-Silacci et al. 2006), confirming the results of earlier ISO and ground-based 10-$\mu$m observations (e.g., van Boekel et al. 2003; Przygodda et al. 2003), and extending the observed protoplanetary disc sample to lower mass objects. The data indicate a large variety of silicate profiles, ranging from strongly peaked silicate bands and steeply rising spectral energy distributions (SEDs) to "boxy" silicate profiles and flat SEDs. The boxy features with low feature-to-continuum ratios are interpreted as grain growth to micron size (Bouwman et al. 2001).

One possible explanation for the different spectra and SEDs is that grain growth and the shape of the disc are related. Dullemond & Dominik (2004a) identified a correspondence between the growth of grains in a circumstellar disc and the evolution of the disc from a "flaring" to a "self-shadowed" geometry. In their models, the larger, more massive dust grains settle to the midplane of the discs as the grains grow, and the initially flared discs evolve into flatter, self-shadowed discs. To what extent this process is related to the age of the young star is still under debate; there are indications that some young stellar objects evolve more quickly than others.

Numerical models show that the process of settling and coagulation is rapid, being well underway at distances of 1–30 AU from the central star in $\sim 10^4$ yrs (e.g., Nomura & Nakagawa 2006). Models predict that the slopes of the SEDs in the millimetre wavelength range will become shallower as the grains in the disc grow to millimetre (mm) and subsequently centimetre (cm) and larger sizes (Dullemond & Dominik 2004a; D'Alessio et al. 2006). It is therefore necessary to observe these sources at larger wavelengths than the infrared. Furthermore, millimetre observations probe the entire disc, including the cold midplane, whereas infrared observations can only probe the hot surface layer of the inner disc. However, a shallow millimetre slope in itself is not enough evidence for grain growth in the discs, since an excess flux at long wavelengths may also be caused by a very small, optically thick disc (see, e.g., Beckwith & Sargent 1991). To break this degeneracy it is necessary to resolve the discs to determine their actual sizes, since if the physical disc size is known, a reasonable estimate of the disc's opacity can be obtained. To resolve the discs around T-Tauri stars, interferometric observations are indispensable.

Considerable progress has been made in this field over the last several years. Wilner et al. (2000) resolved the inner disc of the classical T-Tauri star TW Hya in dust emission at 7 mm using the Very Large Array (VLA). Calvet et al. (2002) did extensive modelling of the SED of this source and showed that the dust grains in the disc must have grown to sizes of at least $\sim$ 1 cm. Wilner et al. (2003) used the Australia Telescope Compact Array (ATCA) to study TW Hya at 3.4 mm and found that a passive two-layer disc (Chiang & Goldreich 1999) provides a reasonable model to explain the observations. Ten T-Tauri stars in the Taurus-Auriga star-forming regions were resolved at 7 mm with the VLA by Rodmann et al. (2006); the majority of these show strong evidence for grain growth to at least millimetre-sized dust.

The more massive counterparts of the T-Tauri stars, the Herbig-Ae/Be stars, have been studied extensively. Meeus et al. (2001) classified 14 isolated Herbig-Ae/Be stars into two groups based on the shape of the SED. Discs with a flared outer part of the disc show a rising mid-infrared (20–100 $\mu$m) excess (*Group I* in the classification by Meeus et al. 2001), whereas self-shadowed discs have more modest mid-infrared excesses (*Group II*). Acke et al. (2004) compared the millimetre slopes for a sample of 26 Herbig-Ae/Be stars, based on single-dish data, and found that *Group II* sources have in general a shallower slope, consistent with grain growth to larger sizes than in the *Group I* sources, and observationally confirming the model predictions from Dullemond & Dominik (2004a). Natta et al. (2004) analysed interferometric observations of nine pre-main-sequence

stars, mostly Herbig-Ae stars, and find that the observations are well explained with dust size distributions containing boulders of up to metre sizes.

We have used the ATCA to observe 3.3 mm continuum emission from a sample of 15 southern T-Tauri stars, five in Lupus and ten in Chamaeleon. Compared with the Taurus star-forming cloud, the T-Tauri stars in Lupus and Chamaeleon are generally somewhat older, and the Lupus clouds are much richer in very low mass stars than the other clouds (Hughes et al. 1994). The sources IM Lup and WW Cha were also observed in spectral-line mode to search for $HCO^+$ as a tracer of the molecular gas. The observations of the Lupus sources were followed up with 1.4-mm observations using the Submillimeter Array (SMA). The sample and the observations are described in Sect. 3.2. The basic results are presented in Sect. 3.3 and further discussed in Sect. 3.4. We will summarise our results and draw some conclusions in Sect. 3.5.

## 3.2 Observations

### 3.2.1 Source selection

The ATCA was used to observe 15 southern T-Tauri stars (listed in Table 3.1) at 3.3 mm. The sources were selected to overlap with the sample observed in the c2d programme. We furthermore selected sources with strong 1.3 mm fluxes (Henning et al. 1993; Nürnberger et al. 1997) to improve the chances of detection at 3.3 mm.

The distances used in this work are $150 \pm 20$ pc to Lupus I (HT Lup, GW Lup) and Lupus II (IM Lup, RU Lup), $200 \pm 20$ pc to Lupus III (HK Lup) (Comerón 2008), and $160 \pm 15$ pc to Chamaeleon I (Whittet et al. 1997). The distances to most of these pre-main-sequence stars are not very well constrained (see, e.g., Comerón 2008; van Kempen et al. 2007, for discussions on the distances to the Lupus clouds). The distance to the isolated source T Cha, however, is known to be closer at $66^{+19}_{-12}$ pc (Hipparcos, van den Ancker et al. 1998).

### 3.2.2 ATCA observations

ATCA[1] observations were carried out in July 2003, October 2004, and August 2005. All sources were observed at 3.3 mm continuum in double sideband. The primary beam of the ATCA antennas is $\approx 35''$ at 3 mm. Each sideband consisted

[1]The Australia Telescope Compact Array is part of the Australia Telescope which is funded by the Commonwealth of Australia for operation as a National Facility managed by CSIRO.

of 32 channels and had an effective total bandwidth of 128 MHz. Furthermore, the sources WW Cha and IM Lup were observed in a dual mode: the lower sideband was a 512-channel band with an effective total bandwidth of 8 MHz to provide high-frequency resolution for detection of the $HCO^+$ $J$ = 1–0 line and the upper sideband was used as a wideband channel with again 32 channels and a total bandwidth of 128 MHz. These two sources were observed for a complete track to reach a similar RMS noise in the continuum as that for the other sources, and to maximise the possibility of detecting the $HCO^+$ $J$ = 1–0 line. The resulting velocity resolution of the narrow-band observations was 0.11 km $s^{-1}$, the velocity coverage was ∼24 km $s^{-1}$. The ATCA was in the EW214 configuration at the time of the observations in 2003 (three antennas equipped with 3 mm receivers, baselines of 31–107 metres) and in the H214C configuration in 2004 and 2005 (five antennas, baselines of 82–247 metres). The data were calibrated and reduced with the MIRIAD package (Sault et al. 1995). The quasars PKS 1622-297 and PKS 1057-797 served as gain calibrators for the Lupus and Chamaeleon sources, respectively, and the absolute fluxes were calibrated on Mars or Uranus. The calibration is estimated to have an uncertainty of ∼20 %. The passbands were calibrated on the quasars PKS 0537-441 and PKS 1253-055.

The phase centre was offset from the source position by 5″ to avoid possible artefacts. There was some overlap in the samples that were observed in the three runs. The 2004 data suffered badly from unstable weather and were not used in the analysis, whereas the 2003 and 2005 data were consistent. In 2003, there were only three ATCA antennas fitted with 3 mm receivers, resulting in a large and elongated beam. Five antennas with 3 mm receivers were available in 2005, greatly improving the resolution and beam shape of our observations. With the exception of HK Lup, which was only observed in 2003, we decided to use only the 2005 data for our analysis. For an overview of the ATCA observations, see Table 3.2.

### 3.2.3 SMA observations

The five Lupus sources in our sample were observed in double-sideband continuum (217 and 227 GHz, primary beam ∼ 55″) with the SMA[2] (Ho et al. 2004) on 28 April 2006. The data from both sidebands were combined, giving an effective bandwidth of 3 GHz. The SMA was in the compact configuration and baselines ranged from 5 to 52 metres. The low elevation of the sources as seen from Mauna

[2]The Submillimeter Array is a joint project between the Smithsonian Astrophysical Observatory and the Academia Sinica Institute of Astronomy and Astrophysics and is funded by the Smithsonian Institution and the Academia Sinica.

Table 3.1: Source list of sources observed with the ATCA.

| Source | Cloud | Age[a] (Myr) | Spectral type[b] | L[c] ($L_\odot$) | D[d] (pc) | When observed[e] |
|---|---|---|---|---|---|---|
| SY Cha | Cha I | 3–5 | M0 | 0.35 | 160 ± 15 | 2005 |
| CR Cha | Cha I | 1–2 | K0, K2 | 2.8 | 160 ± 15 | 2003†; 2005 |
| CS Cha | Cha I | 2–3 | K4 | 1.3 | 160 ± 15 | 2003†; 2005 |
| DI Cha | Cha I | 3–4 | G1, G2 | 8.9 | 160 ± 15 | 2005 |
| KG 28 | Cha I | ... | K7 | 1.1 | 160 ± 15 | 2005 |
| Glass I[f] | Cha I | 2–3 | K4 | 1.3 | 160 ± 15 | 2005 |
| KG 49 | Cha I | ... | ... | 15 | 160 ± 15 | 2005 |
| WW Cha | Cha I | 0.4–0.8 | K5 | 2.2 | 160 ± 15 | 2003†; 2005 |
| XX Cha | Cha I | 10–40 | M1 | 0.10 | 160 ± 15 | 2005 |
| T Cha | Isolated | > 12.5 | G2 | 1.3 | $66^{+19}_{-12}$ | 2003†; 2005 |
| HT Lup[g] | Lup I | 0.4–0.8 | K2 | 6.0 | 150 ± 20 | 2003†; 2005 |
| GW Lup | Lup I | 1.3–3.2 | M2 | 0.23 | 150 ± 20 | 2003†; 2005 |
| IM Lup | Lup II | 0.09–0.6 | M0 | 1.3 | 150 ± 20 | 2003†; 2005 |
| RU Lup | Lup II | 0.04–0.5 | K7-M0 | 2.1 | 150 ± 20 | 2003†; 2005 |
| HK Lup | Lup III | 0.7–1.4 | M0 | 0.62 | 200 ± 20 | 2003 |

[a] Ages adopted from Hughes et al. (1994), Lawson et al. (1996), and van den Ancker et al. (1998).

[b] Spectral types adopted from Herbig & Kameswara Rao (1972), Gauvin & Strom (1992), Hughes et al. (1994), Alcala et al. (1995), van den Ancker et al. (1998), and Comerón et al. (1999).

[c] Luminosities adopted from Hughes et al. (1994), Lawson et al. (1996), Chen et al. (1997), and van den Ancker et al. (1998).

[d] Distances adopted from Whittet et al. (1997), van den Ancker et al. (1998), and Comerón (2008).

[e] The observations marked with a † were not used in the analysis.

[f] This source is a binary with a separation of 2.″4; the spectrum quoted is that of component A.

[g] This source is a binary in 2MASS K-band images with a separation < 3″. The spectrum quoted includes both sources.

Table 3.2: Overview of the observations.

| Obs. dates | Freqs. covered (GHz) | $(u, v)$ range covered (k$\lambda$) | # Antennas used |
|---|---|---|---|
| | ATCA | | |
| 10 July 2003 | 89.999, 90.095 | 8-33 | 3 |
| 11 July 2003 | 89.999, 90.095 | 9-33 | 3 |
| 12 July 2003 | 89.999, 90.095 | 6-33 | 3 |
| 13 July 2003 | 89.999, 90.095 | 6-33 | 3 |
| 19 August 2005 | 89.181, 91.456 | 19-76 | 5 |
| 24 August 2005 | 89.180, 91.456 | 12-70 | 5 |
| | 90.000, 90.096 | 14-75 | 5 |
| 25 August 2005 | 89.176, 91.456 | 10-71 | 5 |
| 26 August 2005 | 89.176, 91.456 | 12-71 | 5 |
| 28 August 2005 | 89.176, 91.456 | 12-71 | 5 |
| | SMA | | |
| 28 April 2006 | 217.347, 226.892 | 4-53 | 8 |

Kea and the relatively short integration time of $\sim$ 30 minutes per source resulted in a rather elongated beam of $\sim 9 \times 2.5$ arcsec (natural weighting). The raw visibility data were calibrated and flagged with MIR, and the calibrated visibility data were analysed with MIRIAD. The gains were calibrated on the quasar PKS 1622-297, and the absolute fluxes and correlator passbands were calibrated on Uranus with an expected uncertainty of ~20 %. All eight antennas of the array were available at the time of the observations. For an overview of the SMA observations, see Table 3.2.

## 3.3 Results

### 3.3.1 Source fluxes

From the 15 sources that were observed with the ATCA in 2003 and 2005, ten were detected at better than $3\sigma$, with 3.3 mm fluxes ranging from $\sim$ 6 mJy up to $\sim$ 30 mJy. For those objects, both point sources and circular Gaussians were fitted in the $(u, v)$ plane, the results of which are presented in Table 3.3. Those sources that were detected at better than $5\sigma$ are shown in Fig. 3.1, overplotted on 2MASS K-band (2.1 $\mu$m) images. The positions of the infrared sources and the millimetre peaks agree very well.

Table 3.3: Basic results of ATCA observations at 3.3 mm.

| Source name | Continuum flux[a] (mJy) | | RMS[b] (mJy/beam) | Gaussian size (arcsec) | RA[a] (J2000) | Dec.[a] (J2000) | Beam size[c] (arcsec) | $\nu_{\rm eff}$ (GHz) |
|---|---|---|---|---|---|---|---|---|
| | (P) | (G) | | | | | | |
| SY Cha | < 4.8[d] | | 1.6 | - | 10 56 30.4 | -77 11 45.0 | $2.5 \times 2.2$ | 90.3 |
| CR Cha | 6.2 | 6.1 | 1.5 | < 1 | 10 59 06.9 | -77 01 39.7 | $2.5 \times 2.1$ | 90.3 |
| CS Cha | 5.9 | 8.8 | 1.5 | $1.65 \pm 0.96$ | 11 02 24.9 | -77 33 35.9 | $2.4 \times 2.2$ | 90.3 |
| DI Cha | < 3.9[d] | | 1.3 | - | 11 07 21.6 | -77 38 12.0 | $2.4 \times 2.2$ | 90.3 |
| KG 28 | < 3.9[d] | | 1.3 | - | 11 07 57.9 | -77 38 50.0 | $2.4 \times 2.3$ | 90.3 |
| Glass I | < 3.0[d] | | 1.0 | - | 11 08 15.1 | -77 33 59.0 | $2.4 \times 2.4$ | 90.3 |
| **KG 49** | 11.9 | 29.5 | 1.5 | $2.78 \pm 0.40$ | 11 08 38.6 | -77 43 52.1 | $2.4 \times 2.2$ | 90.3 |
| **WW Cha** | 25.9 | 33.1 | 1.2 | $1.32 \pm 0.16$ | 11 10 00.0 | -76 34 58.0 | $2.5 \times 2.2$ | 91.0 |
| XX Cha | < 4.5[d] | | 1.5 | - | 11 11 39.7 | -76 20 21.0 | $2.4 \times 2.2$ | 90.3 |
| T Cha | 6.4 | 7.0 | 1.0 | $0.78 \pm 1.03$ | 11 57 13.6 | -79 21 31.7 | $2.5 \times 2.4$ | 90.3 |
| **HT Lup** | 8.3 | 12.0 | 1.1 | $1.40 \pm 0.41$ | 15 45 12.9 | -34 17 30.8 | $2.4 \times 1.7$ | 90.0 |
| GW Lup | 8.5 | 9.5 | 1.9 | $0.98 \pm 1.22$ | 15 46 44.7 | -34 30 36.0 | $5.3 \times 1.7$ | 90.0 |
| **IM Lup** | 8.9 | 13.1 | 1.3 | $1.40 \pm 0.39$ | 15 56 09.2 | -37 56 06.3 | $2.3 \times 1.7$ | 91.5 |
| **RU Lup** | 12.7 | 15.6 | 1.0 | $0.99 \pm 0.32$ | 15 56 42.3 | -37 49 16.0 | $2.3 \times 1.7$ | 90.0 |
| HK Lup | 7.3 | 9.1 | 2.1 | $2.85 \pm 1.70$ | 16 08 22.5 | -39 04 46.3 | ill defined[e] | 90.1 |

NOTE. — Source name in boldface indicates that the source is resolved at 3.3 mm with the ATCA, see Sect. 3.3.2.

[a] Continuum flux and position are from fits in the $(u, v)$ plane. For sources that were detected at $3\sigma$, both the point-source flux (P) and the integrated flux for a Gaussian (G) are shown. For sources that were not detected, the coordinates of the phase centre are quoted.

[b] Calculated from the cleaned image.

[c] Restored beam, using natural weighting.

[d] Quoted value is $3\sigma$ upper limit.

[e] Large, elongated beam due to short integration time and availability of only three antennas with 3 mm receivers.

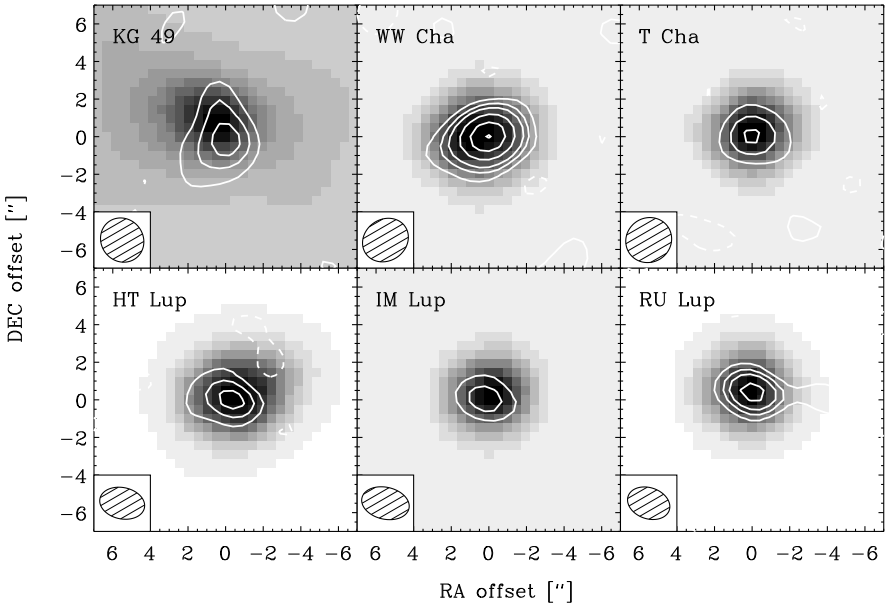


Figure 3.1: ATCA images of the $\lambda = 3.3$-mm continuum emission (contours), overplotted on 2MASS K-band (2.1 $\mu$m) images (grayscales). Contour levels are drawn at 2, 4, 6, 10, 15, and 20 times the noise level; negative contours are dashed. The positional offsets are with respect to the fitted coordinates (see Table 3.3).

Table 3.4 presents the results of the SMA 1.4-mm observations of the Lupus sources, which were all detected at better than $15\sigma$, with fluxes ranging from $\sim$ 70 mJy up to $\sim$ 210 mJy. For comparison, the SEST 1.3 mm single-dish fluxes from Nürnberger et al. (1997) are also shown.

### 3.3.2 Are the sources resolved?

A plot of the visibility amplitude as a function of baseline for each of our target sources is presented in Figs. 3.2 and 3.3. An amplitude that decreases as a function of baseline indicates a resolved source, suggesting that at least some of our sources are resolved. Note that in principle the resolved structure could be the protoplanetary disc, or the remnant centrally-condensed envelope around it. One can distinguish between the two by looking in more detail at the shape of the

Table 3.4: Basic results of SMA observations at 1.4 mm. For comparison, the SEST 1.3 mm single-dish fluxes from Nürnberger et al. (1997) are shown.

| Source name | Continuum flux[a] (mJy) | | RMS[b] (mJy/beam) | Gaussian size (arcsec) | RA[a] (J2000) | Dec.[a] (J2000) | $\nu_{\rm eff}$ (GHz) | SEST 1.3 mm[c] | |
|---|---|---|---|---|---|---|---|---|---|
| | (P) | (G) | | | | | | Flux (mJy) | RMS (mJy) |
| HT Lup | 73 | 77 | 4.0 | 1.01 ± 0.66 | 15 45 12.9 | -34 17 30.1 | 221.3 | 135 | 15 |
| GW Lup | 64 | 70 | 3.7 | 1.22 ± 0.48 | 15 46 44.8 | -34 30 35.7 | 221.3 | 106 | 18 |
| **IM Lup** | 188 | 214 | 4.3 | 1.33 ± 0.20 | 15 56 09.2 | -37 56 06.5 | 221.3 | 260 | 9 |
| **RU Lup** | 148 | 158 | 4.5 | 1.02 ± 0.32 | 15 56 42.3 | -37 49 15.9 | 221.3 | 197 | 7 |
| **HK Lup** | 89 | 101 | 3.9 | 1.43 ± 0.38 | 16 08 22.5 | -39 04 47.5 | 221.3 | 84 | 17 |

NOTE. — Source name in boldface indicates that the source is resolved at 1.4 mm with the SMA, see Sect. 3.3.2.

[a] Continuum flux and position are taken from fits in the $(u, v)$ plane. Both the point-source flux (P) and the integrated flux for a Gaussian (G) are shown.

[b] Calculated from the cleaned image.

[c] Nürnberger et al. (1997). The SEST fluxes are in general higher than the SMA fluxes, partly due to the slightly shorter effective wavelength, 1.3 mm (SEST) vs 1.4 mm (SMA).

amplitude vs $(u, v)$ distance curves. A disc shows a shallower profile at shorter baselines, levelling off to the flux of the integrated disc emission. A power-law envelope shows a flux that increases steeply towards the shortest baselines, and the total integrated flux can only be obtained with single-dish telescopes, observing with a larger beam. An illustrative example is provided by Fig. 3 in Jørgensen et al. (2005), who need a disc and an envelope to explain the amplitude as a function of baseline for the deeply embedded class 0 source NGC 1333 IRAS 2A.

The amplitude vs $(u, v)$ distance plot for KG 49 (Cha IRN) appears to indicate a resolved envelope rather than a disc. This is in line with the results of Henning et al. (1993) who find that the SED from 1 $\mu$m to 1 mm cannot be fitted with a disc, but is consistent with a spherically symmetric model with constant density and $A_V = 25$ mag. Furthermore, all other sources show silicates in emission around 10 $\mu$m, which is indicative of a disc without significant foreground absorption. KG 49 on the other hand does not show silicate emission around 10 $\mu$m. However, it does show bands of $H_2O$, CO, and $CO_2$ ice (Gürtler et al. 1999; Pontoppidan et al. 2003), which can be explained by a cold envelope. It thus appears that KG 49 is not a genuine T-Tauri star, but a less evolved object that is still embedded in an envelope. We will therefore disregard KG 49 in the further analysis in this work.

We consider a source to be resolved if the integrated flux of the fitted Gaussian is at least $2\sigma$ higher than the flux obtained from a point-source fit (see Tables 3.3 and 3.4). Note that for a point source the peak flux density equals the integrated flux. According to this definition, five of the detected sources (KG 49, WW Cha, HT Lup, IM Lup, RU Lup) are resolved by the ATCA, and three of the Lupus sources (IM Lup, RU Lup, HK Lup) are resolved by the SMA. In the case of KG 49 it is the envelope that is resolved, in the other cases the discs.

### 3.3.3 Opacity index

At low frequencies, i.e., in the Rayleigh-Jeans regime, the flux density, $F_\nu$, is related to frequency, $\nu$, by a power law: $F_\nu \propto \nu^\alpha$. One can determine the dust opacity index, $\beta$, where $\kappa_\nu \propto \nu^\beta$, from the observed spectral index, $\alpha$, through

$$\beta \approx (\alpha - 2)(1 + \Delta), \tag{3.1}$$

where $\Delta$ is the ratio of optically thick to optically thin emission from the disc (Beckwith et al. 1990; Beckwith & Sargent 1991; Rodmann et al. 2006).

Due to the frequency dependence of the dust opacity, protoplanetary discs are generally optically thick at short wavelengths and optically thin at long wavelengths. Optically thick emission cannot be neglected in the inner disc where column densities get very high, even at very long wavelengths. The ratio of optically

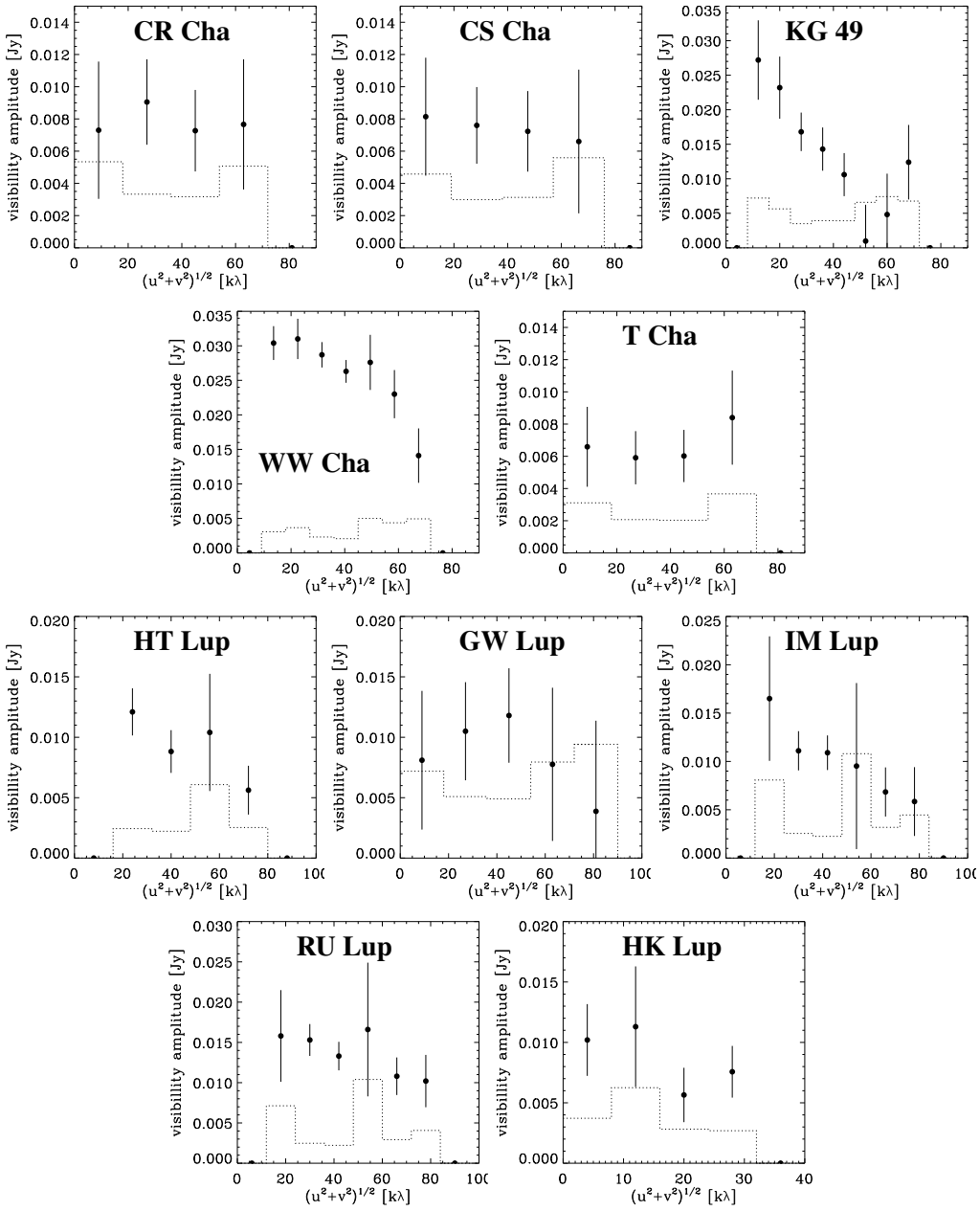


Figure 3.2: Amplitude vs $(u, v)$ distance for sources observed with the ATCA. The data points give the vector-averaged amplitude per bin, where the data are binned in annuli according to $(u, v)$ distance. The error bars show the statistical $1\sigma$ errors and the dotted lines give the expected amplitude for zero signal.

Table 3.5: SEST 1.3 mm fluxes from the literature, mm slopes, derived opacity indices, and disc masses.

| Source name | SEST 1.3 mm[a] Flux (mJy) | Mm slope[b] $\alpha$ | Opacity index[b] $\beta$ | Disc mass[c] $M_{\rm disc}$ ($M_\odot$) |
|---|---|---|---|---|
| SY Cha | < 172 | ... | ... | < 0.011 |
| CR Cha | 125 ± 24 | 3.2 ± 0.5 | 1.5 ± 0.6 | 0.014 |
| CS Cha | 128 ± 46 | 2.9 ± 0.5 | 1.0 ± 0.6 | 0.021 |
| DI Cha | 38 ± 11 | > 2.4 | > 0.5 | < 0.009 |
| KG 28 | ... | ... | ... | < 0.009 |
| Glass I | 70 ± 22 | > 3.4 | > 1.7 | < 0.007 |
| WW Cha | 408 ± 29 | 2.7 ± 0.7 | 0.8 ± 0.8 | 0.077 |
| XX Cha | < 252 | ... | ... | < 0.011 |
| T Cha | 105 ± 18 | 2.9 ± 0.5 | 1.1 ± 0.6 | 0.003 |
| HT Lup | 135 ± 15 | 2.5 ± 0.4 | 0.4 ± 0.5 | 0.025 |
| GW Lup | 106 ± 18 | 2.4 ± 0.4 | 0.5 ± 0.5 | 0.019 |
| IM Lup | 260 ± 9 | 3.2 ± 0.5 | 1.4 ± 0.5 | 0.027 |
| RU Lup[c] | 197 ± 7 | 2.5 ± 0.1 | 0.5 ± 0.1 | 0.032 |
| HK Lup | 84 ± 17 | 2.5 ± 0.4 | 0.7 ± 0.5 | 0.033 |

[a] Henning et al. (1993); Nürnberger et al. (1997).

[b] Calculated from SMA and ATCA fluxes (Gaussian fits) from this work and SEST fluxes, where available.

[c] Disc masses estimated from ATCA fluxes (Gaussian fits), assuming a gas-to-dust ratio $\Psi = 100$, a dust opacity at 3.3 mm $\kappa_\nu = 0.9$ cm$^2$ g$^{-1}$, and a dust temperature $T_{\rm dust} = 25$ K.

[d] Includes JCMT fluxes from Weintraub et al. (1989).

thick to optically thin emission coming from the disc is given by

$$\Delta \approx -p \times \left[(2-q)\ln\{(1-p/2)\bar{\tau}\}\right]^{-1}, \tag{3.2}$$

where $p$ and $q$ are the disc's surface density and temperature indices, and $\bar{\tau}$ is the average disc opacity at the frequency under consideration (see Beckwith et al. 1990, for details). Following Beckwith et al. (1990) and Rodmann et al. (2006), we used $p = 1.5$. $q$ is uniquely determined from the spectral index at wavelengths where the dust opacity is high ($\lambda \leq 100\mu$m), and from IRAS photometry we obtained values ranging from 0.4 to 0.7. $\bar{\tau}$ can in principle only be determined if

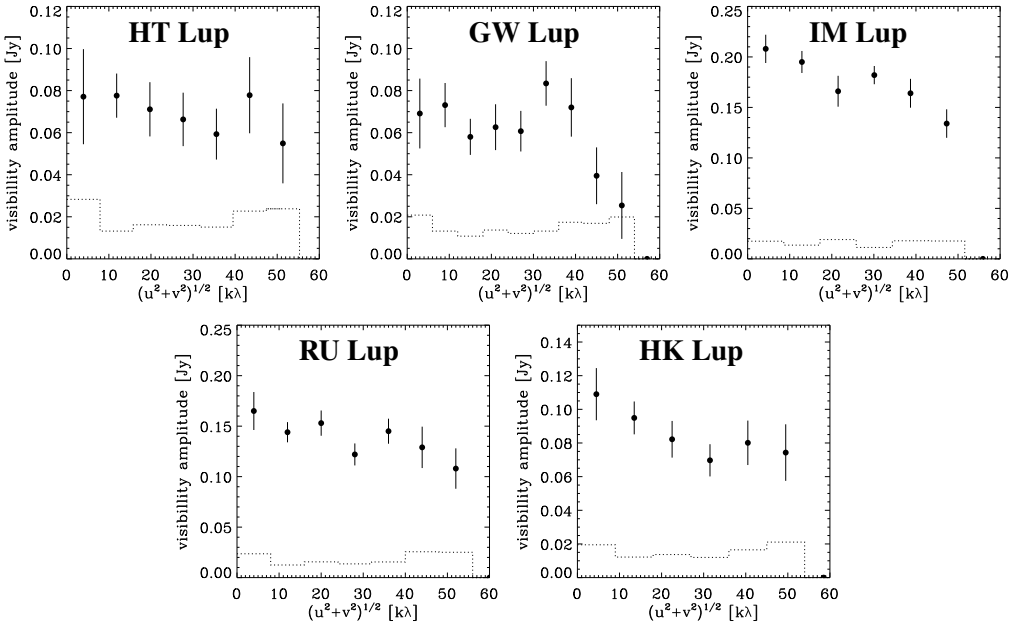


Figure 3.3: Same as Fig. 3.2 for sources observed with the SMA.

the physical disc radius is known. Rodmann et al. (2006) use $\bar{\tau} = 0.01$ at 7 mm. Taking $\beta = 1$ as a fiducial value for the opacity index, we adopt $\bar{\tau} = 0.02$ at 3.3 mm and find values for $\Delta$ ranging from 0.18 to 0.22.

The spectral index $\alpha$ and the opacity index $\beta$ were determined from the ATCA 3.3 mm fluxes and SEST 1.3 mm fluxes from the literature (Nürnberger et al. 1997; Henning et al. 1993). The uncertainties in $\alpha$ and $\beta$ are typically 0.5, due to both the large uncertainties in the absolute fluxes of the data points and to the relatively short wavelength range over which $\alpha$ was determined. For the Lupus sources, $\alpha$ was also determined with the SMA 1.4-mm fluxes included, giving consistent results. The robustness of the value for $\alpha$ is illustrated by Fig. 3.4, which shows the integrated fluxes from this work and single-dish (sub)millimetre fluxes from the literature for RU Lup (Weintraub et al. 1989; Nürnberger et al. 1997), along with the fitted slope: $\alpha = 2.5 \pm 0.1$. We thus find that the formal uncertainties in $\alpha$ and $\beta$ for the other sources are probably overestimates. Unfortunately, RU Lup is the only source for which currently observations at such short wavelengths are available. The low error in the fit to its data point illustrates that more observations, preferably over a larger wavelength regime, will help to better constrain values for

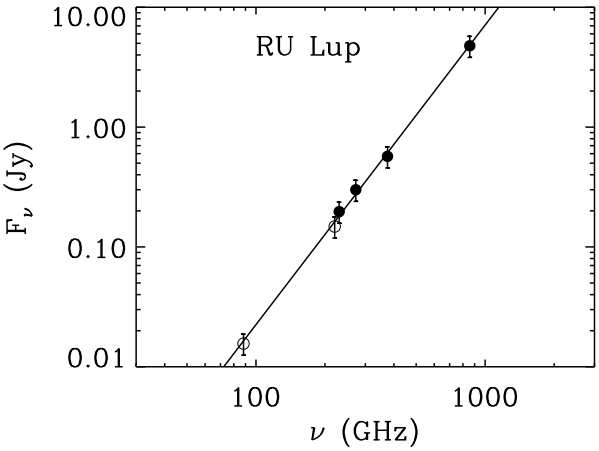


Figure 3.4: $F_\nu$ vs $\nu$ for RU Lup. Filled symbols show fluxes from single-dish observations (JCMT and SEST, Weintraub et al. 1989; Nürnberger et al. 1997), open symbols show the values for the interferometric observations from this work. All points fall on a line with $\alpha = 2.5 \pm 0.1$, where $F_\nu \propto \nu^\alpha$. This suggests that there is no extended emission over the size scale of the primary beams of the different telescopes, as may be the result of, e.g., a remnant envelope or ambient cloud material. Hence, no extended emission is filtered out in the interferometric observations.

$\alpha$, and hence $\beta$.

The values for $\alpha$ and $\beta$ for the sources in our sample are presented in Table 3.5. Fig. 3.5 shows the cumulative fraction of sources with given dust-opacity indices for our sample and that of Rodmann et al. (2006). Rodmann et al. corrected for the contribution of free-free radiation at 7 mm. We estimate the contribution of free-free radiation to be $\sim 5\%$ at 3.3 mm, and hence it is not necessary to correct for it at this wavelength. Fig. 3.4 illustrates that contamination from free-free emission is not an issue for RU Lup. The Kolmogorov-Smirnov test gives a probability of 58% that Rodmann et al.'s and our groups are drawn from the same distribution. However, the uncertainties in $\beta$ are still quite large, and are not taken into account by the standard Kolmogorov-Smirnov test.

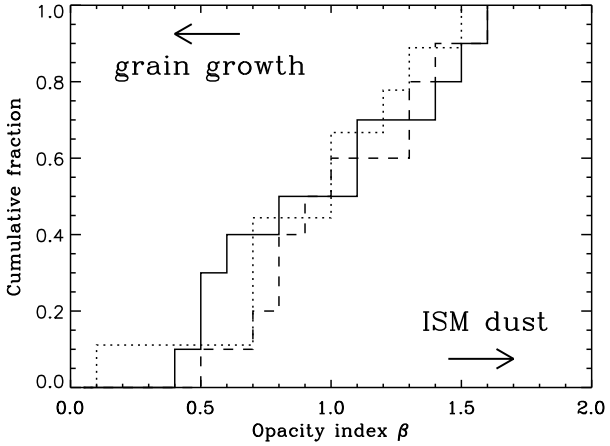


Figure 3.5: Cumulative number of sources with an opacity index less than a given value of $\beta$ for the sources in our sample (solid line), those studied by Rodmann et al. (2006) (dashed line), and those studied by Natta et al. (2004) (dotted line).

### 3.3.4 Disc masses

For optically thin discs, the disc mass $M_{\rm disc}$ is directly proportianal to the flux $F_\nu$ (see, e.g., Hildebrand 1983; Natta et al. 2000):

$$M_{\rm disc} = \frac{F_\nu \Psi D^2}{\kappa_\nu B_\nu(T_{\rm dust})}, \tag{3.3}$$

where $\Psi$ is the gas-to-dust ratio, $D$ is the distance to the source, $\kappa_\nu$ is the dust opacity, and $B_\nu(T_{\rm dust})$ is the brightness at the frequency $\nu$ for a dust temperature $T_{\rm dust}$, as given by the Planck function. We used the integrated fluxes from the Gaussian fits, and assumed $\Psi = 100$, $T_{\rm dust} = 25$ K, and $\kappa_\nu = 0.9$ cm$^2$ g$^{-1}$ at 3.3 mm [cf. Beckwith et al. (1990)[3]]. The derived disc masses for our sources range from $< 0.01$ up to 0.08 $M_\odot$, and are presented in Table 3.5. Note that the mass estimates are quite uncertain and may easily be off by a factor of 2, due to the uncertainties in the parameter values. Given the uncertainties in the measured quantities it is not meaningful to extend the analysis to include the contribution of optically thick emission and detailed disc structure.

[3]Note that Beckwith et al. (1990) estimate $\kappa_\nu = 0.1(\nu/10^{12}\ {\rm Hz})^\beta$ cm$^2$ g$^{-1}$, where $\kappa_\nu$ is the opacity index *for the gas and the dust combined*, i.e., with an implied gas-to-dust ratio. Our values for $\kappa_\nu$, however, are for the dust alone, and hence we have to account for the gas-to-dust ratio explicitly.

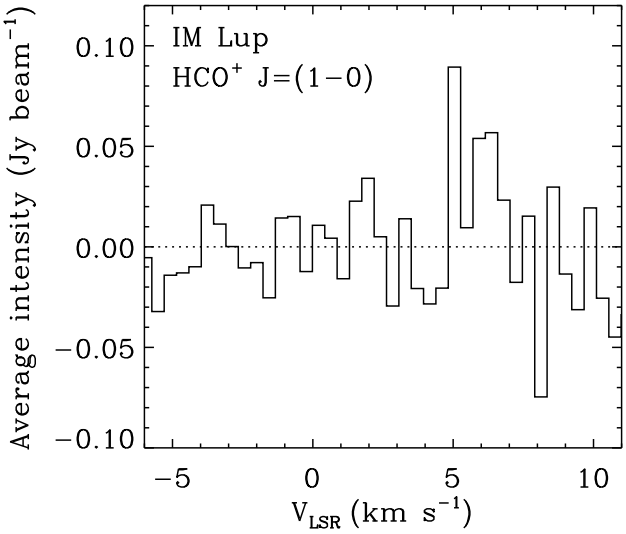


Figure 3.6: Spectrum of $HCO^+$ $J$ = 1–0 line emission observed from IM Lup, at the position of the peak continuum emission, binned to 0.44 km $s^{-1}$ velocity resolution, in the $2\farcs3 \times 1\farcs7$ synthesised beam.

### 3.3.5 Molecular line emission

Both IM Lup and WW Cha were observed in spectral-line mode to search for $HCO^+$ $J$ = 1–0 emission. In general, CO is a more easily detectable gas tracer in the millimetre regime, but since the ATCA does not presently have the capability to observe at frequencies above 106 GHz, $HCO^+$ was used to investigate the gas component of discs. We tentatively detect $HCO^+$ at $\sim$ 0.05 Jy $beam^{-1}$ in IM Lup, as presented in Fig. 3.6. Van Kempen et al. (2006) detected a double-peaked feature, consistent with a rotating gas disc, using JCMT observations of the $^{12}CO$ $J$ = 3–2 line. However, they find the line at $\sim$1 km $s^{-1}$ lower velocity. The cause of this discrepancy is unclear.

A ray-tracing programme (Hogerheijde & van der Tak 2000) was used to compute the line profile of $HCO^+$ $J$ = 1–0, using the model for IM Lup described in van Kempen et al. (2007). The abundance of $HCO^+$ was set to be $10^{-8}$ with respect to $H_2$ in areas with temperatures above 30 K, and $10^{-12}$ in areas with temperatures below 30 K. An intensity of $\sim$ 0.02 Jy $beam^{-1}$ was predicted, consistent with the observations within the uncertainties.

No $HCO^+$ line emission is detected to a limit of 97 mJy beam$^{-1}$ ($3\sigma$) in the direction of WW Cha. Combining our new results with those of Wilner et al. (2003) who detected $HCO^+$ in TW Hya, but not in HD 100546, we have two detections of $HCO^+$ and two non-detections. Data for more targets are required, in order to determine whether the presence of $HCO^+$ is related to the disc's evolutionary state.

## 3.4 Discussion and interpretations

### 3.4.1 Grain growth

About half the sources that are detected are spatially resolved. The inferred physical sizes (disc radii of $\sim$ 100 AU) indicate that the emission coming from the discs is predominantly optically thin at millimetre wavelengths. This is illustrated by the work of Testi et al. (2001), who do detailed modeling of the Herbig-Ae stars UX Ori and CQ Tau, and find that disc radii of $\sim$ 100 AU, combined with millimetre slopes of $\lesssim 3$ and 1.3 mm fluxes of $\sim 10^2$ mJy, are well explained by an opacity index $\beta = 1.0$. If we assume that all sources in our sample are optically thin at millimetre wavelengths, the opacity index $\beta$ can be determined. Seven out of ten detected sources have $\beta \lesssim 1$, which can be naturally explained by grain growth to millimetre and centimetre sizes (Draine 2006).

### 3.4.2 Comparison with Spitzer infrared data

Our values for $\beta$ indicate grain growth to sizes of millimetres and larger in the outer discs. The surface layers of the inner discs can be probed by infrared observations and, as noted in Sect. 3.1, the 10-$\mu$m feature indicates the growth of grains through changes in its strength and shape.

In Fig. 3.7 we compare the millimetre slope $\alpha$ as derived in Sect. 3.3 with the "strength" or peak 10-$\mu$m flux ($S_{\rm peak}^{10\mu{\rm m}}$) and to the "shape" or the ratio of the 11.3 to 9.8 $\mu$m flux ($S_{11.3}/S_{9.8}$) of the 10-$\mu$m silicate feature for those sources in our sample that overlap with the samples of Przygodda et al. (2003) and Kessler-Silacci et al. (2006). Here the normalized 10-$\mu$m spectra $S_\nu$ are given by

$$S_\nu = 1 + \frac{(F_\nu - F_{\nu,c})}{< F_{\nu,c} >}, \tag{3.4}$$

where $F_\nu$ is the observed spectrum and $F_{\nu,c}$ is the fitted continuum, and $< F_{\nu,c} >$ is the frequency-averaged continuum flux (see Kessler-Silacci et al. 2006 for details). We find a positive correlation between $\alpha$ and $S_{\rm peak}^{10\mu{\rm m}}$ and a negative cor-

relation between $\alpha$ and $S_{11.3}/S_{9.8}$, especially if we leave out the source T Cha, which shows emission from polycyclic aromatic hydrocarbons at 11.3 $\mu$m and may be considerably older than the other sources in the sample. As grains grow from submicron sizes to several microns, the 10-$\mu$m feature becomes weaker and less peaked (see, e.g., Kessler-Silacci et al. 2006), and thus the correlations we find may well indicate that once grain growth starts, the grains quickly grow from (sub)micron sizes to millimetre sizes and larger, both in the inner and outer discs. This is consistent with grain-growth models (Weidenschilling 1988, 1997; Dullemond & Dominik 2004b, 2005), which show that growth to metre sizes is rapid ($\sim 10^3$ yr at 1 AU; $\sim 10^5$ yr at 30 AU).

On the other hand, while a significant fraction of the dust has already grown to sizes of millimetres and centimetres, the infrared data indicate that micron-sized grains are also still present, at least in the surface layers. This may be explained by assuming that not only grain growth, but also aggregate fragmentation takes place in the discs (Dullemond & Dominik 2005). After about $10^4$ years a semi-stationary state is reached for sizes below $a \lesssim 1$ cm, which may last for several $10^6$ years.

Note that Fig. 3.7 shows a trend rather than a bimodal distribution. Dullemond & Dominik (2005) suggest fragmentation of grains to allow for the semi-stationary state that is observed in the discs around T-Tauri stars. If the correlation between the 10-$\mu$m feature and the millimetre slope is confirmed by a more extensive dataset, it would indicate that when aggregates are fragmented in collisions, the size of the fragments increases as the aggregate sizes increase. Hence, when the largest particles grow from millimetre to centimetre sizes, the submicron-sized grains are no longer replenished, and the 10-$\mu$m feature – tracing the upper layers of the disc where the stirred-up small particles reside – flattens while the millimetre slope – which traces the midplane where the largest particles are present – becomes shallower.

We also compared $\alpha$ to the spectral index over the 13 to 35 $\mu$m range from Kessler-Silacci et al. (2006). However, $\alpha$ could only be determined for five of the sources in Kessler-Silacci et al., and no obvious correlation is found for this small sample.

### 3.4.3 Comparison with Herbig-Ae/Be stars

It is interesting to note that Acke & van den Ancker (2004) do *not* find a correlation between the 10-$\mu$m silicate feature and the (sub)millimetre spectral index for their sample of 26 Herbig-Ae/Be stars. On the other hand, Acke et al. (2004) *do* find a correlation between the shape of the mid-IR (12–60 $\mu$m) SED and the

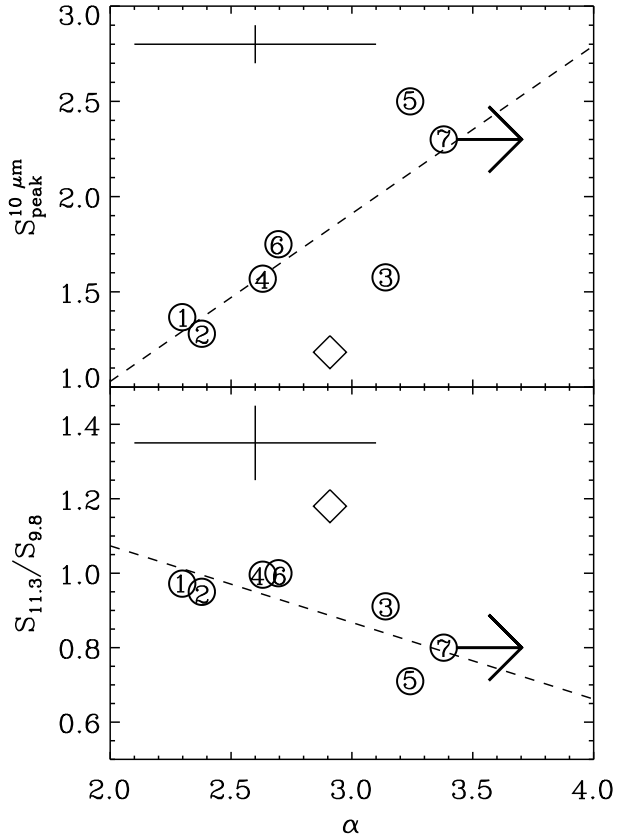


Figure 3.7: Slope in the millimetre regime vs the peak 10-$\mu$m flux (upper panel) and the ratio of the 11.3 to 9.8 $\mu$m flux (lower panel) of the 10-$\mu$m silicate feature, for those sources in our sample for which data are available. 1=HT Lup, 2=GW Lup, 3=IM Lup, 4=RU Lup, 5=CR Cha, 6=WW Cha, 7=Glass I. The source T Cha is depicted with a diamond.

(sub)millimetre slope in their sample. They interpret this finding as a correlation between disc geometry and grain size: as grains grow, the disc structure evolves from flared to geometrically flat (see, e.g., Dullemond 2002). For the twelve sources in our sample for which it was possible to determine $\alpha$, we determined the non-colour-corrected *IRAS* [12]–[60] colour and compared this to $\alpha$. No clear correlation was found, consistent with the above lack of correlation with

the 13–35 $\mu$m spectral index. This may indicate that grain growth has a less dramatic effect on the geometry of discs around the low-mass T-Tauri stars than on the intermediate-mass Herbig-Ae/Be stars, or that *IRAS* fluxes are contaminated by other (extended) emission in the large *IRAS* beams.

Natta et al. (2004) did a study similar to ours for a sample of six isolated Herbig-Ae stars and three T-Tauri stars. They estimated $\beta$ in two different ways, firstly using only interferometric data, and secondly with single-dish data included. Their results are included in Fig. 3.5, where the values for $\beta$ with the single-dish data included were used for comparison. According to the Kolmogorov-Smirnov test there is a 65% probability that the sample of Natta et al. and our sample are drawn from the same distribution. It is interesting to note that in general the sources in Natta et al.'s sample are considerably older than those sources in the current work and that of Rodmann et al. (2006). This may be an extra indication that the size distribution of grains in protoplanetary discs remains stationary for several Myr once sizes of millimetres are reached.

## 3.5 Concluding remarks

We used the ATCA to make interferometric observations of fifteen southern T-Tauri sources at 3.3 mm. Ten of the sources are located in Chamaeleon, the remaining five in Lupus. The Lupus sources were also observed at 1.4 mm with the SMA. The main results are as follows.

- Five of the Chamaeleon sources were detected at the $3\sigma$ level or better with the ATCA, for the other five sources we have strict upper limits.
- All five Lupus sources were detected at better than $3\sigma$ with the ATCA, and at better than $15\sigma$ with the SMA.
- Five of the ten detected sources are spatially resolved with the ATCA, and two of the five Lupus sources are resolved with the SMA. This indicates that the emission coming from these sources is optically thin.
- Adopting optically thin emission for all sources in our sample, we estimated the opacity index $\beta$. We find that $\beta \lesssim 1$ for seven of the ten detected sources. Such values for $\beta$ can be naturally explained by grain growth up to millimetre sizes and beyond.
- We find a tentative correlation between the millimetre slope and the peak 10-$\mu$m flux and ratio of the 11.3 to 9.8 $\mu$m flux of the 10-$\mu$m silicate feature. This indicates that grain growth takes place in the outer disc and in the

surface layers of the inner disc simultaneously. It also confirms earlier findings that agglomerate destruction must take place in the disc to preserve the small grain population. If confirmed by more extensive datasets, this correlation may be an indication that larger aggregates produce larger particles when fragmented in collisions.

- $HCO^+$ was tentatively detected in IM Lup, and was not seen in WW Cha.

This type of work will be greatly assisted by the upcoming 7 mm upgrade for the ATCA, as well as by the installation of a new correlator via the Compact Array Broadband Backend project. Estimating the millimetre slope over a wavelength range up to 7 mm will reduce the error in $\alpha$ – and hence in $\beta$ – from $\sim 0.5$ to $\sim 0.2$. At these longer wavelengths, however, the contribution of free-free emission becomes important, and lower-frequency measurements are required to separate the various contributions. A pilot study to determine the contribution of free-free emission at centimetre wavelengths in our sources is in progress.

The capability to observe the continuum across a 2 GHz bandwidth, as opposed to the current 128 MHz, will provide a marked increase in sensitivity, allowing more discs to be detected. Furthermore, as the new generation of (sub)millimetre interferometers, notably eSMA, CARMA, and ALMA, becomes available to the scientific community, it becomes possible to resolve the circumstellar discs at millimetre and submillimetre wavelengths down to subarcsecond scales. A survey of a large sample of objects, in different clouds, and at higher resolution will greatly enhance our understanding of the timescale for grain growth and the building of planetary systems as a function of disc radius.

## Acknowledgements

We would like to thank the ATNF for their hospitality and assistance, and specifically Tony Wong for extensive assistance during the observations and the data reduction. SMA staff, in particular Alison Peck, are thanked for scheduling observations of the Lupus sources as a filler programme and for carrying out the observations. Partial support for this work was provided by a Netherlands Research School For Astronomy network 2 grant, and by an Netherlands Organisation for Scientific Research Spinoza grant. CMW acknowledges financial support from an ARC Australian Research Fellowship. We are grateful to Jackie Kessler-Silacci for providing us with infrared data, and to Tim van Kempen for useful discussions on IM Lup and calculating the $HCO^+$ emission in his model. Finally, we would like to thank our referee, Claire Chandler, for useful comments that significantly improved this paper.

# Chapter 4

# Grain growth across protoplanetary discs: 10-$\mu$m feature versus mm slope


## Abstract

Young stars are formed with dusty discs around them. The dust grains in the disc are originally of the order of 0.1 $\mu$m. Models predict that these grains will grow in size through coagulation. Observations of the silicate features around 10 and 20 $\mu$m are consistent with a gradual growth from sub$\mu$m to $\mu$m sizes whereas the slope of the spectral energy distribution (SED) at mm and cm wavelengths traces growth up to mm sizes and larger. Grain growth in discs around pre-main-sequence stars is probed in the surface layers of the inner disc by the silicate features and in the mid-plane of the outer disc by the (sub)mm slopes in the SED. We here look for a correlation between these two growth indicators. A large sample of T-Tauri stars was observed with the Spitzer Space Telescope at 5–13 $\mu$m and a subsample was observed with the SMA, ATCA, CARMA, and VLA at mm wavelengths. We complement this subsample with data from the literature to maximise the overlap between $\mu$m and mm observations and search for correlations in the grain-growth signatures. Synthetic spectra are produced to determine which processes may produce the dust evolution observed in protoplanetary discs. Disc masses in the range $<$ 0.01 to 0.07 $M_\odot$ are obtained. The observations show that the strength and the shape of the 10-$\mu$m silicate feature correlate with the slope of the SED between 1 and 3 mm for the sample as a whole. The modelling results confirm that the 10-$\mu$m feature becomes flatter and the mm slope shallower with increasing maximum grain size. Assuming a disc with more small grains in the outer disc and more large grains in the inner disc does not enhance the effect. Other processes, such as the flaring angle or the inclination under which the system is observed, usually affect only the mm slope or only the 10-$\mu$m feature. The modelling results suggest that, as grains grow, first the 10-$\mu$m feature becomes weaker and later the mm slope gets shallower. This quite naturally explains the grouping of sources according to star-forming region in the 10-$\mu$m-feature vs mm-slope diagram. Care must be taken when interpreting the size of the grains in the discs from the strength of the 10-$\mu$m feature alone.



Dave Lommen, Ewine van Dishoeck, Chris Wright, Sarah Maddison,
David Wilner, Demerese Salter, Michiel Min, Huib Jan van Langevelde,
Geoff Blake, Tyler Bourke, and Remco van der Burg



To be submitted to Astronomy & Astrophysics

## 4.1 Introduction

The InfraRed Spectrograph (IRS) on-board the Spitzer Space Telescope has provided a wealth of mid-infrared spectra from discs around pre-main-sequence stars (e.g., Kessler-Silacci et al. 2006; Furlan et al. 2006). The spectrum of these objects between 5 and 30 $\mu$m is often dominated by silicate emission. Most prominent are the amorphous features at 10 and 20 $\mu$m. It was found that the varying strength and the shape of these features can be naturally explained by different grain sizes in the upper layers of the inner disc (Kessler-Silacci et al. 2006), confirming earlier results from the Infrared Space Observatory (e.g., Bouwman et al. 2001) and from the ground (e.g., Przygodda et al. 2003).

Because the 10-$\mu$m feature only probes the surface layers of the inner disc, a stronger, more peaked feature could also be due to the settling of larger, micron-sized grains towards the mid-plane. As the larger grains settle and the small ones remain suspended in the upper layers, the surface becomes dominated by small grains, creating a strong silicate band. Dullemond & Dominik (2008) investigated this idea through theoretical models. They find that settling can in principle explain the different shapes of the 10-$\mu$m feature, but only in quite specific cases, so that overall grain growth is still the most likely explanation. On the other hand, Voshchinnikov & Henning (2008) find that porosity and the inclusion of crystalline silicates may also have some effect on the shape and strength of the 10-$\mu$m feature. Recent interferometric observations of the 10-$\mu$m spectral region from $\sim$1 and 2-3-$M_\odot$ objects show that the grains closer to the central star are both larger and more crystalline than those further out in the disc (see, e.g., the recent review by van Boekel 2008). Hence, the evolution of the 10-$\mu$m feature may be caused by a combination of grain growth and crystallisation and appears to progress from the inner disc outwards.

Whereas the mid-infrared potentially provides information on the growth of grains from interstellar, submicron sizes to sizes of several microns, the growth to larger sizes can only be probed by submillimetre (submm), millimetre (mm), and occasionally centimetre (cm) observations. Ground-breaking work was done by Beckwith et al. (1990) and Beckwith & Sargent (1991), both analytically studying the emission of dust grains and observing a large sample of young stellar objects at mm wavelengths. More recently, Andrews & Williams (2005) did a sensitive submm continuum single-dish survey of 153 young stellar objects in the Taurus-Auriga star-formation region, including a large amount of archival and literature data. They found that the submm slope between 350 $\mu$m and 1.3 mm could be well described by $\alpha = 2.0 \pm 0.5$, where $F_\nu \propto \nu^\alpha$, while the value for the interstellar medium is $\alpha \approx 3.7$ (cf. Draine 2006). Andrews & Williams (2005) inter-

preted this shallow slope as a combined effect of an optically thick contribution and grain growth. It should be noted, however, that the sources in this study were unresolved, and the (sub)mm emission may have a significant contribution from surrounding (envelope) material. More recently, interferometric studies of several dozen T-Tauri stars gave values of $\alpha \lesssim 3.0$ (e.g., Rodmann et al. 2006, and Chapter 3). From this mm slope one can estimate the opacity index $\beta \approx 1.2 \times (\alpha - 2.0)$ (Rodmann et al. 2006) and values of $\beta \approx 1.0$ for $\lambda \gtrsim 1$ mm were found. Such a slope can be naturally explained by a significant fraction of grains at least several mm in size present in the discs (Draine 2006). A subsample of the sources presented in Chapter 3 overlapped with the Spitzer Infrared Spectrograph (IRS) observations published by Kessler-Silacci et al. (2006) and in Chapter 3 we show a tentative correlation between the mm slope of the spectral energy distribution (SED) and the strength and shape of the 10-$\mu$m silicate feature for these sources.

Acke et al. (2004) calculated the (sub)mm spectral indices of 26 Herbig-Ae/Be stars, for which the infrared SED could also be determined. They find a correlation between the strength of the ratio of the near- to mid-infrared excess and the slope of the (sub)mm energy distribution for these sources, which they attribute to a correlation between the disc geometry (flared versus self-shadowed) and the size of the grains in the disc. However, the authors do not find a correlation between the strength and the shape of the 10-$\mu$m silicate feature and the (sub)mm spectral index (see also Acke & van den Ancker 2004).

In this Chapter, we aim to investigate further the tentative correlation presented in Chapter 3 for a larger sample. A subsample of sources studied with the Spitzer IRS were observed with mm interferometers at longer wavelengths (Section 2). Interferometers were used to ascertain that the emission is dominated by disc emission, as extended emission from surrounding material will be filtered out. Also, spatially resolving the disc ensures that the emission is not optically thick. The results of the observations are shown in Section 3. In Section 4, we present model results for discs that were studied using an advanced radiative-transfer tool. The observations and models are compared and discussed in Section 5. A few conclusions are drawn in Section 6.

## 4.2 Observations

For this study, we compared Spitzer IRS observations of the 10-$\mu$m feature with mm observations from the Very Large Array (VLA, operated by NRAO[1]), the

[1]The National Radio Astronomy Observatory is a facility of the National Science Foundation operated under cooperative agreement by Associated Universities, Inc.

Combined Array for Research in Millimeter-wave Astronomy (CARMA[2]), the Submillimeter Array (SMA[3]), and the Australia Telescope Compact Array (ATCA[4]). A full log of the observations is listed in Sect. 4.7.

### 4.2.1 Source selection and Spitzer data

To look for possible environmental effects, sources in a total of five star-forming regions were included, spread over the constellations Lupus, Chamealeon, Corona Australis, Serpens, and the Gum nebula at distances of about 150–200, 160, 130, 260, and 400 pc, respectively, see Table 4.1. The sources were pre-selected to have a large spread in the strengths and shapes of the 10-$\mu$m features from Spitzer IRS data, mainly the "From Molecular Cores to Planet-forming Discs" programme (c2d, Evans et al. 2003, Program IDs 139 and 172–179) and the "The evolution of dust mineralogy in southern star forming clouds" programme (C.M. Wright PI, Project ID 20611). The spectra from the c2d project were previously published in Kessler-Silacci et al. (2006) and Olofsson et al., (2009, in prep.). Program P20611 includes Spitzer IRS observations from embedded YSOs, T-Tauri stars, and Herbig/Vela-type stars. The results for the T-Tauri stars are presented in this work. All data were re-reduced for this work using the c2d IRS reduction pipeline (Lahuis et al. 2006). Spectra were obtained both integrated over the full aperture of the instrument as well as convolved with the point spread function (PSF) at each wavelength. The Full-Aperture extraction method was used, unless the final spectrum quality of the PSF extraction method was considerably better. Furthermore, only data from the short-low module (SL, 5.2–14.5 $\mu$m) data were included, unless data from the short-high module (SH, 9.9–19.6 $\mu$m) were present and of significantly higher quality.

In binary systems, it is possible that circumstellar discs get truncated due to binary interaction, affecting grain growth in the discs. To check for such effects, a number of binaries were included in the sample. Furthermore, the sources were selected to include so-called "cold discs" (e.g., Brown et al. 2007). The cold discs

[2]Support for CARMA construction was derived from the Gordon and Betty Moore Foundation, the Kenneth T. and Eileen L. Norris Foundation, the Associates of the California Institute of Technology, the states of California, Maryland, and Illinois, and the National Science Foundation. Ongoing CARMA development and operations are supported by the National Science Foundation under a cooperative agreement, and by the CARMA partner universities.

[3]The Submillimeter Array is a joint project between the Smithsonian Astrophysical Observatory and the Academia Sinica Institute of Astronomy and Astrophysics and is funded by the Smithsonian Institution and the Academia Sinica.

[4]The Australia Telescope Compact Array is part of the Australia Telescope which is funded by the Commonwealth of Australia for operation as a National Facility managed by CSIRO.

Table 4.1: Distances to and ages of star-forming clouds.

| Cloud | Age[a] (Myr) | D[b] (pc) |
|---|---|---|
| Lupus 1 and 2 | $\lesssim 1$ | 150 ± 20 |
| Lupus 3 | 1–1.5 | 200 ± 20 |
| Lupus 4 | 1–1.5 | 165 ± 15 |
| Cha I | 3–4 (southern subcluster)<br>5–6 (northern subcluster) | 160 ± 15 |
| Corona Australis | 5–13 | ∼130 |
| Serpens | 1–15 | 259 ± 37 |
| Gum nebula | 2–6 | 400 ± 60 |
| Taurus-Auriga | 1–10 | 140 ± 15 |

[a] Ages adopted from Heiles (1998), Comerón et al. (2003), James et al. (2006), Luhman (2007), Comerón (2008), Kenyon et al. (2008), Neuhäuser & Forbrich (2008), Oliveira et al. (2009), and references therein.

[b] Distances adopted from Brandt et al. (1971), Kenyon et al. (1994), Straižys et al. (1996), Whittet et al. (1997), Bertout et al. (1999), de Zeeuw et al. (1999), Comerón (2008), Neuhäuser & Forbrich (2008), and references therein.

show a lower flux in the mid-infrared, which can be naturally explained by a lack of warm dust close to the star. Several of the cold discs were recently found to be circumbinary discs, with a large hole or gap in the centre, e.g., Espaillat et al. (2007, CS Cha), Guilloteau et al. (2008, HH 30). However, some cold discs are single stars, requiring a different mechanism to clear the inner discs of small, hot grains (e.g., Pontoppidan et al. 2008). One such mechanism could be grain growth into larger particles. A number of cold discs selected from the samples of Brown et al. (2007) and Merín et al. (2008) were included in our source list with the aim to explore this possibility. A full list of the 38 selected sources is given in Tables 4.2 and 4.3. Of these, 28 turn out to have a detected 10-$\mu$m feature and 13 yield a mm slope.

### 4.2.2 SMA observations

A total of 14 sources (including one binary) were observed with the SMA for the project 2007B-S033. The observations were carried out on 14 March and 19 April 2008. The data of 14 March were unusable due to phase instabilities. On 19 April, the phases were stable, and the zenith optical depth at 225 GHz was around $\tau_{225} = 0.13$ all through the night. Physical baselines ranged from 5.8 to 131 metres, resulting in a synthesised beam of about $4.8 \times 2.8$ arcsec (natural weighting). The two sidebands were combined into one continuum channel to improve the signal-to-noise ratio, resulting in an effective wavelength of 1.33 mm.

The sources VV CrA (binary), S CrA, and DG CrA were observed as part of the SMA "filler" project 2008A-S111 on 1 October 2008. Only six of the eight antennas were available for this track. However, $\tau_{225} \approx 0.1$ and the phases were stable, resulting in extremely good data. The synthesised beam of the resulting maps was about $5.0 \times 2.1$ arcsec (natural weighting). The correlator was tuned to 218 and 228 GHz. Combination of the two sidebands resulted in an effective wavelength of 1.35 mm. The absolute flux calibration of the SMA observations is estimated to be accurate to better than 20%.

### 4.2.3 ATCA observations

The data for the ATCA project C1794 were taken over the period July to August 2008 when the array was in the H214 configuration. A total of 15 sources were observed: 14 sources (including the binary Sz 65 + Sz 66) were observed at 3 mm and 11 sources at 7 mm. The weather changed considerably over the course of the observations. A short indication of the circumstances for each day is included in Sect. 4.7. Physical baselines ranged from 82 to 247 metres, resulting

in synthesised beam sizes of about 2 arcsec at 3 mm and about 4 arcsec at 7 mm. Combining the two sidebands in the 3 mm band resulted in an effective wavelength of 3.17 mm, those taken in the 7 mm band in an effective wavelength of 6.82 mm. The absolute flux calibration is estimated to be accurate to about 25%.

### 4.2.4 CARMA observations

A total of 13 sources located in Serpens were observed with the CARMA at 1 and 3 mm in the period April to June 2008 for project c0165. Weather conditions varied over the course of the observations, with a typical water path length of 3–6 mm. The calibrator originally selected for the observations at 1 mm, 1743-038, turned out to be too weak to perform a decent gain calibration, rendering most of the C-configuration observations unusable. For the second part of the observations the telescope was in the D configuration (baselines 11-148 metres), yielding a synthesised beam of about $3 \times 2$ arcsec at 1 mm and about $6 \times 4$ arcsec at 3 mm. The effective wavelength of the 1 mm-band observations was 1.33 mm, that of the 3 mm-band observations 3.15 mm. The absolute flux calibration is estimated to be accurate to about 30%.

### 4.2.5 VLA observations

Of the 13 sources in the Serpens star-forming region observed with the CARMA, eight were observed with the VLA at 0.7, 1.3, 3.6, and 6.3 cm under programme AL720. The observations were carried out from 10–15 March, when the array was in the C configuration, with baselines of up to 3.6 km and a synthesised beam of about 0.5 arcsec at 0.7 cm. All observations were performed in the default continuum mode in which, at each frequency, the full 100 MHz bandwidth was used in two adjacent 50 MHz bands. Weather conditions were good in general, with only some clouds forming towards the ends of the tracks carried out on 10 and 13 March. However, a few hours of observing time were lost at the end of the last two tracks due to high winds. The accuracy of the absolute flux calibration is estimated to be about 20% at 0.7 and 1.3 cm and better than 10% at 3.6 and 6.3 cm.

Table 4.2: List of sources in Chamaeleon, Lupus, Corona Australis, and the Gum nebula. The details of the mm observations can be found in Sect. 4.7 and the coordinates of the sources in Sect. 4.8.

| Source | Sp. T. | Cloud | Spitzer | Comments |
|---|---|---|---|---|
| | | Vela | | |
| HBC 553 | M1.5 | Gum | Wright | |
| HBC 556 | M4 | Gum | Wright | |
| HBC 557 | K3: | Gum | Wright | |
| HBC 559 | | Gum | Wright | |
| HBC 560 | K8 | Gum | Wright | |
| HBC 561 | K8 | Gum | Wright | Binary[a] |
| | | Chamaeleon | | |
| SZ Cha | K0e | Cha I | GTO | |
| Sz 32 | K4.7 | Cha I | c2d | |
| | | Lupus | | |
| IK Lup | K7 | Lupus 1 | Wright | Binary[b] |
| Sz 66 | M2 | Lupus 1 | Wright | Binary[b] |
| HN Lup | M1.5 | Lupus 1 | Wright | |
| Sz 77 | M0 | Lupus 1 | Wright | |
| IM Lup | M0 | Lupus 2 | c2d | |
| RY Lup | G0V: | Lupus 3 | c2d | |
| MY Lup | | Lupus 4 | Wright | |
| EX Lup | M0 | Lupus 3 | c2d | |
| Sz 91 | M0.5 | Lupus 3 | — | Circumbinary[c] |
| Sz 96 | M1.5 | Lupus 3 | c2d | |
| Sz 111 | M1.5 | Lupus 3 | — | Cold disc |
| SSTc2d J161029.57-392214.7 | | Lupus 3 | c2d | Cold disc |
| SSTc2d J161159.81-382338.5 | | Lupus 3 | c2d | |
| RX J1615.3-3255 | K5 | Isolated | c2d | |
| | | Corona Australis | | |
| S CrA | K3 | CrA | Wright | Binary[d] |
| DG CrA | | CrA | Wright | |
| VV CrA | K7 | CrA | Wright | Binary[e] |

[a] Separation 0.″63 (Correia et al. 2006).

[b] IK Lup (Sz 65) and Sz 66 form a binary with a separation of 6.″4.

[c] Binary star inside IRAC or MIPS point spread functions (Merín et al. 2008).

[d] Separation 1.″3 (e.g., Forbrich et al. 2007, and references therein).

[e] Separation 2.″0.

Table 4.3: List of sources in Serpens. The details of the mm and cm observations can be found in Sect. 4.7 and the coordinates of the sources in Sect. 4.8.

| Source | Sp. T. | Cloud | Spitzer | Comments |
|---|---|---|---|---|
| | Serpens | | | |
| SSTc2d J182805.03+000659.3 | M4±1 | Serpens | c2d | |
| VV Ser | A2e... | Serpens | c2d | Herbig Ae |
| SSTc2d J182850.21+000949.7 | M5±4 | Serpens | c2d | |
| SSTc2d J182858.09+001724.5 | G3±5 | Serpens | — | Cold disc |
| SSTc2d J182900.90+002931.6 | K7±2 | Serpens | c2d | |
| CoKu Ser-G3 | K0±7 | Serpens | c2d | |
| IRAS 18268-0025 | | Serpens | c2d | |
| SSTc2d J182936.20+004216.8 | F9±5 | Serpens | c2d | |
| SSTc2d J182944.11+003356.1 | M0±1.5 | Serpens | c2d | |
| EC 82 | M0 | Serpens | c2d | |
| EC 90 | M4±2 | Serpens | c2d | Binary[a] |
| EC 97 | | Serpens | c2d | |
| GSC 00446-00153 | F3V | Serpens | — | |

[a] Separation 1.″5 (e.g., Ciardi et al. 2005, and references therein).

## 4.3 Results

### 4.3.1 Mm and cm source fluxes and disc masses

A full log of the results is listed in Sect. 4.8. The results of the interferometric observations at 1, 3, and 7 mm are listed in Tables 4.4 and 4.5.

From the eight sources in Lupus observed with the SMA, four were detected. The four undetected sources had so far also escaped detection in mm surveys, with upper limits quoted for Sz 91 and Sz 96 by Nürnberger et al. (1997) and SSTc2d J161029.6-392215 and SSTc2d J161159.8-382338 being newly detected Spitzer sources. Note, however, that the observations presented here went a factor of two to three deeper those of Nürnberger et al. (1997). Six sources in Lupus were observed with the ATCA at 3.2 mm and all were detected. Five sources were observed at 6.8 mm, of which only one, IM Lup, was detected. MY Lup would have been detected at 6.8 mm with a signal-to-noise ratio of about ten if it had a similar mm slope as IM Lup. However, IM Lup's mm slope between 3.2 and 6.8 mm is rather shallow: $\alpha_{3-7} = 1.82$ (see Table 4.6). Indeed, this is considerably more shallow than the value found for $\alpha$ in Chapter 3 ($3.2 \pm 0.5$), or from interpolating the fluxes at 1.3 and 3.3 mm given in Pinte et al. (2008) ($\alpha_{1-3} = 2.8$).

Three sources in the Gum nebula were observed with the ATCA at 3.2 and at 6.8 mm. None of the sources was detected at either wavelength down to $3\sigma$ upper limits of ~3 mJy at 3.2 mm and of ~0.5 mJy at 6.8 mm. This can be attributed to the large distance between us and this star-forming region. If the sources in the Gum nebula had similar fluxes as those in the Lupus clouds, they would have had a flux of ~0.7 mJy, which is below the noise level. Note that, although the Vela molecular ridge has been observed at mm wavelengths (Massi et al. 1999, 2007), no published mm data of the Gum nebula exist in the literature.

The source SZ Cha was detected at 2.3 mJy at 3.2 mm and was not observed at 6.8 mm. Sz 32 was not detected down to a $3\sigma$ upper limit of 2.9 mJy at 3.2 mm. It was, however, detected with a flux of 0.77 mJy at 6.8 mm.

VV CrA and S CrA were clearly detected at 1.3 mm with the SMA, with fluxes of 376 and 303 mJy. DG CrA, however, was not detected, down to a $3\sigma$ upper limit of only 6.6 mJy. VV CrA and S CrA were also easily detected with the ATCA at 3 and 7 mm. Using uniform weighting to image the binary VV CrA at 3 mm, it was possible to identify the two members. The binary remained unresolved at 1.3 and at 6.8 mm.

Of the 13 sources in the Serpens star-forming region that were observed with the CARMA, only three were detected. This can in part be explained by the

Table 4.4: Fluxes from point-source fits in the $(u, v)$ plane obtained with the SMA and ATCA at 1.3, 3.2, and 6.8 mm and single-dish 1.20-1.27 mm SEST fluxes. $3\sigma$ upper limits are quoted in the case of non-detections.

| Source | 1.3 mm[a] | | 3.2 mm[b] | | 6.8 mm | | SEST 1.20-1.27 mm[c] | |
|---|---|---|---|---|---|---|---|---|
| | Flux (mJy) | rms (mJy/bm) | Flux (mJy) | rms (mJy/bm) | Flux (mJy) | rms (mJy/beam) | Flux (mJy) | rms (mJy) |
| EX Lup | 19 | 3.9 | — | — | — | — | — | — |
| RY Lup | 78 | 4.9 | 2.8 | 0.7 | < 0.6[d] | 0.21 | — | — |
| Sz 91 | < 13[d] | 4.3 | — | — | — | — | < 27[d] | 9 |
| Sz 96 | < 13[d] | 4.2 | — | — | — | — | < 45[d] | 15 |
| Sz 111 | 49 | 4.8 | 5.7 | 0.7 | < 0.6[d] | 0.19 | — | — |
| SSTc2d J161029.6-392215 | < 13[d] | 4.4 | — | — | — | — | — | — |
| SSTc2d J161159.8-382338 | < 13[d] | 4.2 | — | — | — | — | — | — |
| RX J1615.3-3255 | 132 | 3.9 | 6.7 | 0.6 | < 0.5[d] | 0.17 | — | — |
| MY Lup | — | — | 8.7 | 0.4 | < 0.6[d] | 0.20 | — | — |
| Sz 65 & Sz 66 | — | — | 3.4 & 2.2 | 0.4 | — | — | 56 & 47 | 10 & 12 |
| IM Lup | 188 | 4.3 | 8.9 | 1.3 | 2.2 | 0.16 | 260 | 9 |
| HBC 556 | — | — | < 3.7[d] | 1.2 | < 0.7[d] | 0.22 | — | — |
| HBC 557 | — | — | < 3.2[d] | 1.1 | < 0.6[d] | 0.18 | — | — |
| HBC 559 | — | — | < 2.9[d] | 1.0 | < 0.3[d] | 0.09 | — | — |
| SZ Cha | — | — | 2.3 | 0.4 | — | — | 77.5 | 20.3 |
| Sz 32 | — | — | < 2.9[d] | 1.0 | 0.77 | 0.14 | 93.1 | 20.8 |
| VV CrA | 376 | 4.5 | 26.8 | 1.1 | 8.3 | 0.25 | 469, *584* | 21 |
| S CrA | 303 | 3.2 | 24.9 | 1.0 | 3.7 | 0.20 | *290* | — |
| DG CrA | < 6.6 | 2.2 | < 2.5[d] | 0.8 | < 0.5[d] | 0.16 | — | — |

[a] 1 mm band observations were at 1.33 mm (Lupus) and at 1.35 mm (Corona Australis).

[b] 3 mm band observations were at 3.17 mm.

[c] SEST fluxes are from Nürnberger et al. (1997, Lupus), Henning et al. (1993, Chamaeleon), and Henning et al. (1994, Corona Australis), with an adopted centre frequency of 236 GHz (1.27 mm). The values in italic are from Chini et al. (2003), with an adopted centre frequency of 250 GHz (1.20 mm).

[d] Quoted value is $3\sigma$ upper limit.

Table 4.5: Fluxes from point-source fits in the $(u, v)$ plane obtained with CARMA at 1.3 and 3.2 mm. No sources were detected at 6.8 mm with the VLA; $3\sigma$ upper limits are quoted.

| Source | 1.3 mm[a] | | 3.2 mm[b] | | 6.8 mm | |
|---|---|---|---|---|---|---|
| | Flux (mJy) | rms (mJy/bm) | Flux (mJy) | rms (mJy/bm) | Flux (mJy) | rms (mJy/beam) |
| EC 82 | < 15.7[c] | 5.2 | < 2.9[c] | 1.0 | < 0.5[c] | 0.2 |
| EC 90 | 95.7 | 10.4 | 11.5 | 1.2 | < 1.0[c] | 0.3 |
| EC 97 | < 23.3[c] | 7.8 | — | — | < 0.6[c] | 0.2 |
| SSTc2d J18290088+0029315 | 26.4 | 4.9 | 3.4 | 0.5 | < 0.7[c] | 0.2 |
| IRAS 18268-0025 | < 15.6[c] | 5.2 | < 1.9[c] | 0.6 | — | — |
| CoKu Ser-G3 | < 17.1[c] | 5.7 | < 1.8[c] | 0.6 | < 1.2[c] | 0.4 |
| SSTc2d J18285808+0017244 | < 24.6[c] | 8.2 | < 1.9[c] | 0.6 | — | — |
| VV Ser | < 14.8[c] | 4.9 | < 1.8[c] | 0.6 | < 0.7[c] | 0.2 |
| SSTc2d J18285020+0009497 | < 22.8[c] | 7.6 | < 1.9[c] | 0.6 | < 0.6[c] | 0.2 |
| SSTc2d J18294410+0033561 | < 15.0[c] | 5.0 | < 1.7[c] | 0.6 | — | — |
| SSTc2d J18293619+0042167 | < 8.7[c] | 2.9 | < 2.9[c] | 1.0 | — | — |
| GSC 00446-00153 | 90.8 | 3.5 | 6.8 | 1.0 | — | — |
| SSTc2d J18280503+0006591 | < 8.7[c] | 2.9 | < 2.9[c] | 1.0 | — | — |

[a] 1 mm band observations were at 1.33 mm.

[b] 3 mm band observations were at 3.15 mm.

[c] Quoted value is $3\sigma$ upper limit.

weakness of the other sources, of which six were new Spitzer sources. None of the sources were detected at 6.8 mm using the VLA.

Four cold discs were observed at 1.3 and 3.2 mm for this work. Only one of those, Sz 111, was detected. Unfortunately, Sz 111 was not observed with the Spitzer IRS.

All four binaries that were observed at 1.3 and 3.2 mm were detected at both wavelengths. EC 90 and S CrA remained unresolved. The binary Sz 65+Sz 66 was resolved with the ATCA at 3.2 mm. VV CrA could be resolved with the ATCA at 3.2 mm if the source was imaged using uniform weighting (optimised for resolution). However, this binary remained unresolved with the SMA at 1.3 mm and with the ATCA at 6.8 mm.

The detection rate at mm wavelengths of the sources observed in this study is rather low. This can in part be understood by the distance to the star-forming regions, with the Serpens star-forming region being almost twice as far away as the Taurus-Auriga star-forming region and the Gum nebula in Vela almost three times as far away. This reduces the observed flux for similar sources by a factor of about four to nine. The low detection rate for Lupus is largely a selection effect: most of the brightest sources had been observed before (Chapter 3). These previously detected sources will be included in the analysis below.

Disc masses were obtained from the fluxes at 3.2 mm under the rather crude assumptions of an isothermal disc and a fixed opacity. Under these assumptions, the mass of an optically thin disc is given by $M_{\rm disc} = F_\nu \Psi D^2 / \kappa_\nu B_\nu(T_{\rm dust})$, where $\Psi$ is the gas-to-dust ratio (taken to be 100), $D$ is the distance to the source, $\kappa_\nu$ the dust opacity (taken to be 0.9 cm$^2$ g$^{-1}$), and $B_\nu(T_{\rm dust})$ the brightness at the frequency $\nu$ for a dust temperature $T_{\rm dust}$, as given by the Planck function. We assumed a dust temperature $T_{\rm dust}$ = 25 K and found disc masses ranging from ~0.004 to ~0.07 $M_\odot$. The disc masses are presented in Table 4.6.

### 4.3.2 Millimetre slopes

The fluxes at 1, 3, and 7 mm can be combined to obtain the spectral index $\alpha$, where $F_\nu \propto \nu^\alpha$. We are interested in the emission coming from the dusty disc. However, at 7 mm, other emission mechanisms may contribute significantly to the flux. Sources may include an ionised wind or chromospheric magnetic activity. Rodmann et al. (2006) compare their fluxes at 7 mm to those at 3 and 6 cm and claim that about 20% of the emission at 7 mm is due to free-free emission. On the other hand, in Chapter 5 we show that the emission at 7 mm can be entirely attributed to dust emission for a small sample of three sources. It is possible that the emission due to, e.g., an ionised wind, is quite independent of the disc

mass and thus the relative contribution from such a wind will be larger for young stellar objects that are weaker at mm wavelengths. This could explain the findings presented in Chapter 5, in which some of the strongest pre-main-sequence mm emitters in the southern sky are monitored. However, a larger and more sensitive survey at mm to cm wavelengths is required before more quantitative statements on this subject can be made. Since we do not have fluxes at all three wavelengths for most sources, separate indices will be obtained between 1 and 3 mm ($\alpha_{1-3}$) and between 3 and 7 mm ($\alpha_{3-7}$). The results are given in Table 4.6.

The slopes between 1 and 3 mm lie between 2.38 ± 0.36 and 3.83 ± 0.46. Recalling that $\beta \approx 1.2 \times (\alpha - 2.0)$ this corresponds to opacity indices $\beta$ of about 0.5 to 2.2. The Kolmogorov-Smirnov test gives a probability of 50% that the values from this sample and that of Chapter 3 are drawn from the same distribution. This rather low value is due to the steep slopes for the sources RY Lup (3.83 ± 0.46) and SZ Cha (3.78 ± 0.43). Note that the corresponding values for $\beta$ are $\gtrsim 2$, whereas the value for the interstellar medium is $\beta_{\rm ISM} \approx 1.7$ (Draine 2006). It is therefore quite likely that other emission mechanisms are contributing at the shorter wavelength and/or that the emission at mm wavelengths is not optically thin for these two sources.

### 4.3.3 Results from Spitzer infrared observations

The spectra of the T-Tauri stars observed for Spitzer project P20611, including sources in Lupus, Vela, and Corona Australis, are published for the first time here and shown in Fig. 4.1. The 10-$\mu$m silicate features were analysed in the ways of both Furlan et al. (2006) and Kessler-Silacci et al. (2006). Furlan et al. (2006) fitted a third-order polynomial to the continuum around the 10-$\mu$m feature and determined the integrated flux above and below the continuum. The strength of the 10-$\mu$m feature was then defined as the ratio of the integrated flux due to the feature divided by the integrated flux due to the continuum, $(F_{10} - F_{\rm cont})/F_{\rm cont}$, resulting in a strength larger than 0 for a feature in emission. Kessler-Silacci et al. (2006) determined the continuum in three different ways, depending on the full mid-infrared SED and which data were available for each source, and subsequently determined the normalised spectra $S_\nu$ according to

$$S_\nu = 1 + \frac{(F_\nu - F_{\nu,c})}{< F_{\nu,c} >}, \tag{4.1}$$

where $F_\nu$ is the observed spectrum, $F_{\nu,c}$ is the fitted continuum, and $< F_{\nu,c} >$ is the frequency-averaged continuum flux (see their paper for details). They defined the strength of the 10-$\mu$m feature as the maximum value of $S_\nu$ between 5 and 13 $\mu$m,

Table 4.6: Mm slopes, disc masses, and properties of the 10-$\mu$m silicate feature.

| Source | $\alpha_{1-3}$ | $\alpha_{3-7}$ | $M_{disc}$[a] ($M_\odot$) | $\frac{F_{10}-F_{cont}}{F_{cont}}$ | $F_{peak}^{10\mu m}$ | $\frac{F_{11.3}}{F_{9.8}}$ |
|---|---|---|---|---|---|---|
| EX Lup | ... | ... | ... | 0.54 | 2.01 | 0.73 |
| RY Lup | 3.8 ± 0.5 | > 2.0 | 0.005 | 1.10 | 3.16 | 0.66 |
| Sz 96 | ... | ... | ... | 0.78 | 2.30 | 0.82 |
| Sz 111 | 2.5 ± 0.4 | > 2.9 | 0.011 | ... | ... | ... |
| J161159.8-382338 | ... | ... | ... | 0.92 | 2.48 | 0.84 |
| RX J1615.3-3255 | 3.4 ± 0.5 | > 3.4 | 0.013 | 1.25 | 3.04 | 0.96 |
| MY Lup | ... | > 3.5 | 0.017 | 0.54 | 1.87 | 0.79 |
| Sz 65 | 3.0 ± 0.4 | ... | 0.007 | 0.36 | 1.51 | 0.93 |
| Sz 66 | 3.3 ± 0.4 | ... | 0.004 | 0.40 | 1.62 | 0.92 |
| Sz 74 | ... | ... | ... | 0.18 | 1.29 | 1.03 |
| Sz 77 | ... | ... | ... | 0.43 | 1.63 | 0.94 |
| IM Lup | 3.6 ± 0.4 | 1.8 ± 0.3 | 0.017 | 0.52 | 1.81 | 0.85 |
| HBC 553 | ... | ... | ... | 0.22 | 1.43 | 0.86 |
| HBC 556 | ... | ... | < 0.051 | 0.40 | 1.64 | 0.99 |
| HBC 557 | ... | ... | < 0.044 | 0.21 | 1.37 | 0.95 |
| HBC 559 | ... | ... | < 0.040 | 0.39 | 1.60 | 0.85 |
| HBC 560 | ... | ... | ... | 0.29 | 1.44 | 1.03 |
| HBC 561 | ... | ... | ... | 0.43 | 1.67 | 0.90 |
| SZ Cha | 3.8 ± 0.4 | ... | 0.006 | 0.71 | 2.30 | 0.85 |
| Sz 32 | > 3.7 | < 1.8 | < 0.008 | 0.14 | 1.24 | 1.11 |
| VV CrA | 2.5 ± 0.5 | 2.4 ± 0.5 | 0.039 | ... | ... | ... |
| S CrA | 2.9 ± 0.7 | 2.5 ± 0.4 | 0.036 | 0.34 | 1.51 | 0.97 |
| DG CrA | ... | ... | < 0.004 | 1.04 | 2.94 | 0.67 |
| EC 82 | ... | ... | < 0.017 | 1.41 | 3.55 | 0.67 |
| EC 90 | 2.5 ± 0.5 | ... | 0.067 | 0.26 | 1.40 | 1.12 |
| EC 97 | ... | ... | ... | 0.34 | 1.56 | 0.90 |
| J18290088+0029315 | 2.4 ± 0.4 | ... | 0.020 | 0.15 | 1.27 | 0.96 |
| CoKu Ser-G3 | ... | ... | < 0.010 | -0.09 | 0.82 | 1.17 |
| VV Ser | ... | ... | < 0.010 | 0.33 | 1.45 | 0.97 |
| J18285020+0009497 | ... | ... | < 0.011 | 0.36 | 1.57 | 0.88 |
| GSC 00446-00153 | 3.0 ± 0.5 | ... | 0.040 | ... | ... | ... |

[a] Disc masses estimated from ATCA and CARMA fluxes, assuming a gas-to-dust ratio $\Psi = 100$, a dust opacity $\kappa_\nu = 0.9$ cm$^2$ g$^{-1}$, and a dust temperature $T_{dust} = 25$ K.

$S_{peak}^{10\mu m}$, resulting in a value larger than 1 for a feature in emission. Furthermore, Kessler-Silacci et al. (2006) defined the shape of the 10-$\mu$m feature as the ratio $S_{11.3}/S_{9.8}$.

For this work, the continuum was consistently chosen for all sources by fitting a third-order polynomial to data between 5.0 and 7.5 $\mu$m and between 13.0 and 16.0 $\mu$m (cf. Furlan et al. 2006). The regular continuum was used rather than the frequency-averaged continuum, resulting in the peak strength $F_{peak}^{10\mu m}$ and the shape $F_{11.3}/F_{9.8}$. This does not change the results significantly (see Kessler-Silacci et al. 2006).

The results are listed in Table 4.6 and shown in Fig. 4.2. The upper panel of Fig. 4.2 gives $(F_{10} - F_{\rm cont})/F_{\rm cont}$ vs $F_{peak}^{10\mu m}$, showing a clear correlation between the two definitions of the strength of the 10-$\mu$m feature. The lower panel gives $F_{peak}^{10\mu m}$ vs $F_{11.3}/F_{9.8}$, also showing a correlation, confirming the results of Kessler-Silacci et al. (2006). It follows that the three methods to quantify the strength or shape of the 10-$\mu$m feature give completely consistent results. When comparing the 10-$\mu$m feature with the mm slope in Sect. 4.5 below, the strength defined as $(F_{10} - F_{\rm cont})/F_{\rm cont}$ will be used. The source that lies towards the top and to the right of the general trend in the lower panel is RX J1615.3-3255, an isolated source slightly to the north of the Lupus star-forming clouds.

### 4.3.4 10-$\mu$m feature vs mm slope

Figs. 4.3 and 4.4 show the mm slope $\alpha$, measured between 1 and 3 mm, as a function of the strength of the 10-$\mu$m feature $(F_{10} - F_{\rm cont})/F_{\rm cont}$. Included are the sources from this study, as well as those located in the Taurus-Auriga star-forming region discussed in Rodmann et al. (2006) and Andrews & Williams (2007), and those located in Lupus and Chamaeleon and discussed in Chapter 3. In Fig. 4.4, the sources are sorted by their star-forming region.

The mm slope and the strength of the 10-$\mu$m feature correlate weakly for the sample shown in Fig. 4.3: the Spearman rank correlation coefficient is 0.50, with a 99.5% confidence level. However, if the point in the lower right (RY Tau) is excluded, the Spearman rank correlation coefficient becomes 0.66, with a 99.99% confidence level.

Fig. 4.4 suggests a grouping in the $\mu$m-vs-mm diagram according to parental cloud, with the sources from the Taurus-Auriga star-forming region more concentrated in the lower left, the Lupus sources more to the upper left, and the Chamaeleon sources more to the centre right. Note that the six Lupus sources that are on the left part of the diagram (from top to bottom: IM Lup, Sz 66, Sz 65, RU Lup, GW Lup, and HT Lup) are all located in the Lupus 1 and Lupus 2 clouds,

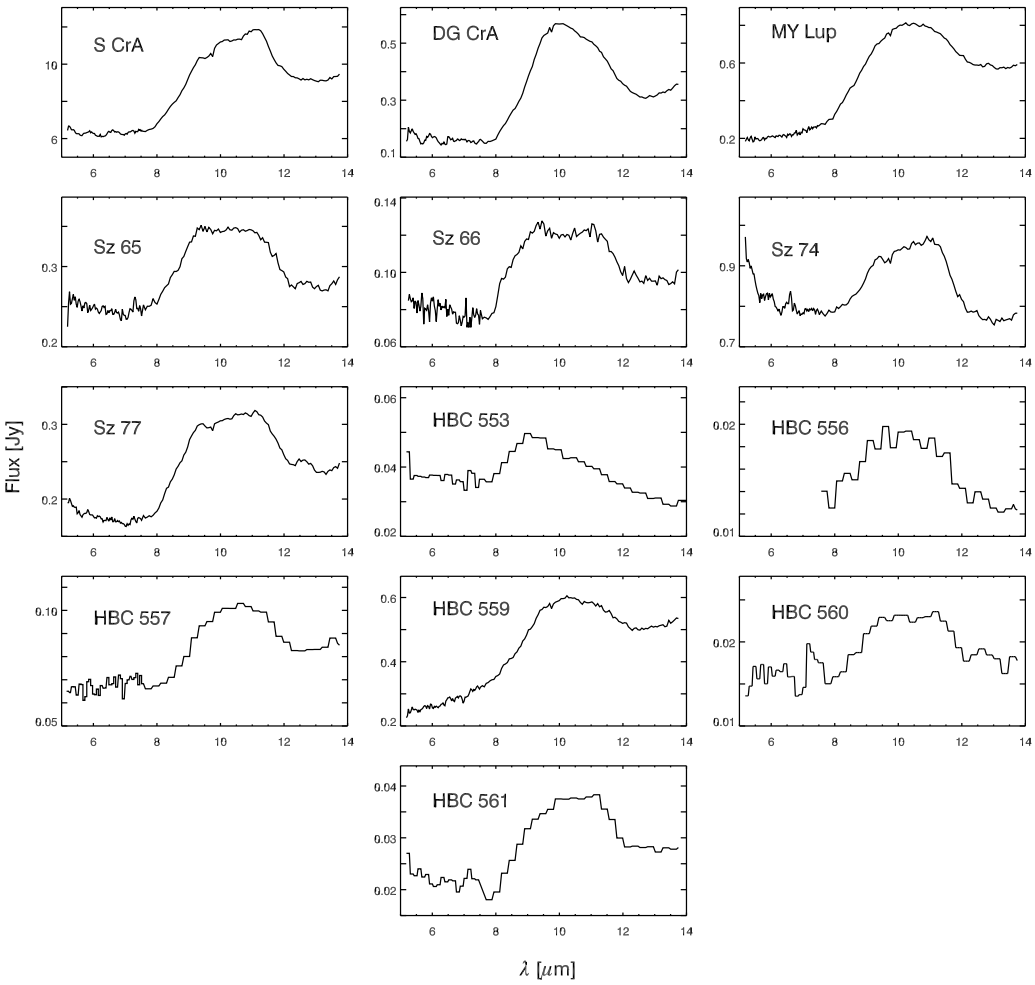


Figure 4.1: Spitzer IRS spectra from the T-Tauri stars observed for Spitzer project P20611 (C.M. Wright PI). Spectra with a maximum flux below 0.1 Jy were binned four times to improve the signal-to-noise ratio.

whereas the remaining two Lupus sources are located in Lupus 3 (top-most source, RY Lup) and off-cloud (RX J1615.3-3255). One explanation for this is that these star-forming regions each represent a different evolutionary phase and/or that each region has a different mechanism dominating the evolution. Another explanation

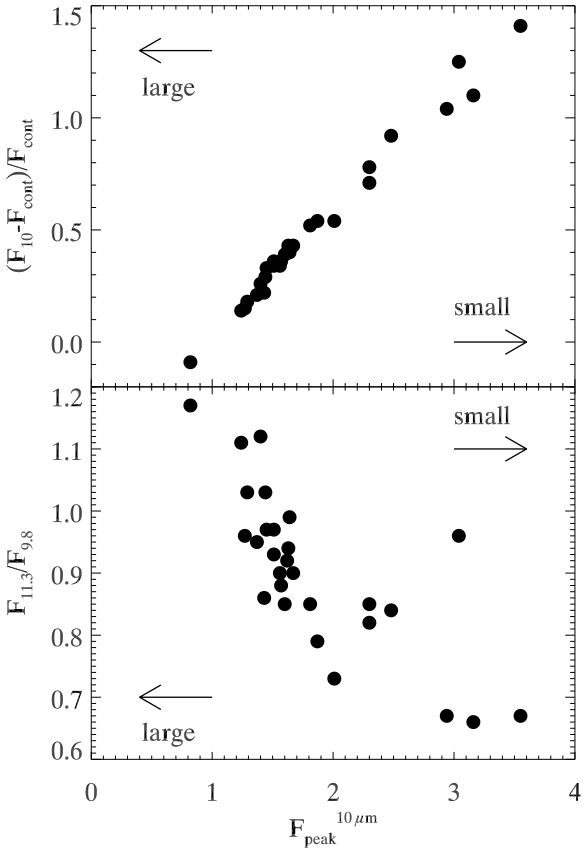


Figure 4.2: *Upper panel*: peak strength of the 10-$\mu$m feature as defined in Kessler-Silacci et al. (2006) vs the strength as defined in Furlan et al. (2006). *Lower panel*: peak strength of the 10-$\mu$m feature vs the shape as in Kessler-Silacci et al. (2006). Included are the sources observed in this work for which the 10-$\mu$m feature could be obtained. The object towards the top and the right off the general trend in the lower panel is the isolated source RX J1615.3-3255.

could be that the different regions have a different mineralogy, e.g., a lower silicate content in the Taurus-Auriga star-forming region than in Chamaeleon, resulting in a weaker 10-$\mu$m feature.

Kessler-Silacci et al. (2006) found a correlation between the spectral type of a source and the strength and shape of the 10-$\mu$m silicate feature, with brown

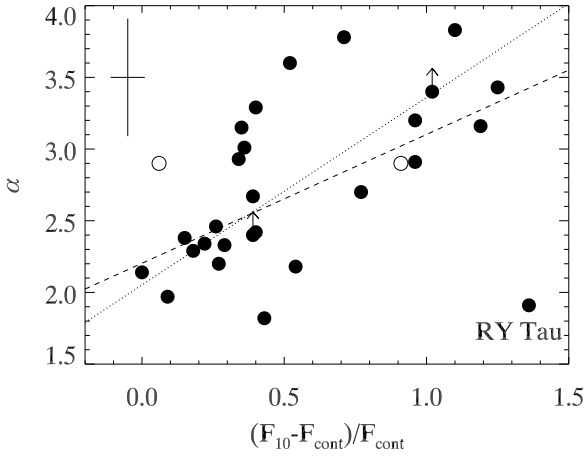


Figure 4.3: The mm slope as measured between 1 and 3 mm as a function of the strength of the 10-$\mu$m feature. The open symbol on the left is for T Cha, which does not show any silicate emission and is not used in the analysis; the strength of the 10-$\mu$m feature slightly larger than zero is due to PAH emission. The open symbol in the centre is for the circumbinary disc CS Cha. The dashed line shows a linear fit to all the data. The dotted line shows a linear fit to the data with RY Lup (the point in the lower right corner) excluded. Included are the sources studied in this Chapter, as well as those from Rodmann et al. (2006), Andrews & Williams (2007), and Chapter 3. Typical uncertainties are included in the upper left corner.

dwarfs having predominantly flatter and Herbig-Ae/Be stars having more peaked features. It was found that this is most likely due to the location of the silicate emission region (Kessler-Silacci et al. 2007). Kessler-Silacci et al. (2007) found that the radius of the 10-$\mu$m silicate emission zone in the disc goes roughly as $(L_*/L_\odot)^{0.56}$. Hence, the 10-$\mu$m feature probes a radius further from the star for early-type stars than for late-type stars. In this context it is interesting to see whether a correlation with spectral type is found in the 10-$\mu$m-feature vs mm-slope diagram (see Fig. 4.5). The M stars in the sample presented here are concentrated to the left, the F and G stars to the lower left, and the M stars are found more to the centre. Hence, no clear correlation with spectral type is found here. It is interesting to note, though, that the F and G sources RY Tau and RY Lup show up isolated from the other F and G sources. This may indicate that these sources are indeed different from the other sources in the sample, justifying the choice not

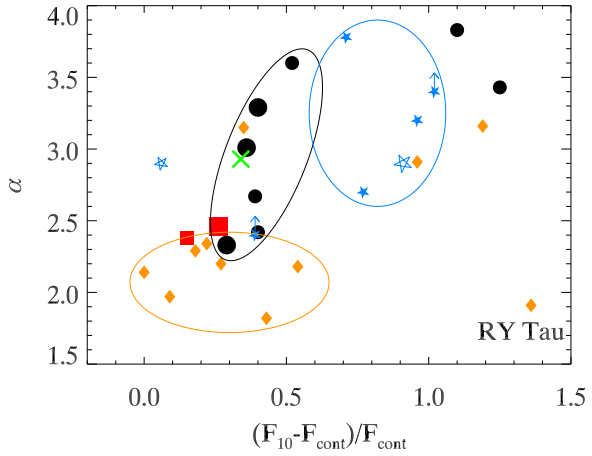


Figure 4.4: Same as Fig. 4.3, with the different sources sorted by star-forming region: *circles*: Lupus, *five-pointed stars*: Chamaeleon, *cross*: Corona Australis, *diamonds*: Taurus-Auriga, and *squares*: Serpens. The ellipses show the concentrations of sources located in the Taurus-Auriga star-forming region (lower left), the Chamaeleon I cloud (top centre), and the Lupus 1 and Lupus 2 clouds (upper left). The remaining two Lupus sources in the upper right are an isolated source (RX J1615-.3-3255, right-most dot) and a source from the Lupus 3 cloud (RY Lup, upper-most dot). The small symbols designate the single stars and the large symbols designate multiple systems. The open five-pointed star to the left is for T Cha, an evolved cold disc which shows no silicate emission around 10 $\mu$m. The open five-pointed star in the centre is CS Cha, a circumbinary disc.

to include RY Tau in the analysis.

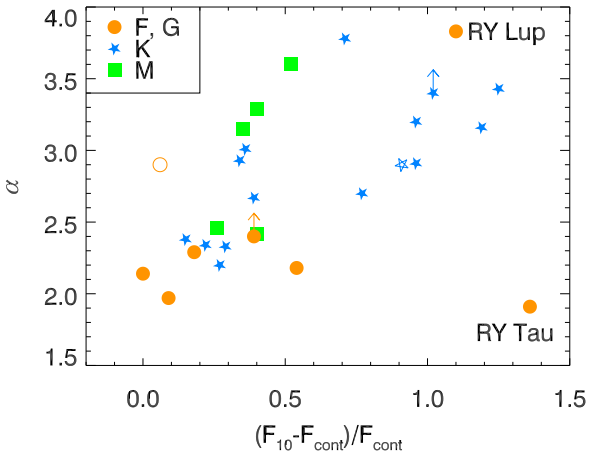


Figure 4.5: Same as Fig. 4.3, with the different sources sorted by spectral type: *circles*: F and G, *five-pointed stars*: K, and *squares*: M.

## 4.4 Modelling

### 4.4.1 Disc model parameters and SEDs

As variations in the strength and shape of the 10-$\mu$m feature (e.g., Kessler-Silacci et al. 2006) as well as in the (sub)mm slope (e.g., Beckwith et al. 1990) can be explained by variations in the sizes of the grains in the circumstellar discs, one may expect a correlation between properties of the 10-$\mu$m feature and the mm slope. We found such a correlation from the observations for the sample as a whole (see previous Section) and this may imply that grain growth occurs in the entire disc simultaneously, or that grains grow in the inner disc and the new grain size distribution is very efficiently spread to the outer disc through radial mixing. Both processes will have the effect of a shift of dust mass from small particles to larger grains. To study this more quantitatively, we ran a number of models with varying grain size distributions.

We use the three-dimensional axisymmetric radiative-transfer code developed by Dullemond (2002) and Dullemond & Dominik (2004a). The disc model is based on the classic model by Chiang & Goldreich (1997), adapted to include a hot inner wall, which is directly irradiated by the central star (Natta et al. 2001, see also Dullemond et al. 2001). The surface density of the disc as a function of radius $\Sigma(r)$ is defined to be:

$$\Sigma(r) = \Sigma_{\rm out}\,(r/R_{\rm out})^n \tag{4.2}$$

with $n$ taken to be $n = -1$. The disc mass was fixed to $M_{\rm disc} = 5 \times 10^{-3}$ M$_\odot$. The gas-to-dust mass ratio $\Psi$ was set to 100, which implies that the total mass in dust grains is also fixed, to a value of $5 \times 10^{-5}$ M$_\odot$. The variation of the scale height, i.e., the flaring of the disc, was then set by $H(r) = rH_{\rm out}/R_{\rm out}(r/R_{\rm out})^\gamma$. For the radiation field coming from the central star, a black-body spectrum with $T_{\rm eff} = 3000$ K and $L = 1$ L$_\odot$ was used. The inner radius was fixed to $R_{\rm in} = 0.1$ AU, corresponding to a temperature of ~1800 K.

For the dust opacities, we use a mixture of 80% amorphous olivine and 20% armorphous carbon (percentages by mass). The opacities are calculated using a Distribution of Hollow Spheres (DHS, see Min et al. 2003). The total volume of the spheres occupied by the inclusion $f$ is taken in the range $f = [0, 0.8]$. It was found by Dullemond & Dominik (2004a) that the mm slope changes if one goes from a disc with only "small," 0.1-$\mu$m-sized particles to a disc that also contains some "large," 2-mm-sized grains. Dullemond & Dominik (2004a) replaced 90%, 99%, 99.9%, 99.99%, and 99.999% of the mass by large grains. However, although the mm slope changes considerably when the mass fraction in large grains

is changed from 0 to 90%, it does not change further if a larger fraction of the dust mass is put in large grains (see Fig. 7 in Dullemond & Dominik 2004a). Although it is possible that a more gradual change in the mm slope is seen when smaller mass fractions are put in large grains, it does seem to be more important what the largest grain size is than which fraction of the dust is contained in such large grains. We therefore chose not to use a bimodal dust distribution, but a distribution in which the size of the grains ranges from a fixed minimum value $a_{\rm min}$ to a varying maximum value $a_{\rm max}$ according to

$$n(a) \propto \left(\frac{a}{a_{\rm min}}\right)^{-m}. \tag{4.3}$$

This power-law distribution is expected on theoretical grounds whenever grain-grain collisions lead to shattering (Dohnanyi 1969). It should be noted that models which include grain growth may lead to different grain size distributions (e.g., Dullemond & Dominik 2005; Tanaka et al. 2005). The value $a_{\rm min}$ was fixed to 0.003 $\mu$m and $a_{\rm max}$ was varied in steps of ten from 0.1 $\mu$m to 1.0 cm. A value of $m = 3.5$ is representative of interstellar grains (Mathis et al. 1977). A shallower slope of $m = 2.5$ is expected when grains coagulate to larger sizes (Natta et al. 2004, 2007), whereas a slope of $m = 4.0$ is expected when also fragmentation is taken into account (e.g., Dominik & Dullemond 2008). Models run with $m = 4.0$ gave practically no variation of the mm slope, which is an interesting result in itself. It may indicate that the $a_{\rm min}$ is not so small in protoplanetary discs, that the dust size distribution is rather bimodal (or even trimodal) than a power law, or that the grain size distribution is not as steep as models predict. A power-law slope $m = 3.5$ was used for the detailed analysis below. The different model parameters are summarised in Table 4.7.

The resulting SEDs from six models, with $a_{\rm max}$ varying and the other parameters kept fixed, is shown in Fig. 4.6. In these models, $R_{\rm out}$ was fixed to 300 AU, $H_{\rm out}$ to 90 AU, and the flaring angle to $\gamma = 0.14$. Strong variations are seen in all wavelength regimes, from the near-infrared through the mm. At wavelengths $\lambda \lesssim 2$ $\mu$m, grain size distributions without grains larger than 1 $\mu$m give such a high opacity that the central star is significantly reddened. In the mid- and far infrared, the flux drops with increasing maximum grain size. The (sub)mm part of the SED does not change appreciably unless grains with sizes of $\sim$100 $\mu$m or larger are included. After that, the (sub)mm slope becomes shallower quite rapidly with increasing $a_{\rm max}$. This figure also demonstrates that care must be taken when estimating the disc mass from the (sub)mm emission alone: even when the dust species is kept the same, assuming a different grain size distribution may already

Table 4.7: Model parameters.

| Parameter | standard value | range |
|---|---|---|
| Mass $M_{\rm star}$ | 1.0 $M_\odot$ | |
| $T_{\rm eff}$ | 3000 K | |
| Luminosity $L_{\rm star}$ | 1.0 $L_\odot$ | |
| Radius $R_{\rm star}$ | 5.1 $R_\odot$ | |
| Mass $M_{\rm disc}$ ($M_\odot$) | $5 \times 10^{-3}$ | |
| Disc inclination angle $i$ (°) | 45 | 5.7, 15, 30, 45, 60, 75, 89 |
| Surface mass density gradient $n$ | –1.0 | |
| Gas-to-dust ratio | 100 | |
| Inner radius $R_{\rm in}$ (AU) | 0.1 | |
| Outer radius $R_{\rm out}$ (AU) | 300 | 100, 200, 300 |
| Disc thickness $H_{\rm out}/R_{\rm out}$ | 0.3 | 0.2, 0.3, 0.4 |
| Flaring angle $\gamma$ | 0.14 | 0.07, 0.14, 0.21 |

change the opacity at 1 mm by an order of magnitude, which will give an equally large uncertainty in the mass estimate from an observed flux at that wavelength.

### 4.4.2 10-$\mu$m feature vs mm slope

To quantify the evolution of the spectral energy distribution as a function of disc and dust properties, we plot the strength of the 10-$\mu$m feature vs the mm slope for different models. The strength of the 10-$\mu$m feature $(F_{10} - F_{\rm cont})/F_{\rm cont}$ is defined as in Furlan et al. (2006) and the mm slope $\alpha$ was determined between 1.0 and 3.0 mm. The results are shown in Fig. 4.7. A possible evolutionary path, from small to large grains, is indicated in each panel with arrows.

In the upper left panel, the maximum grain size is varied from $a_{\rm max} = 0.1$ $\mu$m to 1, 10, and 100 $\mu$m, and finally 1 mm and 1 cm. When $a_{\rm max}$ is changed from 0.1 $\mu$m to 10 $\mu$m, the strength of the 10-$\mu$m silicate feature decreases slightly while the mm slope $\alpha$ is unaffected. When more and more mass is shifted into grains of sizes of 100 $\mu$m and larger, the mm slope $\alpha$ becomes shallower, whereas the 10-$\mu$m feature is further unaffected.

In the top right panel, the results for models with varying physical disc thickness are shown, with $H_{\rm out} = 60$, 90, and 120 AU for a fixed outer radius $R_{\rm out} = 300$ AU. This was done for grain size distributions consisting of only very small grains ($a_{\rm max} = 0.1$ $\mu$m), with grains up to 100 $\mu$m and for distributions including

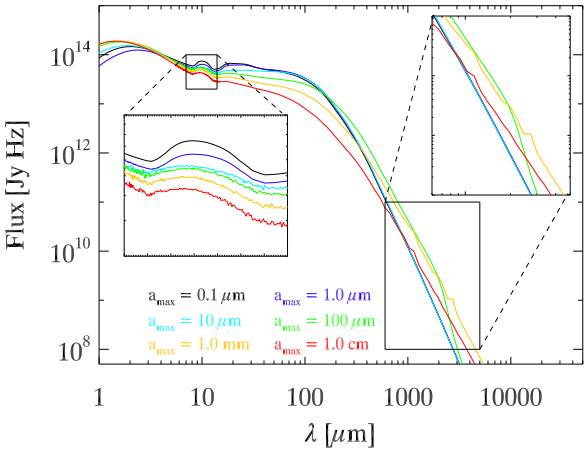


Figure 4.6: Spectral energy distributions (SEDs) for models of a $5 \times 10^{-3}$ $M_\odot$ disc with a varying grain size distribution, seen under an inclination $i = 45°$. The minimum grain size is 0.003 $\mu$m for all models and the maximum grain size varies from 0.1 $\mu$m (black curve) to 1.0 cm in steps of ten (lighter curves). The insets show blow-ups from the 10-$\mu$m feature and the mm part of the SEDs. Note that the SEDs for $a_{max} = 0.1$ $\mu$m, 1.0 $\mu$m, and 10 $\mu$m are completely overlapping in the mm part.

large grains ($a_{max} = 1$ cm). The thickness of the disc mainly affects the 10-$\mu$m feature, largely caused by the fact that the outer disc gets partly in the line of sight between the feature and the observer. In fact, for fairly thick discs with $H/R = 0.4$, the 10-$\mu$m feature appears in absorption for grain size distributions with a maximum grain size up to 100 $\mu$m (not shown in the plot). The shift in $\alpha$ is mainly due to the difference in $a_{max}$.

Another way to change the geometry of the disc is by varying the flaring angle $\gamma$, as is demonstrated in the middle left panel of Fig. 4.7. $R_{out}$ is fixed to 300 AU, $H_{out}$ to 60 AU, and $\gamma$ is varied between 0.07, 0.14, and 0.21, for grain size distributions with $a_{max} = 0.1$ $\mu$m, $a_{max} = 100$ $\mu$m, and $a_{max} = 1$ cm. The mm slope is hardly affected and the effect on the 10-$\mu$m silicate feature is again caused by the fact that the outer disc (partly) obscures it from the point of view of the observer. For the smallest grains, the 10-$\mu$m feature appears in absorption for $\gamma = 0.21$ (not shown).

The effect of the angle under which the system is observed is demonstrated in

the middle right panel. The inclination is varied from close to face on at 5.7° via 15, 30, and 45° up to a maximum inclination $i = 60°$, for maximum grain sizes $a_{\rm max} = 0.1\,\mu$m, $a_{\rm max} = 100\,\mu$m, and $a_{\rm max} = 1$ cm. In these models, $R_{\rm out} = 300$ AU, $H_{\rm out} = 90$, and $\gamma = 0.14$. No effect on the mm slope $\alpha$ is observed, whereas small variations are seen for the strength of the 10-$\mu$m feature. For larger inclinations (for $a_{\rm max} = 0.1\,\mu$m and $a_{\rm max} = 100\,\mu$m already for $i = 60°$, not shown), the 10-$\mu$m feature is observed through the outer disc and appears in absorption.

In the lower left panel of Fig. 4.7 the results are shown for discs with outer radii of 300 AU, 200 AU, and 100 AU. The changes in the mm slope $\alpha$ are again mainly due to the change in $a_{\rm max}$, though a trend is observed with the slope becoming steeper as the disc gets larger. The strength of the 10-$\mu$m feature is also affected, with the strongest features observed for the largest discs, and the feature actually moving into absorption for a 100-AU disc with $a_{\rm max} = 0.1\,\mu$m.

For each of the models in the lower right panel, four dust size distributions are used. The largest triangle is for a disc with a grain size distribution with $a_{\rm max} = 1$ cm throughout, while the smallest triangle is for a disc with a grain size distribution with $a_{\rm max} = 0.1\,\mu$m throughout. The other triangles represent discs with intermediate stages of grain growth and spreading of large grains, with respectively $a_{\rm max} = 1$ cm, 1 mm, 100 $\mu$m, and 10 $\mu$m inward of 0.5 AU, $a_{\rm max} =$ 100, 1.0, 0.1, and again 0.1 $\mu$m outward of 50 AU, and intermediate grain sizes between 0.5 and 50 AU. A similar effect is seen as in the upper left panel. This seems to suggest that the grain size is the dominating effect for the evolution of the 10-$\mu$m feature and the mm slope, rather than the location where the (large) grains reside.

It should be noted that our modelling results do not cover the entire parameter space found from the observations. In particular, the sources with the strongest 10-$\mu$m features are not represented by the models. This can at least in part be explained by the fact that settling is not included in the models here. Allowing the largest grains to settle to the mid-plane with the smallest grains suspended in the disc atmosphere will boost the strength of the 10-$\mu$m feature. The slope of the grain size distribution $m$ may also have an effect on the strength of the 10-$\mu$m feature.

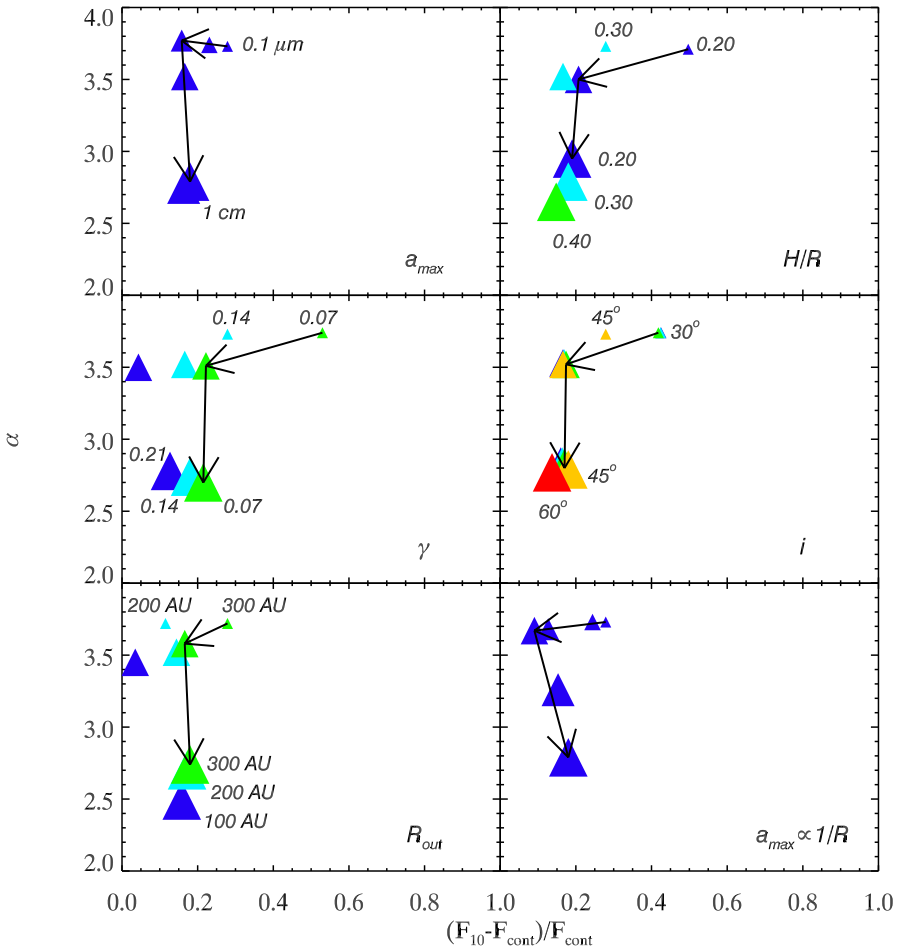


Figure 4.7: The mm slope $\alpha$ vs the strength of the 10-$\mu$m feature. See text for disc parameters. The size of the triangles indicates the size of the largest dust grains $a_{\rm max}$; the colour indicates the variation of the other parameters. The arrows indicate an increase in grain size. *Top left*: variation of maximum grain size $a_{\rm max}$ from 0.1 $\mu$m to 1, 10, and 100 $\mu$m, 1 mm, and 1 cm. *Top right*: variation of disc thickness $H/R$ from 0.20 (dark blue) via 0.30 (light blue) to 0.20 (green). *Middle left*: variation of flaring angle $\gamma$ from 0.07 (dark blue) via 0.14 (light blue) to 0.21 (green). *Middle right*: variation of inclination $i$ from close to face on (5.7°, dark blue) to 15, 30, 45, and 60° (light blue, green, yellow, and red). *Lower left*: variation of the radius $R_{\rm out}$ from 300 AU (green) via 200 AU (light blue) to 100 AU (dark blue). *Lower right*: variation of maximum grain size with radius.

## 4.5 Discussion

A correlation between the strength of the 10-$\mu$m silicate feature and the slope between 1 and 3 mm is observed in a sample of 27 T-Tauri stars. Put differently, there are no sources with a strong 10-$\mu$m feature and a shallow mm slope, nor sources with a weak 10-$\mu$m feature and a steep mm slope (with the sole exception of RY Tau). This would suggest that grain growth occurs almost simultaneously throughout the disc or, considering the fact that grain growth will mainly take place in the mid-plane of the inner disc where the densities are highest, that considerable mixing must take place. It also seems to imply that most of the submicron-sized grains are gone by the time the largest grains reach mm sizes. The modelling results do not show such a clear correlation between the strength of the 10-$\mu$m feature and the mm slope. It would rather appear that first the 10-$\mu$m feature becomes flatter and subsequently the mm slope becomes shallower. Note that this may in part be due to the steep grain size distribution and the very low value for the minimum grain size $a_{\rm min} = 0.003$ $\mu$m used in the models.

A gradual over-all change in the grain size distribution as suggested by the observations can also naturally explain the clustering of the sources per star-forming region. The T-Tauri stars in Chamaeleon show the strongest 10-$\mu$m features, as well as the steepest mm slopes. The T-Tauri stars located in the Lupus 1 and Lupus 2 clouds have somewhat weaker 10-$\mu$m features and mm slopes that are a bit shallower than the Chamaeleon sources. The sources located in the Taurus-Auriga star-forming region, finally, have the weakest 10-$\mu$m features and the shallowest mm slopes. This suggests an evolutionary sequence, with the Chamaeleon sources being the least evolved, and the Taurus-Auriga sources the most evolved, although we warn that the samples for each of these clouds are highly incomplete.

Grain size, or rather the maximum grain size, is not the only parameter that affects the observables. It is the dominating effect where the steepness of the mm slope is concerned. However, the strength of the 10-$\mu$m feature is also significantly affected by the geometry of the disc and the inclination under which the system is observed. For example, a "self-shadowed" disc, with a small flaring angle $\gamma$, gives a much stronger 10-$\mu$m feature than a "flaring" disc with a large value for $\gamma$. Note that Acke et al. (2004) found a correlation between the single-dish (sub)mm slope between 350 $\mu$m and 2.7 mm and the excess at 60 $\mu$m for their sample of 26 Herbig-Ae/Be stars, suggesting that grain growth causes a circumstellar disc to evolve from flaring to self-shadowed. However, Acke & van den Ancker (2004) do not find a correlation between the strength of the 10-$\mu$m feature and the (sub)mm slope. We also find that a physically flat disc (small value for $H/R$) gives a strong 10-$\mu$m feature, whereas a physically thick disc results in a

weak 10-$\mu$m feature. The effect is the strongest for grain size distributions that are strongly dominated by small grains, up to sizes of $\sim$10 $\mu$m. One must therefore be very careful when trying to deduce grain sizes, or indeed the physical geometry of the disc, from the strength of the 10-$\mu$m feature alone.

It should be noted that our models do not cover the whole range of observed feature strengths and mm slopes. Indeed, 10-$\mu$m strengths of $(F_{10} - F_{\rm cont})/F_{\rm cont}$ considerably larger than 1.0 are observed, whereas the values for the models hardly come up to 0.5. This may in part be due to the fact that settling is not taken into account in the models presented here. It is well known that large grains will settle to the disc mid-plane, while the smallest grains remain suspended in the disc atmosphere. We ran a number of models in which we allowed the larger grains to settle and found that the resulting spectra ended up in the upper right of the 10-$\mu$m-feature vs mm-slope diagrams. This confirms that the strength of the 10-$\mu$m feature is affected by dust settling, as was already found by Dullemond & Dominik (2008) using the same code.

In this context it is interesting to consider another possible relation between the infrared and the mm regimes. The flux around 70 $\mu$m, or more generally the mid- to far-IR slope, may be a good tracer of dust settling (e.g., Dullemond & Dominik 2004b). Under the assumption that dust settling is required to get high enough densities for significant grain growth to occur, this would imply a correlation between the slope in the mid-infrared, e.g., between 24 and 70 $\mu$m, and the mm slope. As only a small number of the sources for which we obtained reliable mm slopes were observed at several wavelengths with the Multiband Imaging Photometer for SIRTF (MIPS) on board Spitzer, we resorted to IRAS fluxes at 60 and 100 $\mu$m to look for this correlation. The results are shown in Fig. 4.8. The top panel shows the IRAS 60-$\mu$m fluxes divided by the IRAS 12-$\mu$m fluxes vs the mm slope $\alpha$ and the bottom panel shows the IRAS 100-$\mu$m fluxes divided by the IRAS 12-$\mu$m fluxes vs $\alpha$. A trend is seen, in particular in the upper panel, for sources with a relatively weak 60-$\mu$m flux to have a shallow mm slope. This can be understood as follows. Sources with a weak 60-$\mu$m flux are those sources for which the grains of several microns in size have settled to the mid-plane. Thus, in these sources, a large reservoir of micron-sized particles exist in the mid-plane. These particles will collide and grow to mm sizes, in turn causing the mm slope to become shallower.

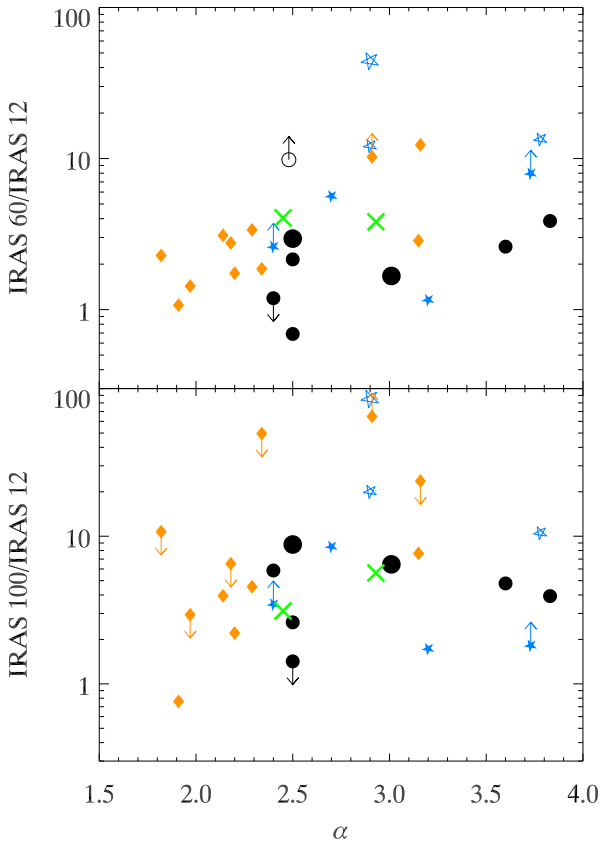


Figure 4.8: *Upper panel*: IRAS flux at 60 $\mu$m divided by the flux at 12 $\mu$m vs the mm slope $\alpha$. *Lower panel*: IRAS flux at 100 $\mu$m divided by the flux at 12 $\mu$m vs the mm slope $\alpha$. The colour coding of the sources is the same as in Fig. 4.4.

## 4.6 Conclusions

We observed 38 T-Tauri stars at infrared and mm wavelengths. Combining our new observations with data from the literature, a correlation between the strength of the 10-$\mu$m feature and the mm slope was found for the sample as a whole. Modelling protoplanetary discs with varying geometries and grain size distributions indicates that the variations in the 10-$\mu$m feature strength and mm slope can be explained by variations in grain size, but that varying disc geometries result in a large spread. While comparing the mm slopes with normalised IRAS fluxes we furthermore found that these show a positive correlation, indicating that the far-infrared slope is already a good tracer of grain growth. This can be understood if one realises that the far infrared traces the amount of settling in a disc and that the sources with the most settling will also be the sources with the most growth and consequently the largest grains.

**Acknowledgements**
We are indebted to Kees Dullemond for the use of his RADMC and RAYTRACE codes and to Stephen Bourke for help with AIPS. A special thanks to the ATNF and SMA staff for assistance with the observations. Ruud Visser's help on all things computer is greatly appreciated! Partial support for this work was provided by a Netherlands Research School For Astronomy network 2 grant, and by a Netherlands Organisation for Scientific Research Spinoza grant. C.M.W. anknowledges financial support from an ARC Australian Research Fellowship. This research has made use of the SIMBAD database, operated at CDS, Strasbourg, France.

## 4.7 Appendix: observations

A total of 20 sources (17 in Lupus and three in Corona Australis) were observed at about 1 mm with the Submillimeter Array (SMA). A full log of the SMA observations is given in Table 4.8.

With the Australia Telescope Compact Array (ATCA), 15 sources spread over the constellations Lupus, Vela, Corona Australis, and Chamaeleon were observed at 3 and 7 mm. A log of the ATCA observations is given in Table 4.9.

The Combined Array for Research in Millimeter-wave Astronomy (CARMA) was used to observe ten sources in Serpens at 1 and 3 mm. The log of these observations is presented in Table 4.10.

Finally, eight sources in Serpens were observed with the (Very Large Array) VLA at 0.7, 1.3, 3.6, and 6 cm. A full log of those observations is given in Table 4.11.

Table 4.8: Overview of the SMA observations.

| Obs. date | $\lambda\lambda$ (mm) | Config. | Target sources[a] | Gain calibrator(s) | Flux cal. | Notes |
|---|---|---|---|---|---|---|
| 20080314[b] | 1.30, 1.36 | compact | HM Lup, MY Lup, Sz 102, Sz 65 & Sz 66 Sz 73, Sz 74 Sz 76, Sz 77 | 1517-243, 1626-298 | Callisto | PWV < 2.5 mm, bad phases |
| 20080419 | 1.30, 1.36 | compact | EX Lup, RX J1615.3-3255 RY Lup, 161029.6-392215 161159.9-382337, Sz 111 Sz 91, Sz 96 | 1517-243, 1626-298 | Mars | PWV < 4.0 mm |
| 20081001 | 1.31, 1.37 | compact | VV CrA, S CrA, DG CrA | 1924-292 | Callisto | PWV < 2.5 mm |

[a] In the case of SSTc2d names, only the coordinates (in J2000) are shown.

[b] Phase instabilities rendered these observations unusable.

Table 4.9: Overview of the ATCA observations.

| Obs. date | $\lambda\lambda$ (mm) | Config. | Target sources | Gain calibrator(s) | Flux cal. | Notes |
|---|---|---|---|---|---|---|
| 20080712 | 3.14, 3.21 | H214 | HBC 556, HBC 557, HBC 559 | 0745-330 | Mars | Mostly nice weather |
| 20080713 | 6.67, 6.99 | H214 | HBC 556, HBC 557, HBC 559 | 0826-373 | Uranus | Weather worsening |
| 20080728 | 6.67, 6.99 | H214 | HBC 559 | 0826-373 | Uranus | Mostly nice weather |
| 20080729 | 3.14, 3.21 | H214 | HBC 559 | 0745-330 | Uranus | Mostly nice weather |
| | | | SZ Cha, Sz 32 | 1057-797 | | |
| 20080730 | 3.14, 3.21 | H214 | SZ Cha | 1057-797 | Uranus | Weather less than perfect |
| 20080801 | 6.67, 6.99 | H214 | Sz 111, RY Lup | 1600-44 | Uranus | Weather improving |
| | | | RX J1615.3-3255 | 1622-297 | | |
| | | | VV CrA, S CrA, DG CrA | 1921-293 | | |
| 20080802 | 3.14, 3.21 | H214 | SZ Cha | 1057-797 | Uranus | Weather improving |
| | | | Sz 111, RY Lup | 1600-44 | | |
| | | | RX J1615.3-3255 | 1622-297 | | |
| | | | VV CrA, S CrA, DG CrA | 1933-400 | | |
| 20080803 | 3.14, 3.21 | H214 | MY Lup | 1600-44 | Uranus | Mostly nice weather |
| | | | VV CrA, S CrA, DG CrA | 1933-400 | | |
| 20080804 | 3.14, 3.21 | H214 | Sz 65 & Sz 66 | 1622-297 | Uranus | Weather less than perfect |
| 20080805 | 6.48, 6.78 | H214 | MY Lup, IM Lup | 1600-44 | Uranus | Weather improving |

Table 4.10: Overview of the CARMA observations.

| Obs. date | $\lambda\lambda$ (mm) | Config. | Target sources[a] | Gain calibrator(s) | Flux cal. | Notes |
|---|---|---|---|---|---|---|
| 20080424 | 1.33 | C | EC 82, EC 90, 18290088+0029315 | 1743-038 | 3c454.3 | Gain cal. too weak |
| 20080426 | 1.33 | C | 18290088+0029315, IRAS 18268-0025, CoKu Ser G3, 18285808+0017244, 18285020+0009497, 18294410+0033561, VV Ser | 1743-038 | 3c454.3 | Gain cal. too weak |
| 20080501 | 1.33 | C | 18293619+0042167, GSC 00446-00153 | 1743-038 | 3c454.3 | Gain cal. too weak |
| 20080518 | 1.33 | C | GSC 00446-00153 | 1751+096 | 3c454.3 | |
| 20080521 | 3.15 | C | EC 82, EC 90, 18290088+0029315, IRAS 18268-0025, 18285808+0017244, 18285020+0009497, VV Ser | 1743-038 | 3c273 | Gain cal. too weak |
| 20080618 | 3.15 | D | EC 82, EC 90, 18290088+0029315, IRAS 18268-0025, CoKu Ser G3, VV Ser | 1751+096 | 3c279 | |
| 20080619 | 3.15 | D | 18285808+0017244, 18285020+0009497, 18294410+0033561, 18293619+0042167 | 1751+096 | 3c273 | |
| 20080620 | 1.33 | D | EC 82, EC 90, 18290088+0029315, IRAS 18268-0025, CoKu Ser G3, VV Ser, 18285808+0017244, 18285020+0009497 | 1751+096 | 3c273 | |
| 20080622 | 3.15 | D | 18293619+0042167, GSC 00446-00153 | 1751+096 | 3c273 | |
| 20080704 | 1.33 | D | EC 97, 18285020+0009497, 18294410+0033561, 18293619+0042167, GSC 00446-00153 | 1751+096 | 3c279 | |

[a] In the case of SSTc2d names, only the coordinates (in J2000) are shown.

Table 4.11: Overview of the VLA observations.

| Obs. date | $\lambda\lambda$ (mm) | Config. | Target sources[a] | Gain calibrator(s) | Flux cal. | Notes |
|---|---|---|---|---|---|---|
| 20080310 | 6.92, 6.93 | C | CoKu Ser G3, EC 82 18290088+0029315, EC 90, VV Ser, EC 97, 18285020+0009497 | 1824+013 | 3c286 | Clouds forming |
| 20080311 | 13.4 | C | CoKu Ser G3, 18290088+0029315, EC 90, VV Ser, EC 97 | 1851+005 | 3c286 | Clear sky. |
| 20080313 | 13.4 | C | 18285020+0009497, 18290980+0034459, EC 82 | 1851+005 | 3c286 | Clouds forming |
| 20080314 | 35.5 | C | EC 82, EC 90, 18295020+0009497, EC 97, VV Ser, | 1804+010 | 3c286 | High winds. |
| 20080315 | 61.4, 62.0 | C | CoKu Ser G3, 18290088+0029315, EC 82, EC 90, 18295020+0009497, EC 97, CoKu Ser G3, 18290088+0029315, VV Ser, 18285020+0009497 | 1804+010 | 3c286 | High winds. |

[a] In the case of SSTc2d names, only the coordinates (in J2000) are shown.

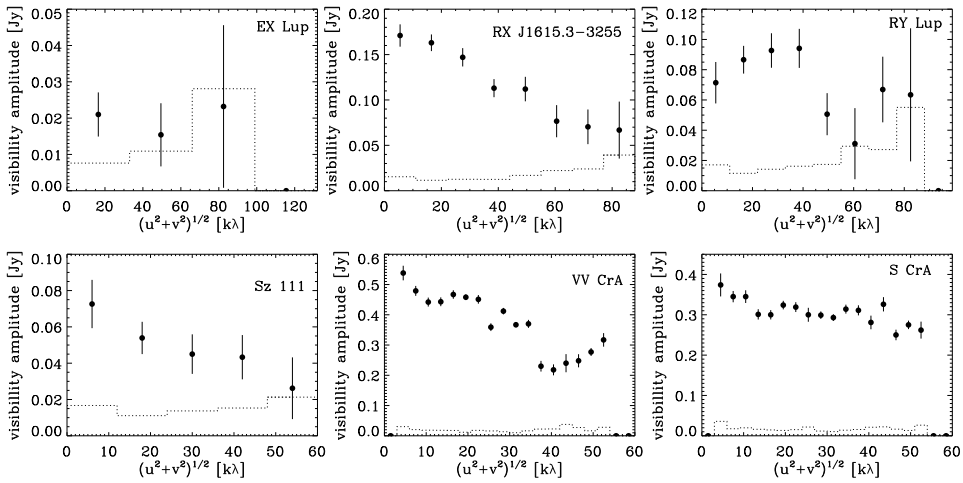


Figure 4.9: Amplitude as a function of ($u$, $v$) distance for sources detected with the SMA at 1 mm. The data points give the vector-averaged amplitude per bin, where the data are binned in annuli according to $(u, v)$ distance. The error bars show the statistical $1\sigma$ errors and the dotted lines give the expected amplitude for zero signal.

## 4.8 Appendix: results

The complete results of the SMA observations are shown in Table 4.12. The amplitude as a function of ($u$, $v$) distance is plotted in Fig. 4.9.

The complete results of the ATCA observations at 3 mm are shown in Table 4.13, those of the ATCA observations at 7 mm in Table 4.14. Several sources were observed at the same wavelength more than once. The data for those sources were co-added in the ($u$, $v$) plane to improve the signal-to-noise ratio. The resulting fluxes or $3\sigma$ upper limits are presented in Tables 4.4 and 4.5.

The binary VV CrA was not resolved with the ATCA at 3 or 7 mm using natural weighting, which is optimised for sensitivity. However, using uniform weighting, which is optimised for resolution, the binary could be resolved at 3 mm. The map is shown in Fig. 4.10. The amplitude as a function of ($u$, $v$) distance of the sources detected with the ATCA at 3 mm is plotted in Fig. 4.11, that of the sources detected with the ATCA at 7 mm in Fig. 4.12.

The complete results of the CARMA observations at 1 mm are shown in Table 4.15, those of the CARMA observations at 3 mm in Table 4.16. Some sources were observed twice, once in the C and once in the D configuration. If good data

Table 4.12: Complete results of SMA observations at 1.3 mm.

| Obs. date | $\lambda_{\rm eff}$ (mm) | Target source[a] | Continuum flux[b] (P) | (G) | rms[c] | Gaussian size (arcsec) | RA[b] (J2000) | Dec[b] (J2000) |
|---|---|---|---|---|---|---|---|---|
| 20080419 | 1.34 | EX Lup | 19.3 | 21.3 | 4.0 | 1.00 ± 1.34 | 16 03 05.0 | -40 18 20.1 |
| | | RX J1615.3-3255 | 131.8 | 169.1 | 3.9 | 1.53 ± 0.13 | 16 15 20.2 | -32 55 05.3 |
| | | RY Lup | 78.3 | 89.0 | 5.0 | 1.14 ± 0.30 | 15 59 28.4 | -40 21 51.4 |
| | | 161029.6-392215 | < 13.1[d] | | 4.4 | – | 16 10 29.6 | -39 22 14.4 |
| | | 161159.9-382337 | < 12.7[d] | | 4.2 | – | 16 11 59.8 | -38 23 38.0 |
| | | Sz 111 | 49.3 | 52.5 | 4.2 | 0.78 ± 0.67 | 16 08 54.7 | -39 37 43.6 |
| | | Sz 91 | < 13.0[d] | | 4.3 | – | 16 07 11.6 | -39 03 47.1 |
| | | Sz 96 | < 12.6[d] | | 4.2 | – | 16 08 12.6 | -39 08 33.3 |
| 20081001 | 1.35 | VV CrA | 349.6 | 367.0 | 5.1 | 0.96 ± 0.06 | 19 03 06.8 | -37 12 49.3 |
| | | S CrA | 301.4 | 322.2 | 3.5 | 0.91 ± 0.07 | 19 01 08.6 | -36 57 20.6 |
| | | DG CrA | < 6.6[d] | | 2.2 | – | 19 01 55.2 | -37 23 40.5 |

[a] In the case of SSTc2d names, only the coordinates (in J2000) are shown.

[b] Continuum flux and position are from fits in the ($u$, $v$) plane. For sources that were detected at $3\sigma$, both the point-source flux (P) and the integrated flux for a Gaussian (G) are shown. For sources that were not detected, the coordinates of the phase centre are quoted.

[c] Calculated from the cleaned image.

[d] Quoted value is $3\sigma$ upper limit.

Table 4.13: Complete results of ATCA observations at 3 mm.

| Obs. date | $\lambda_{\rm eff}$ (mm) | Target source | Continuum flux[a] (P) | (G) | rms[b] | Gaussian size (arcsec) | RA[a] (J2000) | Dec[a] (J2000) |
|---|---|---|---|---|---|---|---|---|
| 20080712 | 3.18 | HBC 556 | | < 3.7 | 1.2 | – | 8 10 31.3 | -36 01 46.5 |
| | | HBC 557 | | < 3.2 | 1.1 | – | 8 12 47.4 | -36 19 18.0 |
| | | HBC 559 | | < 3.3 | 1.1 | – | 8 13 56.4 | -36 08 02.1 |
| 20080729 | 3.18 | HBC 559 | | < 4.3 | 1.4 | – | 8 13 51.0 | -36 08 02.1 |
| | | SZ Cha | | < 3.0 | 1.0 | – | 10 58 10.0 | -77 17 17.6 |
| | | Sz 32 | | < 2.9 | 1.0 | – | 11 09 48.0 | -76 34 26.0 |
| 20080730 | 3.18 | SZ Cha | 3.4 | 5.8 | 0.5 | 1.95 ± 0.63 | 10 58 16.6 | -77 17 17.0 |
| 20080802 | 3.18 | SZ Cha | | < 2.9 | 1.0 | – | 10 58 15.5 | -77 17 17.6 |
| | | Sz 111 | 5.7 | –[d] | 0.7 | – | 16 08 54.6 | -39 37 53.3 |
| | | RY Lup | | < 2.3 | 0.8 | – | 15 59 28.0 | -40 21 51.2 |
| | | RX J1615.3-3255 | 6.8 | –[c] | 0.6 | – | 16 15 20.2 | -32 55 05.6 |
| | | VV CrA a | 31.0 | 69.5[d] | 1.2 | 2.56 ± 0.21[d] | 19 03 06.8 | -37 12 49.8 |
| | | VV CrA b | 25.1 | 69.5[d] | | 2.56 ± 0.21[d] | 19 03 06.9 | -37 12 48.3 |
| | | S CrA | 22.0 | –[c] | 1.1 | – | 19 01 08.6 | -36 57 20.2 |
| | | GN 18.57.8 | 7.1 | 13.1 | | 1.45 ± 0.52 | 19 01 07.9 | -36 57 16.9 |
| | | DG CrA | | < 3.0 | 1.0 | – | 19 01 54.9 | -37 23 40.5 |
| 20080803 | 3.18 | MY Lup | 8.7 | –[c] | 0.4 | – | 16 00 44.5 | -41 55 31.2 |
| | | VV CrA a | 23.0 | 44.2[d] | 1.9 | 2.28 ± 0.38[d] | 19 03 06.8 | -37 12 49.9 |
| | | VV CrA b | 21.9 | 44.2[d] | | 2.28 ± 0.38[d] | 19 03 06.9 | -37 12 48.4 |
| | | S CrA | 24.9 | –[c] | 1.9 | – | 19 01 08.6 | -36 57 20.6 |
| | | GN 18.57.8 | 8.2 | –[c] | | – | 19 01 07.9 | -36 57 15.2 |
| | | DG CrA | | < 4.3 | 1.4 | – | 19 01 54.9 | -37 23 40.5 |
| 20080804 | 3.18 | Sz 65 | 3.4 | –[c] | 0.4 | – | 15 39 27.7 | -34 46 17.6 |
| | | Sz 66 | 2.2 | –[c] | | – | 15 39 28.2 | -34 46 17.9 |

[a] Continuum flux and position are from fits in the ($u$, $v$) plane. For sources that were detected at $3\sigma$, both the point-source flux (P) and the integrated flux for a Gaussian (G) are shown. For sources that were not detected, the coordinates of the phase centre are quoted and $3\sigma$ upper limits are quoted.

[b] Calculated from the cleaned image.

[c] No circular Gaussian could be fit to the source in the ($u$, $v$) plane.

[d] Value is for the two components of VV CrA combined.

Table 4.14: Complete results of ATCA observations at 7 mm.

| Obs. date | $\lambda_{\rm eff}$ (mm) | Target source | Continuum flux[a] (P) | (G) | rms[b] | Gaussian size (arcsec) | RA[a] (J2000) | Dec[a] (J2000) |
|---|---|---|---|---|---|---|---|---|
| 20080713 | 6.83 | HBC 556 | | < 0.7[c] | 0.2 | – | 8 10 31.6 | -36 01 46.5 |
| | | HBC 557 | | < 0.4[c] | 0.1 | – | 8 12 47.7 | -36 19 18.0 |
| | | HBC 559 | | < 0.6[c] | 0.2 | – | 8 13 56.8 | -36 08 02.1 |
| 20080728 | 6.85 | HBC 559 | | < 0.3[c] | 0.1 | – | 8 13 56.8 | -36 08 02.1 |
| 20080801 | 6.85 | Sz 111 | | < 0.6[c] | 0.2 | – | 16 08 53.8 | -39 37 43.1 |
| | | RY Lup | | < 0.6[c] | 0.2 | – | 15 59 27.5 | -40 21 51.2 |
| | | RX J1615.3-3255 | | < 0.5[c] | 0.2 | – | 16 15 19.4 | -32 55 05.0 |
| | | VV CrA | 3.4 | 3.4 | 0.2 | (unresolved) | 19 03 06.8 | -37 12 49.3 |
| | | S CrA | 3.7 | 5.4 | 0.2 | 3.12 ± 0.81 | 19 01 08.6 | -36 57 20.3 |
| | | DG CrA | | < 0.6[c] | 0.2 | – | 19 01 54.4 | -37 23 40.5 |
| 20080805 | 6.65 | MY Lup | 1.3 | 2.9 | 0.1 | 4.75 ± 1.31 | 16 00 44.6 | -41 55 31.5 |
| | | IM Lup | 2.2 | 2.2 | 0.2 | (unresolved) | 15 56 09.2 | -37 56 06.0 |

[a] Continuum flux and position are from fits in the ($u$, $v$) plane. For sources that were detected at $3\sigma$, both the point-source flux (P) and the integrated flux for a Gaussian (G) are shown. For sources that were not detected, the coordinates of the phase centre are quoted.

[b] Calculated from the cleaned image.

[c] Quoted value is $3\sigma$ upper limit.

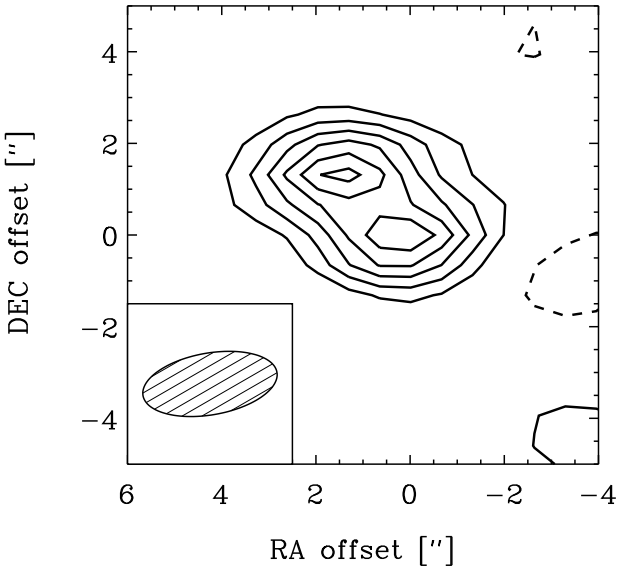


Figure 4.10: Image of VV CrA, observed at 3.2 mm on 2 and 3 August 2008. The offsets are with respect to the phase centre, which is located at 19:03:06.7, -37:12:49.7. The contours are at 2, 4, 6, ... times the rms of 2.0 mJy/beam; negative contours are dashed.

were obtained in both occasions, they were co-added in the ($u$, $v$) plane to improve the signal-to-noise ratio. The resulting fluxes or $3\sigma$ upper limits are presented in Tables 4.4 and 4.5. The amplitude as a function of ($u$, $v$) distance of the sources detected with CARMA at 1 mm is plotted in Fig. 4.13, that of the sources detected with CARMA at 3 mm in Fig. 4.14.

The complete results of the VLA observations at 7 mm and 1 cm are shown in Table 4.17, those of the VLA observations at 3.5 and 6.2 cm in Table 4.18.

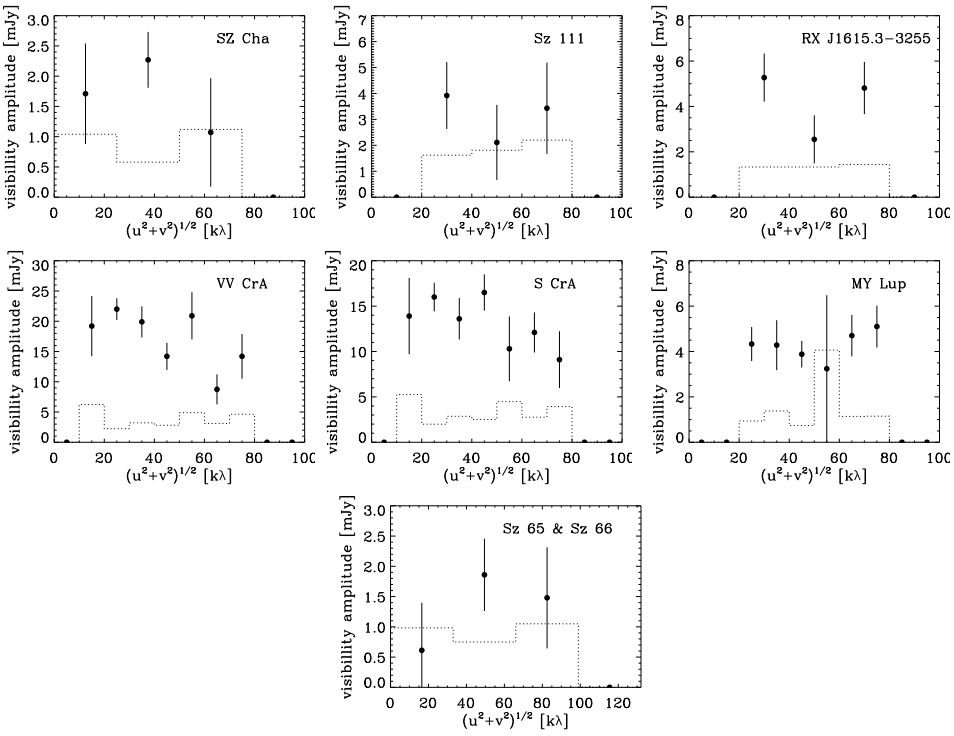


Figure 4.11: Amplitude as a function of ($u$, $v$) distance for sources detected with the ATCA at 3 mm. The data points give the vector-averaged amplitude per bin, where the data are binned in annuli according to $(u, v)$ distance. The error bars show the statistical $1\sigma$ errors and the dotted lines give the expected amplitude for zero signal.

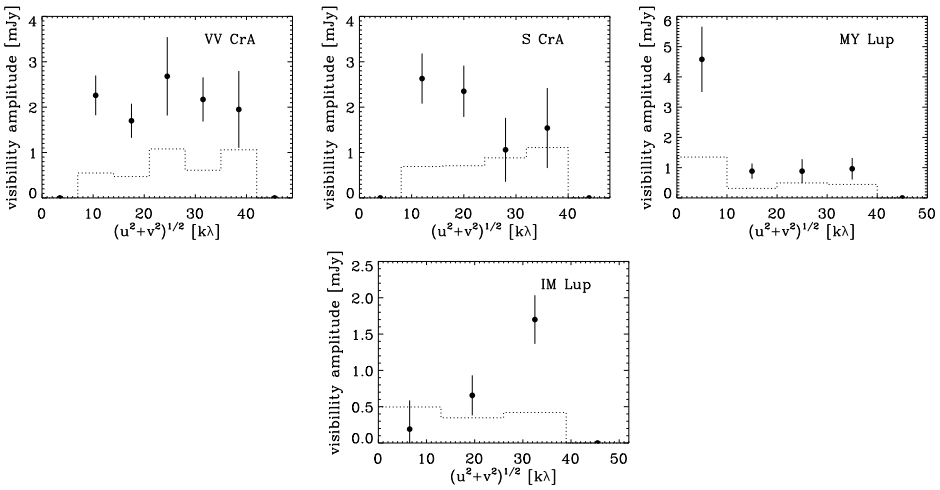


Figure 4.12: Amplitude as a function of ($u$, $v$) distance for sources detected with the ATCA at 7 mm. The data points give the vector-averaged amplitude per bin, where the data are binned in annuli according to $(u, v)$ distance. The error bars show the statistical $1\sigma$ errors and the dotted lines give the expected amplitude for zero signal.

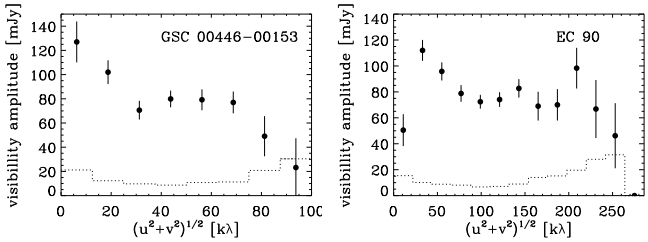


Figure 4.13: Amplitude as a function of ($u$, $v$) distance for sources detected with CARMA at 1 mm. The data points give the vector-averaged amplitude per bin, where the data are binned in annuli according to $(u, v)$ distance. The error bars show the statistical $1\sigma$ errors and the dotted lines give the expected amplitude for zero signal.

Table 4.15: Complete results of CARMA observations at 1 mm.

| Obs. date | $\lambda_{\rm eff}$ (mm) | Target source[a] | Continuum flux[b] (P) | (G) | rms[c] | Gaussian size (arcsec) | RA[b] (J2000) | Dec[b] (J2000) |
|---|---|---|---|---|---|---|---|---|
| 20080518 | 1.33 | GSC 00446-00153 | 43.6 | 50.5 | 6.0 | 0.46 ± 0.32 | 18 30 06.2 | +00 42 33.6 |
| 20080620 | 1.33 | EC 82 | < 15.7[d] | | 5.2 | – | 18 29 56.8 | +01 14 46.0 |
| | | EC 90 | 91.8 | 91.7 | 10.4 | (unresolved) | 18 29 57.7 | +01 14 07.0 |
| | | 18290088+0029315 | < 16.4[d] | | 5.5 | – | 18 29 00.9 | +00 29 31.6 |
| | | IRAS 18268-0025 | < 15.6[d] | | 5.2 | – | 18 29 28.2 | -00 22 57.1 |
| | | CoKu Ser G3 | < 17.1[d] | | 5.7 | – | 18 29 01.8 | +00 29 54.6 |
| | | VV Ser | < 14.8[d] | | 4.9 | – | 18 29 47.9 | +00 08 40.0 |
| | | 18285808+0017244 | < 24.6[d] | | 8.2 | – | 18 28 58.1 | +00 17 24.4 |
| | | 18285020+0009497 | < 98.2[d] | | 32.7 | – | 18 28 50.2 | +00 09 49.7 |
| 20080704 | 1.33 | EC 97 | < 23.3[d] | | 7.8 | – | 18 29 58.2 | +01 15 22.0 |
| | | 18285020+0009497 | < 22.8[d] | | 7.6 | – | 18 28 50.2 | +00 09 49.7 |
| | | 18294410+0033561 | < 15.0[d] | | 5.0 | – | 18 29 44.1 | +00 35 56.1 |
| | | 18293619+0042167 | < 8.7[d] | | 2.9 | – | 18 29 36.2 | +00 42 16.7 |
| | | GSC 00446-00153 | 90.8 | 97.6 | 2.8 | 0.67 ± 0.23 | 18 30 06.2 | +00 42 33.6 |

[a] In the case of SSTc2d names, only the coordinates (in J2000) are shown.

[b] Continuum flux and position are from fits in the ($u$, $v$) plane. For sources that were detected at $3\sigma$, both the point-source flux (P) and the integrated flux for a Gaussian (G) are shown. For sources that were not detected, the coordinates of the phase centre are quoted.

[c] Calculated from the cleaned image.

[d] Quoted value is $3\sigma$ upper limit.

Table 4.16: Complete results of CARMA observations at 3 mm.

| Obs. date | $\lambda_{\rm eff}$ (mm) | Target source[a] | Continuum flux[b] (P) | (G) | rms[c] | Gaussian size (arcsec) | RA[b] (J2000) | Dec[b] (J2000) |
|---|---|---|---|---|---|---|---|---|
| 20080618 | 3.15 | EC 82 | | < 2.9[d] | 1.0 | – | 18 29 56.8 | +01 14 46.0 |
| | | EC 90 | 11.3 | 11.6 | 1.0 | 1.69 ± 0.97 | 18 29 57.8 | +01 14 06.9 |
| | | 18290088+0029315 | 3.4 | 3.9 | 0.6 | (unresolved) | 18 29 00.9 | +00 29 31.7 |
| | | IRAS 18268-0025 | | < 1.9[d] | 0.6 | – | 18 29 28.2 | -00 22 57.1 |
| | | CoKu Ser G3 | | < 1.6[d] | 0.5 | – | 18 29 01.8 | +00 29 54.6 |
| | | VV Ser | | < 1.8[d] | 0.6 | – | 18 28 47.9 | +00 08 40.0 |
| 20080619 | 3.15 | 18285808+0017244 | | < 1.9[d] | 0.6 | – | 18 28 58.1 | +00 17 24.4 |
| | | 18285020+0009497 | | < 1.9[d] | 0.6 | – | 18 28 50.2 | +00 09 49.7 |
| | | 18294410+0033561 | | < 1.7[d] | 0.6 | – | 18 29 44.1 | +00 33 56.1 |
| | | 18293619+0042167 | | < 2.7[d] | 0.9 | – | 18 29 36.2 | +00 42 16.7 |
| 20080622 | 3.15 | 18293619+0042167 | | < 5.3[d] | 1.8 | – | 18 29 36.2 | +00 42 16.7 |
| | | GSC 00446-00153 | 6.8 | 8.1 | 1.0 | 2.71 ± 1.58 | 18 30 06.3 | +00 42 34.2 |

[a] In the case of SSTc2d names, only the coordinates (in J2000) are shown.

[b] Continuum flux and position are from fits in the ($u$, $v$) plane. For sources that were detected at $3\sigma$, both the point-source flux (P) and the integrated flux for a Gaussian (G) are shown. For sources that were not detected, the coordinates of the phase centre are quoted.

[c] Calculated from the cleaned image.

[d] Quoted value is $3\sigma$ upper limit.

Table 4.17: Complete results of VLA observations at 6.9 mm and 1.3 cm.

| Obs. date | $\lambda_{\rm eff}$ (mm) | Target source[a] | Continuum flux[b] (Peak) | (Integ.) | rms[c] | Gaussian size (arcsec) | RA[b] (J2000) | Dec[b] (J2000) |
|---|---|---|---|---|---|---|---|---|
| 20080310 | 6.93 | CoKu Ser G3 | $< 1.2^{\rm d}$ | | 0.4 | – | 18 29 01.8 | +00 29 54.5 |
| | | 18290088+0029315 | $< 0.7^{\rm d}$ | | 0.2 | – | 18 29 00.9 | +00 29 31.5 |
| | | EC 90 | $< 1.0^{\rm d}$ | | 0.3 | – | 18 29 57.7 | +01 14 05.7 |
| | | VV Ser | $< 0.7^{\rm d}$ | | 0.2 | – | 18 28 47.9 | +00 08 39.8 |
| | | EC 97 | $< 0.6^{\rm d}$ | | 0.2 | – | 18 29 58.2 | +01 15 21.7 |
| | | 18285020+0009497 | $< 0.6^{\rm d}$ | | 0.2 | – | 18 28 50.2 | +00 09 49.6 |
| | | EC 82 | $< 0.5^{\rm d}$ | | 0.2 | – | 18 29 56.9 | +01 14 46.4 |
| 20080311 | 13.4 | CoKu Ser G3 | 8.66 | 9.81 | 0.06 | $1.17 \times 0.91$ | 18 29 01.8 | +00 29 54.8 |
| | | 18290088+0029315 | $< 0.17^{\rm d}$ | | 0.06 | – | 18 29 00.9 | +00 29 31.5 |
| | | EC 90 | $< 0.24^{\rm d}$ | | 0.08 | – | 18 29 57.7 | +01 14 05.7 |
| | | VV Ser | $< 0.17^{\rm d}$ | | 0.06 | – | 18 28 47.9 | +00 08 39.8 |
| | | EC 97 | $< 0.15^{\rm d}$ | | 0.05 | – | 18 29 58.2 | +01 15 21.7 |
| 20080313 | 13.4 | 18285020+0009497 | $< 0.20^{\rm d}$ | | 0.07 | – | 18 28 50.2 | +00 09 49.6 |
| | | 18290980+0034459 | $< 0.23^{\rm d}$ | | 0.08 | – | 18 29 09.8 | +00 34 45.8 |
| | | EC 82 | $< 0.28^{\rm d}$ | | 0.09 | – | 18 29 56.9 | +01 14 46.4 |

[a] In the case of SSTc2d names, only the coordinates (in J2000) are shown.

[b] Continuum flux and position are obtained using the AIPS task JMFIT, which fits elliptical Gaussians to the cleaned image. For sources that were detected at $3\sigma$, both the peak (Peak) and the integrated (Integ.) flux are shown. For sources that were not detected, the coordinates of the phase centre are quoted.

[c] Calculated from the cleaned image.

[d] Quoted value is $3\sigma$ upper limit.

Table 4.18: Complete results of VLA observations at 3.5 and 6.2 cm.

| Obs. date | $\lambda_{\rm eff}$ (mm) | Target source[a] | Continuum flux[b] (Peak) | (Integ.) | rms[c] | Gaussian size (arcsec) | RA[b] (J2000) | Dec[b] (J2000) |
|---|---|---|---|---|---|---|---|---|
| 20080314 | 35.5 | EC 82 | $< 0.09$[d] | | 0.03 | – | 18 29 56.0 | +01 14 49.9 |
| | | EC 90 | $< 0.09$[d] | | 0.03 | – | 18 29 56.0 | +01 14 49.0 |
| | | EC 97 | $< 0.09$[d] | | 0.03 | – | 18 29 56.0 | +01 14 49.0 |
| | | CoKu Ser G3 | 1.11 | 1.11 | 0.03 | $2.49 \times 2.35$ | 18 29 01.8 | +00 29 54.7 |
| | | 18290088+0029315 | $< 0.10$[d] | | 0.03 | – | 18 29 05.0 | +00 29 44.0 |
| | | VV Ser | 0.14 | 0.17 | 0.03 | $3.25 \times 2.31$ | 18 28 47.9 | +00 08 40.1 |
| | | 18285020+0009497 | $< 0.08$[d] | | 0.03 | – | 18 28 40.0 | +00 09 13.0 |
| 20080315 | 61.7 | EC 82 | $< 0.09$[d] | | 0.03 | – | 18 29 57.0 | +01 14 40.0 |
| | | EC 90 | $< 0.09$[d] | | 0.03 | – | 18 29 57.0 | +01 14 40.0 |
| | | EC 97 | $< 0.09$[d] | | 0.03 | – | 18 29 57.0 | +01 14 40.0 |
| | | CoKu Ser G3 | 0.91 | 1.00 | 0.04 | (unresolved) | 18 29 01.9 | +00 29 54.9 |
| | | 18290088+0029315 | $< 0.12$[d] | | 0.04 | – | 18 29 07.0 | +00 32 09.0 |
| | | VV Ser | $< 0.14$[d] | | 0.05 | – | 18 29 47.0 | +00 09 11.0 |
| | | 18285020+0009497 | $< 0.14$[d] | | 0.05 | – | 18 29 47.0 | +00 09 11.0 |

[a] In the case of SSTc2d names, only the coordinates (in J2000) are shown.

[b] Continuum flux and position are obtained using the AIPS task JMFIT, which fits elliptical Gaussians to the cleaned image. For sources that were detected at $3\sigma$, both the peak (Peak) and the integrated (Integ.) flux are shown. For sources that were not detected, the coordinates of the phase centre are quoted.

[c] Calculated from the cleaned image.

[d] Quoted value is $3\sigma$ upper limit.

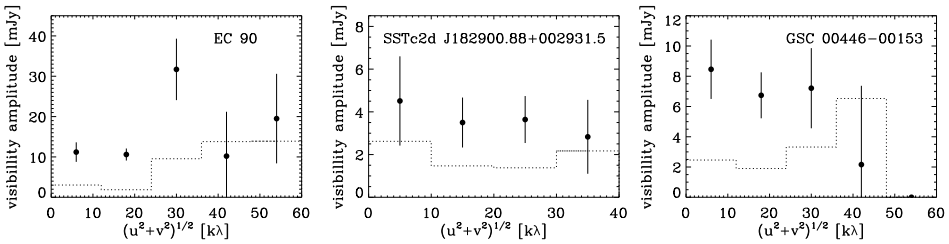


Figure 4.14: Amplitude as a function of ($u$, $v$) distance for sources detected with CARMA at 3 mm. The data points give the vector-averaged amplitude per bin, where the data are binned in annuli according to $(u, v)$ distance. The error bars show the statistical $1\sigma$ errors and the dotted lines give the expected amplitude for zero signal.

# Chapter 5

# Large grains in discs around young stars: ATCA observations of WW Cha, RU Lup, and CS Cha

**Abstract**

Grains in discs around young stars grow from interstellar sub$\mu$m sizes to planetesimals, up to thousands of km in size, over the course of several Myr. Thermal emission of large grains or pebbles is best observed at cm wavelengths, but other emission mechanisms also contribute, such as free-free emission from stellar winds and chromospheric activity. We aim to determine the mechanisms of cm emission for three T-Tauri stars. WW Cha and RU Lup were recently found to have grain growth at least up to mm sizes in their circumstellar discs, based on millimetre data up to 3.3 mm. CS Cha has similar indications for grain growth in its circumbinary disc. The T-Tauri stars WW Cha and RU Lup are monitored over the course of several years at mm and cm wavelengths, using the Australia Telescope Compact Array (ATCA). The new ATCA 7 mm system is also used to observe CS Cha at 7 mm. WW Cha is detected on several occasions at 7 and 16 mm. We obtain one detection of WW Cha at 3.5 cm and upper limits only for 6.3 cm. The emission at 16 mm is stable over periods of days, months and years, whereas the emission at 3.5 cm is variable. RU Lup was detected at 7 mm. It was observed at 16 mm three times and at 3 and 6 cm four times and is variable in all three wavebands. CS Cha is detected at 7 mm, but the signal-to-noise ratio was not high enough to resolve the gap in the circumbinary disc. The typical resolution of the 7 and 16 mm observations was 5–10″ with rms $\sim$ 0.2 mJy. The emission at 3, 7 and 16 mm for WW Cha is well explained by thermal emission from mm- and cm-sized pebbles. The cm spectral index between 3.5 and 6.3 cm is consistent with emission from an optically thick ionised wind, but the high variability of the cm emission points to a non-thermal contribution. The spectral energy distributions of both RU Lup and CS Cha from 1 to 7 mm are consistent with thermal emission from mm-sized grains. The variability of the longer-wavelength emission for RU Lup and the negative spectral index suggests non-thermal emission, arising from an optically thin plasma.

Dave Lommen, Sarah Maddison, Chris Wright, Ewine van Dishoeck,
David Wilner, Tyler Bourke
Astronomy & Astrophysics 2009, 495, 869

## 5.1 Introduction

Planet formation takes place in the discs around young stellar objects (YSOs), where submicron-sized grains have to grow to planet size in about 10 Myr or less (Haisch et al. 2001; Carpenter et al. 2005; Setiawan et al. 2008). The very first step, where the grains grow from submicron size to several microns, may be traced by the 10-$\mu$m silicate feature. Silicates of a few microns in size give considerably flatter features than those of submicron sizes (e.g., Przygodda et al. 2003). However, the strength and shape of the 10-$\mu$m feature may also be influenced by the crystallinity of the grains (e.g., Meeus et al. 2003), or by their porosity (Voshchinnikov & Henning 2008). Furthermore, the 10-$\mu$m silicate feature only probes the surface layers of the circumstellar discs.

Growth up to millimetre (mm) sizes can be more readily observed by looking at the mm slope in the spectral energy distribution (SED). From the slope $\alpha$, where $F_\nu \propto \nu^\alpha$, the opacity index $\beta$ in the mm regime, where $\kappa_\nu \propto \nu^\beta$, can be obtained through

$$\beta \approx (\alpha - 2)(1 + \Delta), \tag{5.1}$$

where $\Delta$ is the ratio of optically thick to optically thin emission from the disc (Beckwith et al. 1990; Beckwith & Sargent 1991; Rodmann et al. 2006). An opacity index $\beta \approx 1$ indicates that grains have grown at least up to mm sizes, irrespective of their exact physical structure (Draine 2006). Indeed, about 30 sources with grains up to at least mm sizes have been found over the past several years (Natta et al. 2004; Rodmann et al. 2006; Andrews & Williams 2007).

The next step, growth to centimetre (cm) sizes and beyond, is much harder to observe directly. The reason for this is that at cm wavelengths, where these "pebbles" can be observed, the emission is several orders of magnitudes weaker than at mm wavelengths. Furthermore, other processes such as chromospheric activity (Forbrich et al. 2007), gyrosynchrotron emission (André et al. 1988), electron-cyclotron maser emission (Dulk 1985; Smith et al. 2003) or an ionised wind (Girart et al. 2004) may also contribute significantly to the cm emission. A particularly interesting source of variable cm emission may be that from (interacting) helmet streamers (Massi et al. 2006, 2008). To rule out these other cm emission mechanisms, the sources have to be monitored over days, months, and years, to ascertain that the cm emission is optically thin and not variable, and ideally be spatially resolved. So far, TW Hya is the only T-Tauri star that has been monitored over sufficient time periods to safely characterise the cm emission as thermal emission from pebbles (Wilner et al. 2005). [Natta et al. (2004) and Alonso-Albi et al. (2008) also claim thermal emission from cm-sized grains though their ob-

servations have not yet been monitored over an extended period of time.]

In Chapter 3 we observed T-Tauri stars in the southern constellations Lupus and Chamaeleon with the Australia Telescope Compact Array (ATCA[1]) at 3.3 mm, and found three sources that were resolved and had an opacity index $\beta < 1.0$. We chose the two brightest of these, WW Cha and RU Lup, for follow-up observations with the ATCA at 7 mm through 6 cm, the results of which are presented in this paper. The source CS Cha was not resolved at 3 mm but found to have an opacity index of $\beta = 1.0 \pm 0.6$ in Chapter 3 and was added for high-resolution observations at 7 mm.

WW Cha is located in a reflection nebula in the Ced 112 region of the Chamaeleon I molecular cloud, and is thought to drive the highly collimated jets HH 915 and HH 931 (Bally et al. 2006; Wang & Henning 2006). Wang & Henning (2006) claim that two near-infrared molecular-hydrogen emission knots detected by Gómez et al. (2004) on the opposite side of WW Cha may be the counterparts of HH 915. WW Cha has a relatively weak 10-$\mu$m amorphous-silicate feature (Przygodda et al. 2003), indicating that the surface layers are dominated by micron-sized grains. No clear crystalline features are detected in the 10-$\mu$m region. Reipurth et al. (1996) placed the bright mm source Cha-MMS2 about 9″ from IRAS 11083-7618, which is the infared counterpart to the T-Tauri star WW Cha. However, given the similar fluxes found from SEST observations by both Henning et al. (1993) and Reipurth et al. (1996), the lack of other mm sources within several tens of arcseconds, and the fairly large beam used for these and the IRAS observations, we claim that Cha-MMS2 and WW Cha are one and the same source. Another T-Tauri star, Ced 112 IRS 4, is located about 40″ to the north from WW Cha.

RU Lup is a very active and well-studied T-Tauri star, showing variability in the optical, UV and X-ray bands (e.g. Lamzin et al. 1996; Stempels & Piskunov 2002; Herczeg et al. 2005; Robrade & Schmitt 2007). The mass accretion rate onto the central star is found to be relatively large, at $\sim 10^{-7}$ $M_\odot$ yr$^{-1}$ (Lamzin et al. 1996; Podio et al. 2007). Stempels & Piskunov (2002) studied the variations in the radial velocity in RU Lup, which they found to be periodic with a period of 3.71 days. Stempels & Piskunov attribute this periodic variability to long-lived star spots, and find the solution of a substellar companion unlikely. Olofsson et al. (2009, in prep.) show a very strong and boxy 10-$\mu$m feature for RU Lup, indicating the presence of submicron-sized particles in the disc photosphere. Contributions from crystalline silicates are detected between 20 and 35 $\mu$m (Kessler-Silacci

[1]The Australia Telescope Compact Array is part of the Australia Telescope which is funded by the Commonwealth of Australia for operation as a National Facility managed by CSIRO.

Table 5.1: Source list of sources observed with the ATCA.

| Source | Cloud | Distance[a] (pc) | Age[b] (Myr) | Luminosity[b] ($L_\odot$) | Mass[b] ($M_\odot$) | Spectral type[c] |
|---|---|---|---|---|---|---|
| WW Cha | Cha I | 160 ± 15 | 0.4–0.8 | 2.2 | 0.6–0.8 | K5 |
| RU Lup | Lup II | 140 ± 20 | 0.04–0.5 | 2.1 | 2.0–2.8 | K7-M0 |
| CS Cha | Cha I | 160 ± 15 | 2–3 | 1.3 | 0.9–1.2 | K4 |

[a] Distances from Whittet et al. (1997) (WW Cha and CS Cha) and Hughes et al. (1993) (RU Lup).

[b] Ages, luminosities and masses from Hughes et al. (1994) (RU Lup) and Lawson et al. (1996) (WW Cha and CS Cha).

[c] Spectral types from Gauvin & Strom (1992) (WW Cha and CS Cha) and Hughes et al. (1994) (RU Lup).

et al. 2006).

CS Cha was classified as a so-called transitional disc by Espaillat et al. (2007). The SEDs of transitional discs show a lack of infrared emission, indicating a deficit of warm dust close to the star. SEDs of transitional discs are well fit by models that include an inner hole, suggesting that the discs are in a transitional stage. The loss of warm dust can be explained by photo-evaporation, by dust growing to larger sizes and effectively moving the flux to longer wavelengths in the SED, and/or by the presence of an unseen planet that sweeps up material in the inner disc. However, CS Cha was recently found to be a binary (Guenther et al. 2007), and so is now classified as a circumbinary disc rather than a transitional disc. Basic parameters of the sources WW Cha, RU Lup, and CS Cha are presented in Table 5.1.

We here present observations of WW Cha and RU Lup, taken with the ATCA at wavelengths ranging from 7 mm to 6.3 cm, to determine their cm emission mechanisms. We also present ATCA 7 mm observations of the binary CS Cha, with the aim to obtain a longer-wavelength flux point and resolve the hole in the dust disc, which has a diameter of $\sim$ 85 AU (Espaillat et al. 2007), at mm wavelengths. The observations are described in Sect. 5.2, with the basic results presented in Sect. 5.3 and further discussed in Sect. 5.4. Conclusions are presented in Sect. 5.5.

## 5.2 Observations

We present continuum observations of WW Cha, RU Lup, and CS Cha, observed with the ATCA over the period 2006-2008 at 7 and 16 mm and at 3.5 and 6.3 cm. The observations are listed in Table 5.2. ATCA is an array of $6 \times 22$ m antennas, with antenna 6 (CA06) fixed at 6 km. The observations were carried out in double sideband, where each sideband had a bandwidth of 128 MHz. CA06 was only included in the reduction when the array was in an extended configuration (1.5A, 1.5B or 6D – where the number in these array configuration is approximately the longest baseline in kilometres). The data were calibrated and imaged using the MIRIAD package (Sault et al. 1995).

The complex gain calibration was done on the calibrators QSO B1057-797 (for WW Cha and CS Cha) and QSO B1622-297 (for RU Lup), both of which are within 10 degrees of the science targets. The complex gains for RU Lup were twice calibrated using different sources: on QSO B1600-44 (on 9 June 2007) and on QSO B1622-310 (on 4 November 2006).

Normally the absolute flux calibration was done on Uranus at 7 mm and on ATCA's primary flux calibrator QSO B1934-638 at cm wavelengths. QSO B1934-638 is stable at cm wavelengths, and its flux as a function of frequency is well known. On two occasions the absolute flux calibration was done on Mars. The baselines on which Mars was resolved out were not used in the flux calibration. The absolute flux calibration was done on QSO B1057-797 and QSO B1921-293 on four occasions. See Table 5.2 for details.

Using QSO B1057-797 or QSO B1921-293 as an absolute flux calibrator does require some care. However, in some cases we have data very close in time to when the Observatory has published fluxes (e.g., the previous or next day for QSO B1057-797 in October 2007), and the long-term variability of QSO B1057-797 is at most a factor of 2, and that of QSO B1921-293 likely much smaller than that [2]. In this work, we assume an uncertainty in the calibrated flux of about 15%, unless stated otherwise.

Note that for all of our observations the phase centre is offset from the source by one or two synthesised beamwidths in right ascension. This was done to avoid any artefacts at the centre of the field.

[2] see ATCA calibrator pages: `http://www.narrabri.atnf.csiro.au/calibrators/`.

### 5.2.1 WW Cha

Observations of WW Cha at 7 mm were carried out twice in compact configurations. On both days the observations did not include a planet for the flux calibration and the fluxes were calibrated on the gain calibrator QSO B1057-797, resulting in an estimated uncertainty in the absolute flux calibration of 15% in October 2007 and 30% in March 2008. We conducted six observations of WW Cha at 16 mm in the period May 2006-March 2008, all in compact configurations except in November 2007 when an extended array was used. Without a dedicated flux calibrator on 31 March 2008, the estimated uncertainty for this track is 30%. WW Cha was observed at 3 and 6 cm twice.

### 5.2.2 RU Lup

RU Lup was observed at 7 mm just once, while three 16 mm observations were conducted, once in an extended configuration. One of the four observations made at 3 and 6 cm was in an extended array configuration. However a large fraction of the data on the longest baselines had to be flagged, losing the advantage of the extended configuration. Fluxes are thought to be calibrated to an uncertainty of $\sim$10% in October 2006.

### 5.2.3 CS Cha

Because the initial aim for CS Cha was to resolve the hole in the circumbinary disc, this source was only observed while the ATCA was in an extended configuration. CS Cha was observed four times at 7 mm in 2008, including a full track on 30 June, though poor weather rendered these data unusable.

Table 5.2: Overview of the observations.

| Obs. date | $\lambda\lambda$ (mm) | Config. | Flux calibrator | Int.[a] (hr) | Notes (weather, array & data) |
|---|---|---|---|---|---|
| WW Cha, ATCA 7 mm band | | | | | |
| 20071005 | 7.0, 7.3 | H75C | 1057-797 | 1.35 | CA02 offline |
| 20080331 | 7.0, 7.3 | H168 | 1057-797 | 1.99 | |
| WW Cha, ATCA 12 mm band | | | | | |
| 20060508[b] | 16.1, 16.2 | H214C | Mars | 0.80 | CA03+CA04 offline |
| 20061013 | 16.1, 16.2 | H214C | 1934-638 | 1.31 | noisy 16.1 mm data |
| 20061018 | 16.1, 16.2 | EW352 | 1934-638 | 3.32 | noisy 16.1 mm data |
| 20071024 | 15.4, 16.2 | H214C | 1934-638 | 3.15 | worsening conditions |
| 20071102 | 15.4, 16.2 | 1.5A | 1934-638 | 8.48 | |
| 20080331 | 15.4, 16.2 | H168 | 1057-797 | 1.33 | |
| WW Cha, ATCA 3+6 cm bands | | | | | |
| 20061018 | 34.7, 62.5 | EW352 | 1934-638 | 3.95 | a lot of data flagged |
| 20070609 | 34.7, 62.5 | EW352 | 1934-638 | 5.19 | |
| RU Lup, ATCA 7 mm band | | | | | |
| 20071006 | 7.0, 7.3 | H75C | Uranus | 0.99 | CA04 offline |
| RU Lup, ATCA 12 mm band | | | | | |
| 20061011 | 16.1, 16.2 | H214C | 1934-638 | 3.66 | very good conditions |
| 20071024 | 16.1, 16.2 | H214C | 1934-638 | 2.49 | fair conditions |
| 20071104 | 15.4, 16.2 | 1.5A | 1934-638 | 3.79 | fair conditions |
| RU Lup, ATCA 3+6 cm bands | | | | | |
| 20061012 | 34.7, 62.5 | H214C | 1934-638 | 3.53 | very good conditions |
| 20061013 | 34.7, 62.5 | H214C | 1934-638 | 1.70 | very good conditions |
| 20070609 | 34.7, 62.5 | EW352 | 1934-638 | 3.32 | good conditions |
| 20071104 | 34.7, 62.5 | 1.5A | 1934-638 | 3.48 | a lot of data flagged |
| CS Cha, ATCA 7 mm band | | | | | |
| 20080426 | 7.0, 7.3 | 6A | 1921-293 | 6.89 | fair conditions |
| 20080630 | 6.7, 7.0 | 1.5B | Mars | 4.85 | poor conditions |
| 20080705 | 6.7, 7.0 | 1.5B | Uranus | 0.72 | very good conditions |
| 20080706 | 6.7, 7.0 | 1.5B | Uranus | 1.71 | fair conditions |

[a] Total time spent on the science target, before flagging and calibration of data.

[b] Three antennas only.

## 5.3 Results

### 5.3.1 WW Cha

Table 5.3 summarises the fluxes on the different dates at the various wavelengths. Note that in the Table and below the uncertainties do not include the uncertainties from the absolute flux calibration as given in the previous section. Continuum fluxes are from point-source fits in the $(u, v)$ plane, where the source was detected at $3\sigma$ or better. For the cases where WW Cha was not detected to at least $3\sigma$, an upper limit of three times the root mean square of the noise is quoted.

WW Cha was observed with the ATCA at 3.3 mm in August 2005 and reported to have a point-source flux of 25.9 mJy (see Chapter 3). At 7 mm, the source was detected in both sidebands on both occasions at which it was observed, and the fluxes in the two sidebands were consistent from one date to the other to within the uncertainties of the absolute flux calibrations. The fluxes at the different frequencies will be treated as separate observations in the analysis. Figure 5.1 shows WW Cha at 7.3 mm.

WW Cha was observed at 16 mm six times in the period May 2006–March 2008. It was detected in both sidebands each time it was observed except on 13 October 2006, when an upper limit was obtained at 16.1 mm. See Fig. 5.2 for a comparison of the 3 mm and 16 mm detections. For each frequency, the flux is constant over the different observations to within the uncertainties, as demonstrated by Fig. 5.3, which shows the results from point-source fits in the $(u, v)$ plane at 16.2 mm, where CA06 was not included in the 2 November 2007 data for consistency. Taking the arithmetic mean of the fluxes and quadratic mean of the uncertainties given in Table 5.3, average point-source fluxes of $0.81 \pm 0.16$, $0.99 \pm 0.26$ and $0.98 \pm 0.19$ mJy at 15.4, 16.1, and 16.2 mm respectively were obtained.

WW Cha was observed at 3.5 and 6.3 cm twice. A $3\sigma$ upper limit of 0.22 mJy at 3.5 cm was found on 18 October 2006, whilst on 9 June 2007 a point-source flux of $0.63 \pm 0.06$ mJy detected, demonstrating that the emission varies by a factor of 3 within a year. The emission at 3.5 cm was found to be unpolarised down to the noise level on 9 June 2007. $3\sigma$ upper limits of 0.20 and 0.40 mJy were determined at 6.3 cm on these two dates.

In conclusion, WW Cha is detected at 3, 7, 16 mm and 3.5 cm, and upper limits were found at 6.3 cm, as depicted in Fig. 5.4. Most notably, the source was detected at 16 mm six out of six times, and found stable over periods varying from days to years, while the 3.5 cm emission was found to vary.

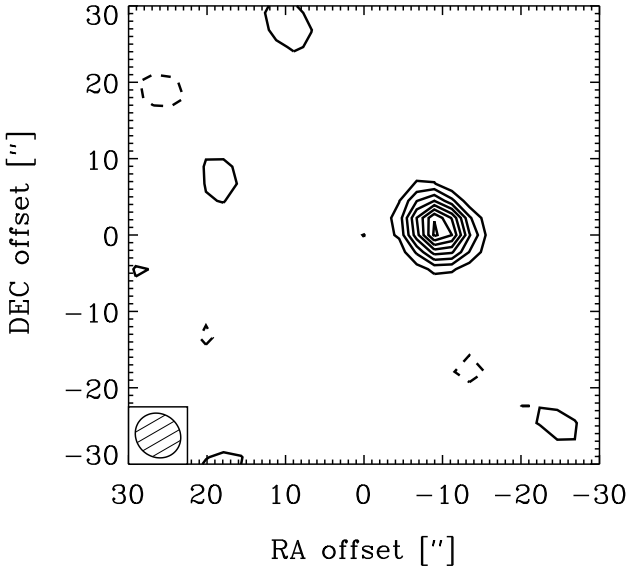


Figure 5.1: Image of WW Cha, observed at 7.3 mm on 31 March 2008. The offsets are with respect to the phase centre, which is located at 11:10:02.7, -76:34:59.0 (J2000); peak emission coincides with the position of the optical star. The contours are at 2, 4, 6, ... times the rms of 0.20 mJy/beam; negative contours are dashed.

**Other sources in the field**

At 16.2 mm, a second source was detected about 40″ to the north-west of WW Cha. This source was identified with the YSO Ced 112 IRS 4 – see Fig. 5.2. The data at 16.2 mm were combined in the $(u, v)$ plane, yielding a point-source flux of $0.22 \pm 0.08$ mJy. The source was subsequently also detected at 7 mm with a point-source flux of $0.77 \pm 0.14$ mJy, and the source was not detected at 3 mm, down to a $3\sigma$ upper limit of 3.3 mJy. This implies a rather shallow mm slope ($\alpha \approx 1.5$), possibly indicating a large contribution from, e.g., free-free emission at 16 and maybe also 7 mm.

In addition, two large lobe-like features were detected about 4′ to the west of WW Cha at both 3.5 and 6.3 cm. These as yet unidentified radio sources are clearly seen in the 6 cm data, as shown in Fig. 5.5, which presents the combined 6.3 cm data from 18 October 2006 and 9 June 2007. The positions of

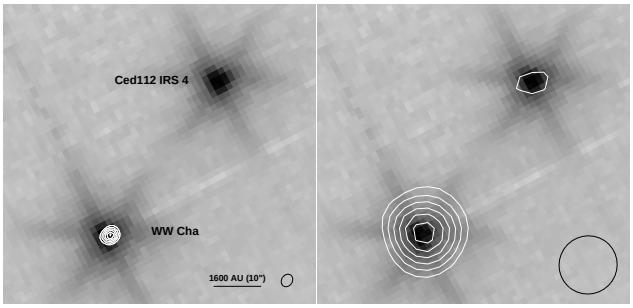


Figure 5.2: The contours show the emission towards WW Cha, observed at 3 mm (left) and 16 mm (right), overplotted on Spitzer Space Telescope InfraRed Array Camera observations at 3.6 $\mu$m (greyscale). Contours are 4, 6, 8, ... times the rms (2.0 mJy/beam at 3 mm and 0.07 mJy/beam at 16 mm) and the size of the synthesised beams at the respective wavelengths is plotted in the lower right corner. The observations at 16 mm (from combined data of 8 May 2006, 13 October 2006, and 31 March 2008) also show a 4$\sigma$ detection of the young stellar object Ced 112 IRS 4.

the sources are 11:08:43, -76:34:58 (J2000) (northern source) and 11:08:56, -76:36:24 (J2000) (southern source). The sources show up in both epochs at which WW Cha was observed at 6.3 cm, but they were not both positively detected at 3.5 cm in each epoch (see Table 5.4). Using the results from point-source fits in the $(u, v)$ plane, spectral slopes between 3.5 and 6.3 cm of $\alpha_{cm} < -2.7$ and $\alpha_{cm} = -3.0 \pm 0.2$ are found for the northern source and of $\alpha_{cm} = -2.54 \pm 0.19$ and $\alpha_{cm} < -2.3$ for the southern source, for 18 October 2006 and 9 June 2007 respectively. Recall that $\alpha$ is defined as $F_\nu \propto \nu^\alpha$, and a negative value implies a flux that increases towards longer wavelengths. Such steeply rising negative spectra are generally attributed to non-thermal emission. Neither of the two sources were detected at 16 mm. The sources may be background radio galaxies, though their fluxes are lower than the limiting magnitude of the 6 cm Parkes-MIT-NRAO radio continuum survey.

### 5.3.2 RU Lup

Table 5.5 summarises the fluxes of RU Lup on the different dates at the various wavelengths. The source RU Lup was observed at 3.3 mm with the ATCA on 24 August 2005 and reported to have a point-source flux of 12.7 mJy (Chapter 3). RU Lup was observed at 7 mm only once and clearly detected (see Fig. 5.6).

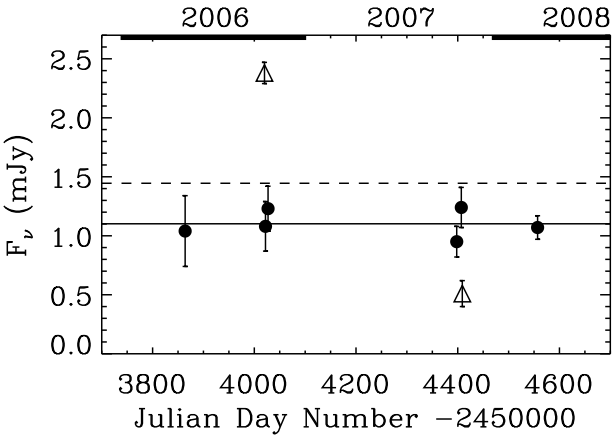


Figure 5.3: Point-source fits in the $(u, v)$ plane for WW Cha (dots) and RU Lup (triangles) at 16.2 mm. The solid line shows the mean value of $1.10 \pm 0.48$ mJy for WW Cha; the dashed line shows the mean value of $1.45 \pm 0.14$ mJy for RU Lup. The thick lines at the top correspond to the years 2006 and 2008, for reference. Note that the upper limit of 24 October 2007 is omitted to prevent this figure from becoming too cluttered; the variability of RU Lup at 16 mm is already clear from the two data points in the figure.

Point-source fluxes of $1.83 \pm 0.25$ mJy at 7.0 mm and of $1.52 \pm 0.24$ mJy at 7.3 mm were obtained. Though these values are consistent with each other, both wavelengths will be treated separately again, for consistency.

Three sets of observations were made of RU Lup at 16 mm. It was detected on 11 October 2006 (see Fig. 5.6), with point-source fluxes of $2.28 \pm 0.09$ and $2.38 \pm 0.09$ mJy at 16.1 and 16.2 mm respectively. It was not detected on 24 October 2007, with $3\sigma$ upper limits of 1.08 and 0.85 mJy at 15.4 and 16.2 mm. A flux of $0.51 \pm 0.11$ at 16.2 mm was detected on 4 November 2007, and a $3\sigma$ upper limit of 0.39 mJy at 15.4 mm, implying that the flux of RU Lup dropped by at least a factor of six over the course of a year. The data were checked for polarisation on 11 October 2007, when the emission was strongest. However, the emission was found to be unpolarised down to the noise level of our observations.

At 3.5 and 6.3 cm, RU Lup was observed on four different occasions (see Table 5.5). It was detected in most data sets, but the flux varied by up to a factor of two over the course of a year. Thus, RU Lup was detected at wavelengths ranging from 3.3 mm to 6.3 cm, with variable emission at 16 mm and longer

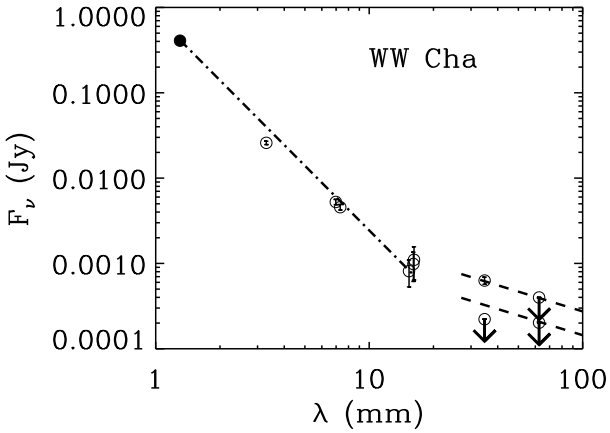


Figure 5.4: Long-wavelength SED of WW Cha. The 1.3 mm point is from Henning et al. (1993), the 3.3 mm point from Chapter 3, and the other points are from this work [point-source fits in the $(u, v)$ plane]. The dash-dotted line shows the fit to the mm data points from 1.3 through 16.2 mm with $\alpha = 2.52$. The dashed lines show $\alpha_{cm} = 0.77$ slopes to the cm data. Note that the emission at 3.5 cm is variable, whereas the emission at 16 mm is stable to well within the uncertainties, indicating that the emission mechanisms at these wavelengths are different.

wavelengths. The SED is given in Fig. 5.7.

### 5.3.3 CS Cha

Table 5.6 summarises the 7 mm fluxes of CS Cha on the different dates. CS Cha was previously observed at 3.3 mm with the ATCA on 26 August 2005 and detected with a point-source flux of 5.9 mJy (Chapter 3). The phases on 30 June 2008 were so unstable that the data could not be used in the analysis. The source was detected once at 7.3 mm, twice at 7.0 mm, and upper limits were determined at 6.7 mm. No proper map could be extracted from the data, in the case of 26 April 2008 because most of the baselines had to be flagged as bad and no closure could be reached, and in the case of 6 July 2008 because of the very elongated beam due to the short observing time. The analysis was done in the $(u, v)$ plane, and a point-source flux of $0.92 \pm 0.25$ mJy was found at 7.3 mm on 26 April 2008. An average 7.0 mm point-source flux of $1.19 \pm 0.27$ mJy (arithmetic mean of the fluxes and quadratic mean of the uncertainties) was determined from the two detections. None of the 7 mm-band detections were resolved. The SED of CS Cha

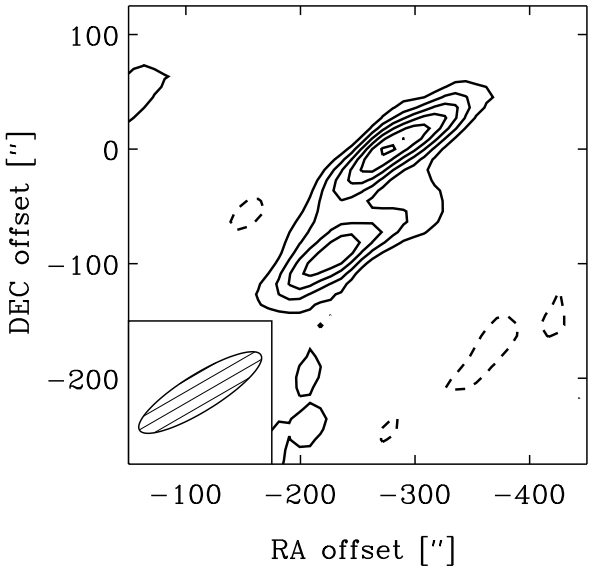


Figure 5.5: Image of the region 4 arcmin to the west of WW Cha at 6.3 cm. The offsets are with respect to the phase centre, which is at 11:10:04.0, -76:35:59.0 (J2000). Contours are at 2, 4, 6, 8, 10, 12 times the rms of 0.19 mJy/beam; negative contours are dashed.

is shown in Fig. 5.8.

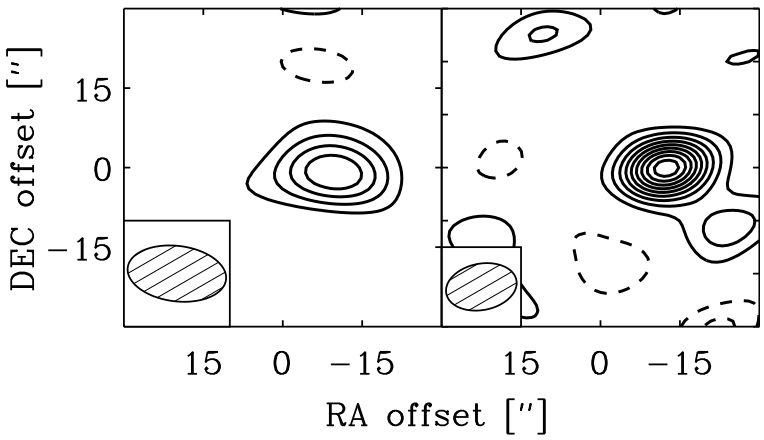


Figure 5.6: Image of RU Lup, observed at 7.3 mm on 6 October 2007 (*left panel*) and at 16.2 mm on 11 October 2006 (*right panel*). The offsets are with respect to the phase centre, which is located at 15:56:42.2, -37:49:15.5 (J2000). The contours are at 2, 4, 6, ... times the rms of 0.11 mJy/beam for both panels; negative contours are dashed. The peak emission corresponds to the position of the optically visible star. Note that the ($4\sigma$) peaks to the north-east and south-west of RU Lup at 16.2 mm are probably not real, as they are equally "significant" as the negative sidelobe in the lower right corner.

Table 5.3: Overview of the results for WW Cha.

| Obs. date | Wavelength (mm) | Flux[a] (mJy) | RMS[a] (mJy/beam) | Beam size[b] (arcsec) |
|---|---|---|---|---|
| ATCA 7 mm band | | | | |
| 5 Oct 2007 | 7.0 | $5.41 \pm 0.32$ | 0.313 | $11 \times 11$ |
| 5 Oct 2007 | 7.3 | $3.93 \pm 0.29$ | 0.350 | $11 \times 11$ |
| 31 Mar 2008 | 7.0 | $5.10 \pm 0.19$ | 0.231 | $5.8 \times 5.3$ |
| 31 Mar 2008 | 7.3 | $5.19 \pm 0.17$ | 0.194 | $6.1 \times 5.6$ |
| ATCA 12 mm band | | | | |
| 8 May 2006 | 16.1 | $1.16 \pm 0.31$ | 0.329 | $23 \times 6$ |
| 8 May 2006 | 16.2 | $1.04 \pm 0.30$ | 0.158 | $23 \times 6$ |
| 13 Oct 2006 | 16.1 | $< 0.921$ | 0.307 | $25 \times 9$ |
| 13 Oct 2006 | 16.2 | $1.08 \pm 0.21$ | 0.217 | $26 \times 9$ |
| 18 Oct 2006 | 16.1 | $0.81 \pm 0.20$ | 0.222 | $38 \times 7$ |
| 18 Oct 2006 | 16.2 | $1.23 \pm 0.19$ | 0.110 | $39 \times 7$ |
| 24 Oct 2007 | 15.4 | $1.01 \pm 0.16$ | 0.209 | $12 \times 8$ |
| 24 Oct 2007 | 16.2 | $0.95 \pm 0.13$ | 0.181 | $13 \times 9$ |
| 2 Nov 2007 | 15.4 | $0.55 \pm 0.20$[c] | 0.125 | $1.9 \times 1.3$ |
| 2 Nov 2007 | 16.2 | $0.48 \pm 0.13$[c] | 0.089 | $2.0 \times 1.4$ |
| 31 Mar 2008 | 15.4 | $0.88 \pm 0.12$ | 0.232 | $14 \times 13$ |
| 31 Mar 2008 | 16.2 | $1.07 \pm 0.10$ | 0.227 | $15 \times 13$ |
| ATCA 3 cm band | | | | |
| 18 Oct 2006 | 34.7 | $< 0.222$ | 0.074 | $71 \times 20$ |
| 9 June 2007 | 34.7 | $0.63 \pm 0.06$ | 0.076 | $53 \times 16$ |
| ATCA 6 cm band | | | | |
| 18 Oct 2006 | 62.5 | $< 0.202$ | 0.067 | $125 \times 32$ |
| 9 June 2007 | 62.5 | $< 0.399$ | 0.133 | $91 \times 26$ |

[a] Continuum fluxes are from point-source fits in the $(u, v)$ plane. If the source was not detected at $3\sigma$, a $3\sigma$ upper limit is quoted. RMS calculated from the cleaned image.

[b] Restored beam, using natural weighting. Note that the exact beam size depends on frequency and location of the source in the sky, as well as on the time of the observations, over which time range the data were taken, and exactly which data/baselines were included.

[c] The 16 mm values from the 2 November 2007 data were obtained with antenna 6 included, causing the significantly lower point-source flux. Note that a Gaussian fit recovers the full flux, indicating that the source is probably extended.

Table 5.4: Overview of the results for the two radio sources detected to the west of WW Cha in the 3 and 6 cm bands. Point source fluxes are given from both the northern and southern source.

| Obs. date | Wavelength (cm) | Flux[a] (mJy) | | RMS[b] (mJy/beam) | Beam size[c] (arcsec) |
|---|---|---|---|---|---|
| | | (northern) | (southern) | | |
| 18 October 2006 | 3.47 | $< 0.27$ | 0.29 | 0.09 | $71 \times 20$ |
| 9 June 2007 | 3.47 | 0.29 | $< 0.25$ | 0.08 | $53 \times 16$ |
| 18 October 2006 | 6.25 | 1.34 | 1.29 | 0.16 | $125 \times 32$ |
| 9 June 2007 | 6.25 | 1.71 | 0.99 | 0.14 | $91 \times 26$ |

[a] Continuum fluxes from point-source fits in the $(u, v)$ plane. $3\sigma$ upper limits are quoted in the case of non-detections.

[b] RMS calculated from the cleaned image.

[c] Restored beam, using natural weighting.

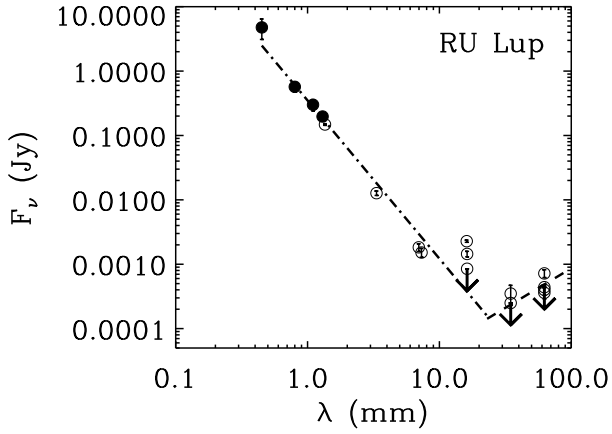


Figure 5.7: Long-wavelength SED of RU Lup. The dash-dotted line shows a fit to data from 450 $\mu$m through 7.3 mm of $\alpha = 2.46$, using data from Weintraub et al. (1989), Nürnberger et al. (1997), Chapter 3, and this work. The dashed line shows an $\alpha_{cm} = -1.23$ slope to the cm data. Multiple points are shown at 16 mm, 3.5 cm, and 6.3 cm, to indicate the source's variability at those wavelengths.

Table 5.5: Overview of the results for RU Lup.

| Obs. date | Wavelength (mm) | Flux[a] (mJy) | RMS[a] (mJy/beam) | Beam size[b] (arcsec) |
|---|---|---|---|---|
| ATCA 7 mm band | | | | |
| 6 October 2007 | 7.0 | $1.83 \pm 0.25$ | 0.490 | $18 \times 10$ |
| 6 October 2007 | 7.3 | $1.52 \pm 0.24$ | 0.141 | $19 \times 10$ |
| ATCA 12 mm band | | | | |
| 11 October 2006 | 16.1 | $2.28 \pm 0.09$ | 0.110 | $14 \times 9$ |
| 11 October 2006 | 16.2 | $2.38 \pm 0.09$ | 0.113 | $13 \times 9$ |
| 24 October 2007 | 15.4 | $< 1.08$ | 0.360 | $9.1 \times 7.8$ |
| 24 October 2007 | 16.2 | $< 0.85$ | 0.283 | $9.4 \times 8.1$ |
| 4 November 2007 | 15.4 | $< 0.39$ | 0.131 | $6.5 \times 1.5$ |
| 4 November 2007 | 16.2 | $0.51 \pm 0.11$ | 0.124 | $6.7 \times 1.6$ |
| ATCA 3 cm band | | | | |
| 12 October 2006 | 34.7 | $< 0.27$ | 0.089 | $27 \times 18$ |
| 13 October 2006 | 34.7 | $0.35 \pm 0.12$ | 0.098 | $23 \times 19$ |
| 9 June 2007 | 34.7 | $< 0.25$ | 0.082 | $53 \times 19$ |
| 4 November 2007 | 34.7 | $< 0.49$ | 0.164 | $56 \times 3$ |
| ATCA 6 cm band | | | | |
| 12 October 2006 | 62.5 | $0.36 \pm 0.07$ | 0.111 | $46 \times 34$ |
| 13 October 2006 | 62.5 | $0.72 \pm 0.10$ | 0.128 | $44 \times 33$ |
| 9 June 2007 | 62.5 | $0.40 \pm 0.07$ | 0.087 | $91 \times 31$ |
| 4 November 2007 | 62.5 | $< 0.44$ | 0.145 | $99 \times 6$ |

[a] Continuum fluxes are from point-source fits in the $(u, v)$ plane, where $3\sigma$ upper limits are quoted in the case of non-detections. RMS calculated from the cleaned image.

[b] Restored beam, using natural weighting. Note that the exact beam size depends on frequency and location of the source in the sky, as well as on the time of the observations, over which time range the data were taken, and exactly which data/baselines were included.

Table 5.6: Overview of the results for CS Cha.

| Obs. date | Wavelength (mm) | Flux[a] (mJy) | RMS[a] (mJy/beam) | Beam size[b] (arcsec) |
|---|---|---|---|---|
| 26 April 2008 | 7.0 | $1.00 \pm 0.28$ | 0.129 | $2.4 \times 1.4$ |
| 26 April 2008 | 7.3 | $0.92 \pm 0.25$ | 0.114 | $2.4 \times 1.5$ |
| 5 July 2008 | 6.7 | $< 0.82$ | 0.273 | $10.8 \times 0.6$ |
| 5 July 2008 | 7.0 | $< 0.71$ | 0.238 | $11.3 \times 0.6$ |
| 6 July 2008 | 6.7 | $< 1.11$ | 0.371 | $4.3 \times 0.6$ |
| 6 July 2008 | 7.0 | $1.38 \pm 0.26$ | 0.218 | $4.5 \times 0.6$ |

[a] Continuum fluxes are from point-source fits in the $(u, v)$ plane, where $3\sigma$ upper limits are quoted in the case of non-detections. RMS calculated from the cleaned image. CS Cha is located at 11:02:25.1, -77:33:35.95 (J2000).

[b] Restored beam, using natural weighting. Note that the exact beam size depends on frequency and location of the source in the sky, as well as on the time of the observations, over which time range the data were taken, and exactly which data/baselines were included.

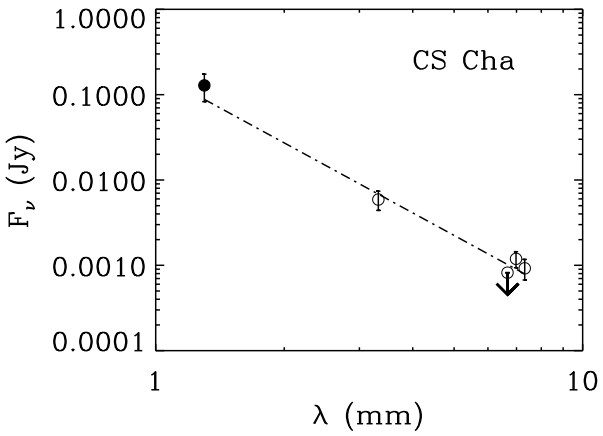


Figure 5.8: Millimetre SED of CS Cha. The 1.3 mm point is from Henning et al. (1993), the 3.3 mm point from Chapter 3, and the 7 mm points are from this work [point-source fits in the $(u, v)$ plane]. The dash-dotted line shows the fit to the mm data points of $\alpha = 2.9$.

## 5.4 Discussion and interpretation

The YSOs WW Cha, RU Lup, and CS Cha were observed at 7 mm using the ATCA. WW Cha and RU Lup were furthermore observed at 16 mm, 3.5 cm, and 6.3 cm. In this Section we discuss the implications of our observations and in particular we try to determine the source of the emission at cm wavelengths.

### 5.4.1 WW Cha

The SED of WW Cha (Fig. 5.4) shows a break in the slope at 16 mm. This suggests that the 16 mm flux is a continuation of the mm flux, implying that the emission up to that wavelength comes from thermal dust emission. The stability of the 16 mm flux over time scales of days, months, and years (see Fig. 5.3) supports the hypothesis that it is due to thermal emission from large, cool dust grains, and makes it unlikely that it is due to stellar magnetic activity, which is known to show variations up to an order of magnitude or more over timescales varying from months to years (e.g., Kutner et al. 1986; Chiang et al. 1996).

#### Disc emission

If the mm emission (from 3 to 16 mm) is due to dust, we should be able to resolve the emission (on the scale of the disc). To determine whether the source is resolved at any of these wavelengths, the method of Chapter 3 was followed. A circular Gaussian was fitted in the $(u, v)$ plane and if the Gaussian fitted flux is at least $2\sigma$ larger than the flux from a point-source fit, the source is concluded to be resolved at that wavelength. Using this definition, the 7 mm emission was found to be resolved on 31 March 2008 and the 16 mm emission was resolved on 2 November 2007 when WW Cha was observed with the 1.5A array configuration. Note that these two dates have the lowest RMS in their respective wave bands, as well as the smallest beam sizes. For details, see Table 5.7 (and note that the 2 November 2007 data include antenna 6). Fitting a circular Gaussian in the $(u, v)$ plane to the emission of WW Cha at 3 mm gives a flux of 33.1 mJy (Chapter 3) and yields a size of $1.5 \pm 0.2$ arcsec, corresponding to a physical (disc) size of $240 \pm 30$ AU at a distance of 160 pc (Whittet et al. 1997). A circular Gaussian fitted to the 7.0 mm emission in the $(u, v)$ plane gives a Gaussian flux of $5.79 \pm 0.38$ mJy and a corresponding source size of 2.0 arcsec, consistent with the size at 3 mm. Similarly, for the 15.4 mm emission a Gaussian flux of $1.65 \pm 0.55$ mJy and a corresponding source size of 2.1 arcsec are obtained, which is consistent with both the 3 and 7 mm sizes. See Table 5.7 for full details.

The peak brightness temperature of the emission is given by

$$T_b = \frac{F_\nu c^2}{2\nu^2 k}\frac{1}{\theta^2}, \tag{5.2}$$

where $k$ is Boltzmann's constant and $\theta^2$ the area of the emitting source. The 16.2 mm flux of $1.20 \pm 0.32$ mJy, (see Table 5.7, but now including a 15% uncertainty from the absolute flux calibration), implies a brightness temperature $T_b = 4.3 \pm 1.2$ K. The low brightness temperature rules out that the emission is thermal free-free from an ionised gas (e.g., Morgan et al. 1990; Snell & Bally 1986), unless (a) the emission has very low optical depth, or (b) it has a very low filling factor within the apparently resolved region (or a combination of these). Finally, a fit to the SED of WW Cha (Fig. 5.4) from 1.3 to 16.2 mm gives $\alpha = 2.52 \pm 0.12$. Given the stability of the 16 mm flux, the resolved size of the emission, the low peak brightness temperature, and the slope of the SED, we conclude that the emission at 16 mm is thermal emission from large grains or small "pebbles".

From our previous 3.3 mm observations, we determined the disc mass for WW Cha as 0.077 $M_\odot$ (Chapter 3). However, this mass determination assumed a dust opacity at 3.3 mm of $\kappa_\nu = 0.9$ cm$^2$ g$^{-1}$. Given the shallow slope of the SED in the mm regime for WW Cha, this value appears to be rather small. Indeed, if we take the mm slope $\alpha = 2.52 \pm 0.12$ and assume that the contribution of optically thick emission is negligible at these wavelengths, we find $\beta \approx \alpha - 2 = 0.52$. Using the opacity law of Beckwith et al. (1990)[3], $\kappa_\nu = 10(\nu/10^{12}\mathrm{Hz})^\beta$ cm$^2$ g$^{-1}$, this yields a dust opacity at 3.3 mm of $\kappa_\nu = 2.86$ cm$^2$ g$^{-1}$ and consequently a disc mass of $M_{\rm disc} = 0.024$ $M_\odot$, where we use

$$M_{\rm disc} = \frac{F_\nu \Psi D^2}{\kappa_\nu B_\nu(T_{\rm dust})}, \tag{5.3}$$

with $\Psi$ the gas-to-dust ratio (taken to be 100), $D$ the distance to the source, $\kappa_\nu$ the dust opacity, and $B_\nu(T_{\rm dust})$ the brightness at the frequency $\nu$ for a dust temperature $T_{\rm dust}$ (taken to be 25 K), as given by the Planck function. Disc masses in the range of 0.024 to 0.055 $M_\odot$ are found for our observations out to 16 mm using this opacity law (see Table 5.7). The spread in disc masses can in part be explained by the uncertainty in the values of the fluxes, and is also an indication that the opacity law is not entirely applicable to the case at hand. However, a disc mass of

[3]Note that Beckwith et al. (1990) estimate $\kappa_\nu = 0.1(\nu/10^{12}$ Hz$)^\beta$ cm$^2$ g$^{-1}$, where $\kappa_\nu$ is the opacity index *for the gas and the dust combined*, i.e., with an implied gas-to-dust ratio. Our values for $\kappa_\nu$, however, are for the dust alone, and hence we have to account for the gas-to-dust ratio explicitly in the calculation of the disc mass.

~0.03 $M_\odot$ for the system is probably accurate to within a factor of a few. Taking into account the contribution of optically thick emission, i.e., $\Delta \approx 0.2$ in Eq. 5.1 (Chapter 3), does not significantly change the results, giving disc masses in the range of 0.03 to 0.07 $M_\odot$. A more detailed determination of the disc mass requires radiative-transfer modelling of the system, including the full SED and available spatial information. For this, we refer the reader to an up coming paper (Ménard, et al., in prep.).

**Emission at longer wavelengths**

The slope of the 3.5 to 6.3 cm part of the SED gives $\alpha_{cm} > 0.77$, which suggests that the emission is thermal, perhaps from an optically thick, ionised wind (Panagia & Felli 1975; Wright & Barlow 1975; Olnon 1975). However, at 3.5 cm WW Cha appears to change in flux by a factor of three between the two epochs at which it was observed (18 October 2006 and 9 June 2007). This amount of variability makes optically thick wind emission an unlikely source for the cm emission. Indeed it is difficult to determine a spectral index in the cm, as the 3.5 cm flux clearly varies and only upper limits were obtained at 6.3 cm. Smith et al. (2003) found that for T Tau the cm spectral index can be positive even for non-thermal emission. They attribute the highly variable emission at 3.5 cm, along with a high level of polarisation and a very compact emission region, to an origin in a magnetically-dominated region close to the star. However, this is unlikely to be the cause of the emission at 3.5 cm for WW Cha, which we found to be unpolarised down to the noise level of our observations. Without information about the size of the emitting region, it is difficult to determine the nature of the cm emission in WW Cha. Follow-up observations should include very-long-baseline-array observations, which would resolve the system down to scales of several stellar radii, such as has been done for, e.g., the double binary T Tau (Smith et al. 2003) and for the binary system V773 Tauri A (Massi et al. 2008). We can conclude, however, that the emission at cm wavelengths is not dominated by thermal emission from large, cm-sized grains.

### 5.4.2 RU Lup

RU Lup was detected at 3.3, 7.0, and 7.3 mm. It was also detected at longer wavelengths, although not every time the source was observed. The SED shows a break around 16 mm (Fig. 5.7), indicating that the dominating emission mechnism changes, as was also observed for WW Cha.

### Disc emission

In Chapter 3 we found RU Lup to be resolved at 1.4 and 3.3 mm, with sizes of $1.02 \pm 0.32$ and $0.99 \pm 0.32''$ respectively, and a (sub)mm slope $\alpha = 2.5 \pm 0.1$ from 450 $\mu$m through 3.3 mm, indicating that the mm emission is due to grains of at least mm sizes. Adding the data points at 7.0 and 7.3 mm to the SED of RU Lup (see Fig. 5.7), a slope of $\alpha = 2.46 \pm 0.09$ from 450 $\mu$m through 7.3 mm is found, indicating that the emission at 7 mm is still due to dust. Fitting a circular Gaussian in the $(u, v)$ plane gives a Gaussian flux of $1.64 \pm 0.39$ and $2.33 \pm 0.39$ mJy at 7.0 and 7.3 mm respectively. This suggests that the 7.3 mm data are resolved (since $F_{\rm Gauss} > F_{\rm point} + 2\sigma$) with a Gaussian size of $9.3''$, which is about 1300 AU at 140 pc. This is quite large, suggesting an extended envelope rather than a disc. This Gaussian size gives a very low peak brightness temperature ($< 0.1$ K). However, the evidence for extended emission is borderline, with the 7.0 mm flux failing our "resolved" test $F_{\rm Gauss} > F_{\rm point} + 2\sigma$ and the 7.3 mm emission only just meeting this criterion.

In Chapter 3 we estimated the disc in the system to be 0.032 $M_\odot$ in mass, assuming an opacity at 3.3 mm of 0.9 cm$^2$ g$^{-1}$. Again neglecting the contribution from optically thick emission, an opacity index $\beta \approx \alpha - 2 = 0.46$ is found. Using the opacity law of Beckwith et al. (1990), this implies an opacity of 3.30, 2.35, and 2.30 cm$^2$ g$^{-1}$ at 3.3, 7.0, and 7.3 mm, respectively. This in turn yields a disc mass of 0.010, 0.006, and 0.010 $M_\odot$ for the different wavelengths, where the spread is most likely dominated by the uncertainty in the fluxes. Again, we refer the reader to an upcoming paper (Ménard, et al., in prep.) for a more detailed calculation of the disc mass.

### Emission at longer wavelengths

RU Lup was detected twice at 16 mm, with a $3\sigma$ upper limit found from a third observation. The fluxes from the three different data sets are inconsistent with each other (see Fig. 5.3), ruling out thermal emission from large grains at these wavelengths. The centimetre slope of the SED from 3.5 to 6.3 cm is $\alpha_{cm} = -1.23 \pm 0.17$ (taken from the detections on 13 October 2006), which, in contrast to WW Cha, implies non-thermal emission from optically thin gyrosynchrotron emission (Anglada et al. 1998; Forbrich et al. 2006), though the variability of the emission makes it difficult to fit one consistent slope to the data. The 16 mm flux is surprisingly high (see Fig. 5.7) and appears to result from more than just thermal emission from dust grains. One possible explanation for the excess 16 mm flux and its variability is that some of the emission comes from a cyclotron maser

(Dulk 1985). The data from 11 October 2006, when the 16 mm flux was highest, have negligible Stokes $Q$, $U$, and $V$ fluxes and hence the emission was unpolarised. Furthermore, maser cyclotrons are expected to produce emission at and around the cyclotron frequency alone. This could result in the emission only being significantly stronger in one of the two sidebands, which is not observed. The lack of polarisation and strongly coherent emission seems to suggest that the emission is not due to a cyclotron maser. However, the overall frequency range of maser emission from a source could be larger than just directly around the cyclotron frequency, and the intrinsic polarisation is likely to be destroyed by Faraday rotation in the overlying plasma (Dulk 1985). Therefore, cyclotron maser emission cannot be fully ruled out. Information on different, even shorter timescales of the radio emission may shed additional light on the processes at play, and the increased sensitivity of the ATCA with the recent addition of the Compact Array Broadband Backend can be a useful tool in this. Unfortunately, RU Lup was never observed at 16 mm, 3.5 cm and 6.3 cm on the same day and we know that the 3.5 cm varies by a factor of two within 24 hours. It seems likely that there are three different emission mechanisms – disc+star+wind – acting over these three cm wavelength bands. This is different from WW Cha, where dust emission dominates up to 16 mm. To determine of the emission mechanism at longer wavelengths requires the source to be resolved, which needs very-long-baseline-interferometer observations.

### 5.4.3 CS Cha

During the three months over which CS Cha was observed, the 7 mm emission was relatively stable and a mm slope $\alpha = 2.90 \pm 0.26$ from 1.3 to 7.3 mm was found. This is consistent with the SED slope found from 1.3 to 3.3 mm in Chapter 3 ($\alpha = 2.9 \pm 0.5$). Since neither the 3 or 7 mm emission was resolved, it cannot be ruled out that the mm emission is optically thick. However, if we assume the emission to be completely optically thin, $\alpha = 2.90$ implies a dust opacity index $\beta = 0.90$. This would suggest that the 7 mm emission from CS Cha is also predominantly due to thermal dust emission from mm-sized grains.

The disc mass was estimated in Chapter 3 to be 0.021 $M_\odot$. Taking the opacity law of Beckwith et al. (1990) and an opacity index $\beta = 0.90$, a mass of 0.016, 0.018, 0.016 $M_\odot$ is found at the different wavelengths, which is consistent with the value of Chapter 3 given the uncertainties in the fluxes. Espaillat et al. (2007) found a disc mass of 0.04 $M_\odot$ through more detailed modelling, slightly larger than the value found with a simple opacity law.

### 5.4.4 Large grains in protoplanetary discs

The mm slopes of WW Cha, RU Lup and CS Cha are given by $\alpha = 2.52 \pm 0.12, 2.46 \pm 0.09$, and $2.90 \pm 0.26$ respectively. This suggests that all three sources have grains of at least mm sizes, although it should be noted that the 7 mm emission of CS Cha was not resolved, and hence the emission could be optically thick. This suggests that grains grow from sub-micron sizes to at least mm sizes throughout the bulk of the disc within a few hundred thousand years. To date only one T-Tauri star has been found with large, cm-sized grains – TW Hya. This was the only other source that has been monitored at cm wavelengths for long periods of time and was found to have stable thermal dust emission at 3.5 cm. But is TW Hya unique? Our new 16 mm results show that the disc of WW Cha also contains cm-sized grains (and we have similar results for the Herbig-Ae star HD 100546; Wright et al., in prep.). Furthermore, about 10% of the 16 mm emission from RU Lup is likely to derive from pebbles as well, so it would appear that cm-sized grains in protoplanetary discs are not as rare as might have been expected.

It has been a long-standing problem in planet formation theory that boulders of about a metre in size fall into the central star before accumulating and growing to kilometre-sized planetesimals (Weidenschilling 1977). Recent numerical simulations have shown that this so-called "metre-size barrier" can be overcome. For example, Johansen et al. (2007) find that grain growth via gravitational collapse can be very efficient in the mid-plane of turbulent discs where streaming instabilities help concentrate grains that grow to several 100 km in a few thousand years. Lyra et al. (2008b) show that grains trapped in Rossby waves excited at the edge of dead zones can grow to Mars-sized embryos in a few thousand years. Brauer et al. (2008b) also find that grains grow rapidly in the near-laminar dead zone of discs and that the associated pressure maxima near evaporation fronts ensure that the newly formed boulders do not migrate radially. These simulations all start with grains that are already at least cm-sized. Our results demonstrate that this is reasonable, and thus with seeds of this size the metre-sized barrier can be overcome to produce fully-fledged protoplanets.

Ideally one would like to know the timescales of grain growth and so may be tempted to try to find an evolutionary sequence of grain size with age. For example, RU Lup and WW Cha are both about 0.5 Myr and show grain sizes up to about a cm, while TW Hya is 9 Myr and shows grains up to 3.5 cm. However, it should be noted that ages of T-Tauri stars are notoriously difficult to determine, but more importantly, the data tell us that other, possibly different, emission mechanisms

are stronger for WW Cha and RU Lup than for TW Hya – which may be age-related. Clearly, a much larger sample is needed to draw any significant con-

clusions regarding grain growth up to pebble or even boulder sizes.

## 5.5 Conclusions

We have been monitoring the mm and cm emission of two T-Tauri stars, WW Cha and RU Lup, over the course of several years with the ATCA, and more recently performed 7 mm observations of the third young T-Tauri star CS Cha. We find that emission up to 7 mm for all three sources is well explained by thermal dust emission from mm-sized grains. The stability of the 16 mm flux in WW Cha, along with the low peak brightness temperature at this wavelength, indicates that this emission is dominated by even larger, cm-size "pebbles", making it the second protoplanetary disc known to contain such large grains. The 16 mm emission of RU Lup may also include dust emission from pebbles, but other emission mechanisms appear to dominate at this wavelength.

This work underlines the necessity to observe young stellar objects at multiple wavelengths and to monitor them over extended periods of time, in order to disentangle the various candidate emission mechanisms at mm and cm wavelengths. The ATCA is well suited to do this and with the upgrade of the correlator that is currently underway, increasing the bandwidth of the telescope by a factor of 16, extended surveys of southern protoplanetary discs will soon be within reach. This will allow us to put more stringent constraints on the processes involved in the first steps of planet formation, telling us where and when they take place.

**Acknowledgements**
DL acknowledges Swinburne University and UNSW@ADFA for their hospitality. This work was partially supported by a Netherlands Research School For Astronomy network 2 grant and a Netherlands Organisation for Scientific Research Spinoza grant (DL and EFvD), a Swinburne Researcher Development Scheme, a Swinburne Special Studies Program, and the Programme National de Physique Stellaire (PNPS), INSU/CNRS (STM), and by an ARC Australian Research Fellowship (CMW). We would like to thank the ATNF staff at Narrabri for their hospitality and assistance, and Annie Hughes and Steve Longmore for assisting with some of the observations. We also thank François Ménard for useful discussions, and we are indepted to the anonymous referee, whose comments helped to considerably improve this paper. This research has made use of the SIMBAD database, operated at CDS, Strasbourg, France.

Table 5.7: Resolving WW Cha. Point-source versus Gaussian fluxes and resulting Gaussian source size for WW Cha at 7 and 16 mm.

| Obs. date | $\lambda_{\rm eff}$ (mm) | Flux (p)[a] (mJy) | Flux (G)[a] (mJy) | RMS[b] (mJy/bm) | Gaussian size (arcsec) | Beam[c] (arcsec) | Opacity[d] ($\rm cm^2\ g^{-1}$) | $M_{\rm disc}$[e] ($\rm M_\odot$) |
|---|---|---|---|---|---|---|---|---|
| 24-28 August 2005[f] | 3.3 | $25.9 \pm 1.0$ | $33.1 \pm 2.1$ | 1.2 | 1.32 | $2.5 \times 2.2$ | 2.86 | 0.024 |
| 31 March 2008 | 7.0 | $5.1 \pm 0.19$ | $5.79 \pm 0.38$ | 0.231 | 2.0 | $5.8 \times 5.3$ | 1.94 | 0.027 |
| 31 March 2008 | 7.3 | $5.2 \pm 0.17$ | $6.46 \pm 0.38$ | 0.194 | 3.4 | $6.1 \times 5.6$ | 1.90 | 0.033 |
| 2 November 2007 | 15.4 | $0.55 \pm 0.20$ | $1.65 \pm 0.55$ | 0.125 | 2.1 | $1.9 \times 1.3$ | 1.29 | 0.055 |
| 2 November 2007 | 16.2 | $0.48 \pm 0.12$ | $1.20 \pm 0.26$ | 0.089 | 1.2 | $2.0 \times 1.4$ | 1.26 | 0.045 |

[a] Continuum fluxes are from point-source (p) and circular Gaussian (G) fits in the $(u, v)$ plane.

[b] RMS calculated from the cleaned image.

[c] Size of the restored beam, using natural weighting.

[d] Dust opacity, using the opacity law of Beckwith et al. (1990) $\kappa_\nu = 10\ (\nu/10^{12}\ \rm Hz)^\beta$, with $\beta = 0.52$.

[e] Assuming a gas-to-dust ratio of 100.

[f] From Chapter 3.

# References

Acke, B. & van den Ancker, M. E. 2004, A&A, 426, 151
Acke, B., van den Ancker, M. E., Dullemond, C. P., van Boekel, R., & Waters, L. B. F. M. 2004, A&A, 422, 621
Alcala, J. M., Krautter, J., Schmitt, J. H. M. M., et al. 1995, A&AS, 114, 109
Alonso-Albi, T., Fuente, A., Bachiller, R., et al. 2008, ApJ, 680, 1289
André, P. & Montmerle, T. 1994, ApJ, 420, 837
André, P., Montmerle, T., Feigelson, E. D., Stine, P. C., & Klein, K.-L. 1988, ApJ, 335, 940
André, P., Ward-Thompson, D., & Barsony, M. 1993, ApJ, 406, 122
Andrews, S. M. & Williams, J. P. 2005, ApJ, 631, 1134
Andrews, S. M. & Williams, J. P. 2007, ApJ, 659, 705
Anglada, G., Villuendas, E., Estalella, R., et al. 1998, AJ, 116, 2953
Bailes, M., Lyne, A. G., & Shemar, S. L. 1991, Nature, 352, 311
Bally, J., Walawender, J., Luhman, K. L., & Fazio, G. 2006, AJ, 132, 1923
Beckwith, S. V. W. & Sargent, A. I. 1991, ApJ, 381, 250
Beckwith, S. V. W., Sargent, A. I., Chini, R. S., & Guesten, R. 1990, AJ, 99, 924
Benson, P. J. & Myers, P. C. 1989, ApJS, 71, 89
Bertout, C., Robichon, N., & Arenou, F. 1999, A&A, 352, 574
Binzel, R. P. 2006, Minor Planet Bulletin, 33, 106
Bjorkman, J. E. & Wood, K. 2001, ApJ, 554, 615
Blum, J. 2004, in Astronomical Society of the Pacific Conference Series, Vol. 309, Astrophysics of Dust, ed. A. N. Witt, G. C. Clayton, & B. T. Draine, 369–5000
Blum, J. & Wurm, G. 2000, Icarus, 143, 138
Blum, J. & Wurm, G. 2008, ARA&A, 46, 21
Boogert, A. C. A., Hogerheijde, M. R., Ceccarelli, C., et al. 2002, ApJ, 570, 708
Boss, A. P. 1997, Science, 276, 1836
Bouwman, J., Meeus, G., de Koter, A., et al. 2001, A&A, 375, 950
Brandt, J. C., Stecher, T. P., Crawford, D. L., & Maran, S. P. 1971, ApJ, 163, L99
Brauer, F., Dullemond, C. P., & Henning, T. 2008a, A&A, 480, 859
Brauer, F., Henning, T., & Dullemond, C. P. 2008b, A&A, 487, L1
Brown, J. M., Blake, G. A., Dullemond, C. P., et al. 2007, ApJ, 664, L107
Bruno, G. 1584, On the Infinite Universe and Worlds, 1980th edn. (The Quest for Extraterrestrial Life)
Calvet, N., D'Alessio, P., Hartmann, L., et al. 2002, ApJ, 568, 1008

Cameron, A. G. W. 1978, in IAU Colloq. 52: Protostars and Planets, ed. T. Gehrels, 453

Carpenter, J. M., Wolf, S., Schreyer, K., Launhardt, R., & Henning, T. 2005, AJ, 129, 1049

Chandler, C. J. & Richer, J. S. 2000, ApJ, 530, 851

Chen, H., Grenfell, T. G., Myers, P. C., & Hughes, J. D. 1997, ApJ, 478, 295

Chiang, E., Phillips, R. B., & Lonsdale, C. J. 1996, AJ, 111, 355

Chiang, E. I. & Goldreich, P. 1997, ApJ, 490, 368

Chiang, E. I. & Goldreich, P. 1999, ApJ, 519, 279

Chini, R., Kämpgen, K., Reipurth, B., et al. 2003, A&A, 409, 235

Ciardi, D. R., Telesco, C. M., Packham, C., et al. 2005, ApJ, 629, 897

Comerón, F. 2008, in 'Handbook of star forming regions', ed. B. Reipurth, ASP Conf. Ser., in press (ESO press)

Comerón, F., Fernández, M., Baraffe, I., Neuhäuser, R., & Kaas, A. A. 2003, A&A, 406, 1001

Comerón, F., Rieke, G. H., & Neuhäuser, R. 1999, A&A, 343, 477

Correia, S., Zinnecker, H., Ratzka, T., & Sterzik, M. F. 2006, A&A, 459, 909

Crapsi, A., Caselli, P., Walmsley, M. C., & Tafalla, M. 2007, A&A, 470, 221

Crapsi, A., van Dishoeck, E. F., Hogerheijde, M. R., Pontoppidan, K. M., & Dullemond, C. P. 2008, A&A, 486, 245

D'Alessio, P., Calvet, N., Hartmann, L., Franco-Hernández, R., & Servín, H. 2006, ApJ, 638, 314

D'Antona, F. & Mazzitelli, I. 1997, Memorie della Societa Astronomica Italiana, 68, 807

de Geus, E. J., de Zeeuw, P. T., & Lub, J. 1989, A&A, 216, 44

de Zeeuw, P. T., Hoogerwerf, R., de Bruijne, J. H. J., Brown, A. G. A., & Blaauw, A. 1999, AJ, 117, 354

Dohnanyi, J. W. 1969, J. Geophys. Res., 74, 2531

Dominik, C., Blum, J., Cuzzi, J. N., & Wurm, G. 2006, in Proceedings of PPV, B. Reipurth, D. Jewitt, and K. Keil eds., astro-ph/0602617 (the University of Arizona Press)

Dominik, C. & Dullemond, C. P. 2008, A&A, 491, 663

Dominik, C. & Tielens, A. G. G. M. 1997, ApJ, 480, 647

Draine, B. T. 2006, ApJ, 636, 1114

Dulk, G. A. 1985, ARA&A, 23, 169

Dullemond, C. P. 2002, A&A, 395, 853

Dullemond, C. P. & Dominik, C. 2004a, A&A, 417, 159
Dullemond, C. P. & Dominik, C. 2004b, A&A, 421, 1075
Dullemond, C. P. & Dominik, C. 2005, A&A, 434, 971
Dullemond, C. P. & Dominik, C. 2008, A&A, 487, 205
Dullemond, C. P., Dominik, C., & Natta, A. 2001, ApJ, 560, 957
Epicurus. 300 B.C., in "Lettres et Maximes", 1992nd edn. ("Presses Universitaires de France, Paris"), 105
Espaillat, C., Calvet, N., D'Alessio, P., et al. 2007, ApJ, 664, L111
Evans, N. J., Allen, L. E., Blake, G. A., et al. 2003, PASP, 115, 965
Evans, II, N. J., Harvey, P. M., Dunham, M. M., et al. 2007, Delivery of Data from the c2d Legacy Project: IRAC and MIPS (Pasadena, SSC)
Flaherty, K. M., Pipher, J. L., Megeath, S. T., et al. 2007, ApJ, 663, 1069
Forbrich, J., Massi, M., Ros, E., Brunthaler, A., & Menten, K. M. 2007, A&A, 469, 985
Forbrich, J., Preibisch, T., & Menten, K. M. 2006, A&A, 446, 155
Furlan, E., Hartmann, L., Calvet, N., et al. 2006, ApJS, 165, 568
Gauvin, L. S. & Strom, K. M. 1992, ApJ, 385, 217
Girart, J. M., Curiel, S., Rodríguez, L. F., et al. 2004, AJ, 127, 2969
Glindemann, A., Abuter, R., Carbognani, F., et al. 2000, in Society of Photo-Optical Instrumentation Engineers (SPIE) Conference Series, Vol. 4006, ed. P. Léna & A. Quirrenbach, 2–12
Goldreich, P. & Ward, W. R. 1973, ApJ, 183, 1051
Gómez, M., Persi, P., Marenzi, A. R., Roth, M., & Tapia, M. 2004, A&A, 423, 629
Greene, T. P., Wilking, B. A., Andre, P., Young, E. T., & Lada, C. J. 1994, ApJ, 434, 614
Guenther, E. W., Esposito, M., Mundt, R., et al. 2007, A&A, 467, 1147
Guilloteau, S., Dutrey, A., Pety, J., & Gueth, F. 2008, A&A, 478, L31
Gürtler, J., Schreyer, K., Henning, T., Lemke, D., & Pfau, W. 1999, A&A, 346, 205
Haisch, Jr., K. E., Barsony, M., Greene, T. P., & Ressler, M. E. 2002, AJ, 124, 2841
Haisch, Jr., K. E., Lada, E. A., & Lada, C. J. 2001, ApJ, 553, L153
Harvey, D. W. A., Wilner, D. J., Myers, P. C., & Tafalla, M. 2003, ApJ, 596, 383
Hatchell, J., Fuller, G. A., Richer, J. S., Harries, T. J., & Ladd, E. F. 2007, A&A, 468, 1009

Hayashi, C., Nakazawa, K., & Nakagawa, Y. 1985, in Protostars and Planets II, ed. D. C. Black & M. S. Matthews, 1100–1153
Heiles, C. 1998, ApJ, 498, 689
Henning, T., Launhardt, R., Steinacker, J., & Thamm, E. 1994, A&A, 291, 546
Henning, T., Pfau, W., Zinnecker, H., & Prusti, T. 1993, A&A, 276, 129
Herbig, G. H. & Kameswara Rao, N. 1972, ApJ, 174, 401
Herczeg, G. J., Walter, F. M., Linsky, J. L., et al. 2005, AJ, 129, 2777
Hildebrand, R. H. 1983, QJRAS, 24, 267
Ho, P. T. P., Moran, J. M., & Lo, K. Y. 2004, ApJ, 616, L1
Hogerheijde, M. R. & van der Tak, F. F. S. 2000, A&A, 362, 697
Hogerheijde, M. R., van Dishoeck, E. F., Blake, G. A., & van Langevelde, H. J. 1997, ApJ, 489, 293
Hogerheijde, M. R., van Dishoeck, E. F., Blake, G. A., & van Langevelde, H. J. 1998, ApJ, 502, 315
Hueso, R. & Guillot, T. 2005, A&A, 442, 703
Hughes, J., Hartigan, P., & Clampitt, L. 1993, AJ, 105, 571
Hughes, J., Hartigan, P., Krautter, J., & Kelemen, J. 1994, AJ, 108, 1071
James, D. J., Melo, C., Santos, N. C., & Bouvier, J. 2006, A&A, 446, 971
Johansen, A., Oishi, J. S., Low, M.-M. M., et al. 2007, Nature, 448, 1022
Johnstone, D., Di Francesco, J., & Kirk, H. 2004, ApJ, 611, L45
Jørgensen, J. K., Bourke, T. L., Myers, P. C., et al. 2007, ApJ, 659, 479
Jørgensen, J. K., Bourke, T. L., Myers, P. C., et al. 2005, ApJ, 632, 973
Jørgensen, J. K., Hogerheijde, M. R., van Dishoeck, E. F., Blake, G. A., & Schöier, F. L. 2004, A&A, 413, 993
Jørgensen, J. K., Schöier, F. L., & van Dishoeck, E. F. 2002, A&A, 389, 908
Kenyon, S. J., Gomez, M., Marzke, R. O., & Hartmann, L. 1994, AJ, 108, 251
Kenyon, S. J., Gómez, M., & Whitney, B. A. 2008, Low Mass Star Formation in the Taurus-Auriga Clouds (Handbook for Star Forming Regions, Volume I: The Northern Sky ASP Monograph Publications, Vol. 4. Edited by Bo Reipurth, p.405), 405
Kessler-Silacci, J., Augereau, J.-C., Dullemond, C. P., et al. 2006, ApJ, 639, 275
Kessler-Silacci, J. E., Dullemond, C. P., Augereau, J.-C., et al. 2007, ApJ, 659, 680
Klessen, R. S., Heitsch, F., & Mac Low, M.-M. 2000, ApJ, 535, 887
Kuiper, G. P. 1951, Proceedings of the National Academy of Science, 37, 383
Kutner, M. L., Rydgren, A. E., & Vrba, F. J. 1986, AJ, 92, 895

Lada, C. J. 1987, in IAU Symp. 115: Star Forming Regions, ed. M. Peimbert & J. Jugaku, 1–17

Lada, C. J. & Wilking, B. A. 1984, ApJ, 287, 610

Lahuis, F., Kessler-Silacci, J. E., Evans, N. J., et al. 2006, c2d Spectroscopy Explanatory Suppl. (Pasadena: *Spitzer* Science Center)

Lamzin, S. A., Bisnovatyi-Kogan, G. S., Errico, L., et al. 1996, A&A, 306, 877

Lawson, W. A., Feigelson, E. D., & Huenemoerder, D. P. 1996, MNRAS, 280, 1071

Leinert, C., Graser, U., Waters, L. B. F. M., et al. 2003, in Society of Photo-Optical Instrumentation Engineers (SPIE) Conference Series, Vol. 4838, ed. W. A. Traub, 893–904

Looney, L. W., Mundy, L. G., & Welch, W. J. 2000, ApJ, 529, 477

Luhman, K. L. 2007, ApJS, 173, 104

Lyra, W., Johansen, A., Klahr, H., & Piskunov, N. 2008a, A&A, 491, L41

Lyra, W., Johansen, A., Klahr, H., & Piskunov, N. 2008b, ArXiv e-prints, 807

Malfait, K., Waelkens, C., Waters, L. B. F. M., et al. 1998, A&A, 332, L25

Massi, F., de Luca, M., Elia, D., et al. 2007, A&A, 466, 1013

Massi, F., Giannini, T., Lorenzetti, D., et al. 1999, A&AS, 136, 471

Massi, M., Forbrich, J., Menten, K. M., et al. 2006, A&A, 453, 959

Massi, M., Ros, E., Menten, K. M., et al. 2008, A&A, 480, 489

Mathis, J. S., Rumpl, W., & Nordsieck, K. H. 1977, ApJ, 217, 425

Matsuo, T., Shibai, H., Ootsubo, T., & Tamura, M. 2007, ApJ, 662, 1282

Mayor, M. & Queloz, D. 1995, Nature, 378, 355

Meeus, G., Sterzik, M., Bouwman, J., & Natta, A. 2003, A&A, 409, L25

Meeus, G., Waters, L. B. F. M., Bouwman, J., et al. 2001, A&A, 365, 476

Merín, B., Jørgensen, J., Spezzi, L., et al. 2008, ApJS, 177, 551

Min, M., Hovenier, J. W., & de Koter, A. 2003, A&A, 404, 35

Morgan, J. A., Snell, R. L., & Strom, K. M. 1990, ApJ, 362, 274

Mouschovias, T. C. 1977, ApJ, 211, 147

Natta, A., Grinin, V., & Mannings, V. 2000, Protostars and Planets IV, 559

Natta, A., Prusti, T., Neri, R., et al. 2001, A&A, 371, 186

Natta, A., Testi, L., Calvet, N., et al. 2007, in Protostars and Planets V, ed. B. Reipurth, D. Jewitt, & K. Keil, 767–781

Natta, A., Testi, L., Neri, R., Shepherd, D. S., & Wilner, D. J. 2004, A&A, 416, 179

Neuhäuser, R. & Forbrich, J. 2008, The Corona Australis Star Forming Re-

gion (Handbook for Star Forming Regions, Volume II: The Southern Sky ASP Monograph Publications, Vol. 5. Edited by Bo Reipurth, p.735), 735
Nomura, H. & Nakagawa, Y. 2006, ApJ, 640, 1099
Nürnberger, D., Chini, R., & Zinnecker, H. 1997, A&A, 324, 1036
Ohashi, N., Hayashi, M., Ho, P. T. P., & Momose, M. 1997, ApJ, 475, 211
Oliveira, I., Merín, B., Pontoppidan, K. M., et al. 2009, ApJ, 691, 672
Olnon, F. M. 1975, A&A, 39, 217
Ossenkopf, V. & Henning, T. 1994, A&A, 291, 943
Palla, F. & Stahler, S. W. 1993, ApJ, 418, 414
Panagia, N. & Felli, M. 1975, A&A, 39, 1
Paszun, D. & Dominik, C. 2006, Icarus, 182, 274
Pinte, C., Padgett, D. L., Ménard, F., et al. 2008, A&A, 489, 633
Podio, L., Garcia, P. J. V., & Bacciotti, F. 2007, Memorie della Societa Astronomica Italiana, 78, 693
Pollack, J. B., Hubickyj, O., Bodenheimer, P., et al. 1996, Icarus, 124, 62
Pontoppidan, K. M., Blake, G. A., van Dishoeck, E. F., et al. 2008, ApJ, 684, 1323
Pontoppidan, K. M., Fraser, H. J., Dartois, E., et al. 2003, A&A, 408, 981
Przygodda, F., van Boekel, R., Àbrahàm, P., et al. 2003, A&A, 412, L43
Qi, C. 2005, The MIR Cookbook, The Submillimeter Array / Harvard-Smithsonian Center for Astrophysics (http://cfa-www.harvard.edu/ cqi/mircook.html)
Reipurth, B., Nyman, L.-A., & Chini, R. 1996, A&A, 314, 258
Ridge, N. A., Di Francesco, J., Kirk, H., et al. 2006, AJ, 131, 2921
Robitaille, T. P., Whitney, B. A., Indebetouw, R., Wood, K., & Denzmore, P. 2006, ApJS, 167, 256
Robrade, J. & Schmitt, J. H. M. M. 2007, A&A, 473, 229
Rodmann, J., Henning, T., Chandler, C. J., Mundy, L. G., & Wilner, D. J. 2006, A&A, 446, 211
Safronov, V. S. & Zvjagina, E. V. 1969, Icarus, 10, 109
Sault, R. J., Teuben, P. J., & Wright, M. C. H. 1995, in ASP Conf. Ser. 77: Astronomical Data Analysis Software and Systems IV, 433
Sekiya, M. & Takeda, H. 2003, Earth, Planets, and Space, 55, 263
Setiawan, J., Henning, T., Launhardt, R., et al. 2008, Nature, 451, 38
Shirley, Y. L., Evans, II, N. J., & Rawlings, J. M. C. 2002, ApJ, 575, 337
Shu, F. H. 1977, ApJ, 214, 488
Shu, F. H., Adams, F. C., & Lizano, S. 1987, ARA&A, 25, 23

Smith, K., Pestalozzi, M., Güdel, M., Conway, J., & Benz, A. O. 2003, A&A, 406, 957
Snell, R. L. & Bally, J. 1986, ApJ, 303, 683
Stempels, H. C. & Piskunov, N. 2002, A&A, 391, 595
Straižys, V., Černis, K., & Bartašiūte˙, S. 1996, Baltic Astronomy, 5, 125
Tanaka, H., Himeno, Y., & Ida, S. 2005, ApJ, 625, 414
Terebey, S., Shu, F. H., & Cassen, P. 1984, ApJ, 286, 529
Testi, L., Natta, A., Shepherd, D. S., & Wilner, D. J. 2001, ApJ, 554, 1087
Ulrich, R. K. 1976, ApJ, 210, 377
van Boekel, R. 2008, Journal of Physics Conference Series, 131, 012023
van Boekel, R., Min, M., Leinert, C., et al. 2004, Nature, 432, 479
van Boekel, R., Min, M., Waters, L. B. F. M., et al. 2005, A&A, 437, 189
van Boekel, R., Waters, L. B. F. M., Dominik, C., et al. 2003, A&A, 400, L21
van den Ancker, M. E., de Winter, D., & Tjin A Djie, H. R. E. 1998, A&A, 330, 145
van Kempen, T. A., van Dishoeck, E. F., Brinch, C., & Hogerheijde, M. R. 2007, A&A, 461, 983
van Kempen, T. A., van Dishoeck, E. F., Salter, D. M., et al. 2009, A&A accepted
Voshchinnikov, N. V. & Henning, T. 2008, A&A, 483, L9
Wang, H. & Henning, T. 2006, ApJ, 643, 985
Weidenschilling, S. J. 1977, Ap&SS, 51, 153
Weidenschilling, S. J. 1980, Icarus, 44, 172
Weidenschilling, S. J. 1988, Formation processes and time scales for meteorite parent bodies (Meteorites and the Early Solar System), 348–371
Weidenschilling, S. J. 1997, Icarus, 127, 290
Weintraub, D. A., Sandell, G., & Duncan, W. D. 1989, ApJ, 340, L69
Whitney, B. A., Wood, K., Bjorkman, J. E., & Wolff, M. J. 2003, ApJ, 591, 1049
Whittet, D. C. B., Prusti, T., Franco, G. A. P., et al. 1997, A&A, 327, 1194
Wilking, B. A., Meyer, M. R., Robinson, J. G., & Greene, T. P. 2005, AJ, 130, 1733
Wilner, D. J., Bourke, T. L., Wright, C. M., et al. 2003, ApJ, 596, 597
Wilner, D. J., D'Alessio, P., Calvet, N., Claussen, M. J., & Hartmann, L. 2005, ApJ, 626, L109
Wilner, D. J., Ho, P. T. P., Kastner, J. H., & Rodríguez, L. F. 2000, ApJ, 534, L101
Wright, A. E. & Barlow, M. J. 1975, MNRAS, 170, 41
Wurm, G., Blum, J., & Colwell, J. E. 2001, Icarus, 151, 318

Youdin, A. N. & Johansen, A. 2008, in Astronomical Society of the Pacific Conference Series, Vol. 398, Astronomical Society of the Pacific Conference Series, ed. D. Fischer, F. A. Rasio, S. E. Thorsett, & A. Wolszczan, 219

Zinnecker, H., Chelli, A., Carrasco, L., Cruz-Gonzalez, I., & Perrier, C. 1988, Ap&SS, 142, 231

# Publicatielijst

Refereed papers

- *Grain growth across protoplanetary discs: 10μm feature versus mm slope (Chapter 4)*
  **Lommen, D.**; van Dishoeck, E. F.; Wright, C. M.; Maddison, S. T.; Wilner, D. J.; Salter, D. M.; Min, M.; van Langevelde H. J.; Bourke, T. L.; van der Burg, R. F. J., 2009, to be submitted to Astronomy & Astrophysics

- *Resolving structure at millimetre and centimetre wavelengths in the HD100546 disk: Signatures of planet formation*
  Wright, C. M.; Maddison, S. T.; **Lommen, D.**; Wilner, D. J.; Bourke, T. L.; Burton, M. G., 2009, to be submitted to Monthly Notices of the Royal Astronomical Society

- *PROSAC: A Submillimeter Array Survey of Low-Mass Protostars: II. Dense gas in the disks and envelopes of class I protostars*
  Jørgensen, J. K.; van Dishoeck, E. F.; **Lommen, D.**; Hogerheijde, M. R., 2009, to be submitted to Astronomy & Astrophysics

- *Large grains in disks around young stars: ATCA observations of WW Cha, RU Lup, and CS Cha (Chapter 5)*
  **Lommen, D.**; Maddison, S. T.; Wright, C. M.; van Dishoeck, E. F.; Wilner, D. J.; Bourke, T. L., 2009, Astronomy & Astrophysics, 495, 869

- *Probing dust grain evolution in IM Lupi's circumstellar disc. Multi-wavelength observations and modelling of the dust disc*
  Pinte, C.; Padgett, D. L.; Ménard, F.; Stapelfeldt, K. R.; Schneider, G.; Olofsson, J.; Panić, O.; Augereau, J. C.; Duchêne, G.; Krist, J.; Pontoppidan, K.; Perrin, M. D.; Grady, C. A.; Kessler-Silacci, J.; van Dishoeck, E. F.; **Lommen, D.**; Silverstone, M.; Hines, D. C.; Wolf, S.; Blake, G. A.; Henning, T.; Stecklum, B., 2008, Astronomy & Astrophysics, 489, 633

- *SMA observations of young disks: separating envelope, disk, and stellar masses in class I YSOs (Chapter 2)*
  **Lommen, D**.; Jørgensen, J. K.; van Dishoeck, E. F.; Crapsi, A., 2008, Astronomy & Astrophysics, 481, 141

- *Investigating grain growth in disks around southern T-Tauri stars at millimetre wavelengths (Chapter 3)*
  **Lommen, D.**; Wright, C. M.; Maddison, S. T.; Jørgensen, J. K.; Bourke, T. L.; van Dishoeck, E. F.; Hughes, A.; Wilner, D. J.; Burton, M.; van Langevelde, H. J., 2007, Astronomy & Astrophysics, 462, 211

- *Cygnus X-3 and the problem of the missing Wolf-Rayet X-ray binaries*
  **Lommen, D.**; Yungelson, L.; van den Heuvel, E.; Nelemans, G.; Portegies Zwart, S., 2005, Astronomy & Astrophysics, 443, 231

- *RXTE observations of the dipping low-mass X-ray binary 4U 1624-49*
  **Lommen, D.**; van Straaten, S.; van der Klis, M.; Anthonisse, B., 2005, Astronomy & Astrophysics, 435, 1005

Conference proceedings

- *Hot Organic Chemistry in the Inner Part of Protoplanetary Disks*
  Lahuis, F.; van Dishoeck, E. F.; Pontoppidan, K. M.; **Lommen, D.**; Hogerheijde, M. R.; Boogert, A. C. A.; Blake, G. A.; Dullemond, C. P.; Jørgensen, J. K.; Wilner, D.; Kessler-Silacci, J.; Knez, C.; Evans, N. J., 2005, in proceedings of "Protostars and Planets V", eds. Reipurth, B., Jewitt, D., Keil, K. (University of Arizona Press)

- *Investigating Grain Growth in Disks Around Southern T-Tauri Stars at Long Wavelengths*
  **Lommen, D.**; van Dishoeck, E. F.; Wright, C. M.; Jørgensen, J. K.; Bourke, T. L.; Wilner, D. J.; Maddison, S. T.; Hughes, A., 2005, in proceedings of "Protostars and Planets V", eds. Reipurth, B., Jewitt, D., Keil, K. (University of Arizona Press)

# Nederlandse samenvatting

## Introductie: stervorming

De zon is slechts één onbeduidend exemplaar van de circa 200 miljard sterren die onze Melkweg rijk is en de Aarde is één van de acht planeten die hun baantjes rond de zon draaien. Er wordt al duizenden jaren gefilosofeerd over planetenstelsels bij andere sterren. Het heeft echter tot de jaren '90 van de afgelopen eeuw geduurd voordat er daadwerkelijk planeten bij andere sterren gevonden werden. Inmiddels zijn er al meer dan 300 zogenaamde exoplaneten gevonden. De centrale vraag van dit proefschrift is: hoe worden planeten gemaakt? We weten dat planeten een bijproduct zijn van sterren en als we planeetvorming willen begrijpen, zullen we ons ook bezig moeten houden met stervorming. Sterren worden gevormd uit grote interstellaire wolken van stof en gas. Deze kunnen zich onder invloed van de zwaartekracht gaan samentrekken. Binnen de wolk zullen verdichtingen ontstaan, die ieder ook zelf gaan samentrekken, waardoor dichte klompen van stof en gas zullen vormen. Elk van deze klompen kan uiteindelijk een ster of enkele sterren opleveren en op die manier kan één interstellaire wolk de kraamkamer vormen van honderden of duizenden sterren.

In elke wolk en ook in elke klomp is altijd wel wat draaiing oftewel impulsmoment aanwezig. Het is een fundamentele natuurwet dat het impulsmoment behouden moet blijven, net als bijvoorbeeld de totale massa. Als gevolg hiervan gaan klompen die instorten steeds harder draaien. Hetzelfde effect zie je bij een kunstschaatser die een pirouette draait en zijn armen intrekt: die gaat ook steeds sneller ronddraaien. Een ander effect van het behoud van impulsmoment is dat niet alle massa direct naar het centrum kan vallen, waardoor zich een schijf rond de jonge ster zal vormen. Een groot deel van de massa zal door de schijf naar het centrum bewegen en alsnog op de centrale ster terecht komen. Een paar procent van de oorspronkelijke massa blijft achter in de schijf en in die schijf kunnen zich uiteindelijk planeten vormen. Daarom worden deze schijven ook wel protoplanetaire schijven genoemd.

## Stofgroei en planeetvorming

Interstellaire wolken bestaan voor zo'n 99% qua massa uit gas en voor maar 1% uit stof, minieme korreltjes van kleiner dan een micrometer[4] groot. Planeten zoals de Aarde en Mars, met diameters van zo'n 10.000 km, zijn gevormd uit ontelbare deeltjes die oorspronkelijk zo klein waren. We denken dat gasreuzen zoals Jupiter ook een vaste kern hebben van misschien wel tien keer de massa van de Aarde. Hoe komen we van zo klein naar zo groot?

De eerste stap is vooral met computersimulaties bestudeerd en lijkt vrij gemakkelijk te gaan. Deeltjes van kleiner dan een micrometer plakken vrijwel altijd aan elkaar als ze botsen en groeien snel tot deeltjes van een micrometer of tien. De reden dat dit in de interstellaire wolken niet gebeurt, is dat daar de dichtheden veel lager zijn dan in een schijf rond een jonge ster: de deeltjes komen elkaar simpelweg nooit tegen. De volgende stap, van micrometers tot millimeters, centimeters en decimeters, wordt vooral in laboratoria onderzocht. Alhoewel hier groei niet meer vanzelfsprekend is — soms gaan stofdeeltjes kapot als ze botsen — lijkt het er toch wel op dat ook stofklonten van een centimeter of tien vrij gemakkelijk gemaakt kunnen worden.

Als deeltjes eenmaal groter zijn dan, pak en beet, een decimeter, kunnen ze niet langer in een laboratorium onderzocht worden en moeten we weer onze toevlucht nemen tot computersimulaties. Voor deze volgende stap is turbulentie in de schijf — en misschien op sommige plaatsen juist de afwezigheid ervan — van groot belang. Turbulentie zorgt voor dichtheids- en snelheidsverschillen in de schijf en beide zorgen ervoor dat stenen en rotsen weer vaker botsen en samenklonteren. Op deze manier kunnen kilometersgrote embryo's van planeten vormen, waarna de zwaartekracht het overneemt en deze zogenaamde planetesimalen laat doorgroeien brokken zo groot als de maan of zelfs zwaarder dan enkele keren de massa van de aarde.

Er is nog een tweede manier waarop planeten zich kunnen vormen in protoplanetaire schijven. Die manier lijkt veel op de wijze waarop sterren ontstaan uit interstellaire wolken. Het idee is dat lokaal in de schijf weer dichtheidsverschillen ontstaan die op een bepaald moment zo groot worden dat de zwaartekracht het overneemt. Op deze manier kan zich al in een vrij vroeg stadium een planeet beginnen te vormen.

Het lijkt er dus eigenlijk wel op dat we planeetvorming vrij goed begrepen hebben. Alle theoretische modellen moeten echter altijd getoetst worden aan de hand van waarnemingen. Het blijkt dan toch vaak dat de theorie die we gebruiken

[4]Een micrometer = 1 $\mu$m = 0,001 mm.

niet helemaal juist of misschien te simpel is. Zo geven sommige modellen aan dat rotsen van een meter groot in de ster vallen voordat ze groter groeien. Andere modellen voorspellen dat gasrijke planeten veel langer nodig hebben om te vormen dan de tien miljoen jaar die we volgens de waarnemingen beschikbaar hebben. Dit proefschrift houdt zich bezig met de waarnemingen van jonge sterren die nodig zijn om de theorieën en modellen te testen.

## Het waarnemen van jonge sterren

Jonge sterren worden veel bestudeerd met infrarood-telescopen. Een van de redenen dat infrarood en bijvoorbeeld niet zichtbaar licht gebruikt wordt, is dat jonge ster-systemen het helderst zijn bij infrarood-golflengten. Sterker nog, in de fase dat de vormende ster en schijf nog verborgen zijn in een omhulsel, kunnen we het niet eens waarnemen in zichtbaar licht. We gebruiken daarom infrarood-telescopen om het systeem waar te nemen. Het spectrum[5] wordt volledig overheerst door het omhulsel en het systeem wordt wel een klasse I-systeem genoemd, zie bovenaan in Fig. 5.9 op de volgende pagina. Als het omhulsel opgelost en de centrale ster zichtbaar is, spreken we van een klasse II-systeem, in het midden van Fig. 5.9. De laatste fase voordat de jonge ster de volwassenheid bereikt, is de klasse III-fase. Het gas is dan uit de schijf verdwenen, het spectrum wordt gedomineerd door de ster en er is nog slechts een kleine hoeveelheid extra straling in het infrarood afkomstig van de schijf, zoals weergegeven in het onderste deel van Fig. 5.9.

De zogenaamde Lada-classificatie van jonge sterren is niet perfect. Zo komt het geregeld voor dat een systeem waarvan het omhulsel al is opgelost nog wordt geclassificeerd als klasse I. Dit kan bijvoorbeeld komen doordat we van de zijkant naar het systeem kijken en de centrale ster waarnemen door de dichte schijf heen. Afgezien hiervan heeft sowieso elke waarneemtechniek haar voor- en nadelen en een nadeel van infrarood-waarnemingen is dat we er niet alle massa in de schijf mee kunnen zien; in feite zien we alleen het toplaagje ervan. Als we alle massa in de schijf willen waarnemen moeten we naar nog langere golflengten, oftewel het radio-regime. De golflengte van radiogolven varieert van enkele honderden micrometers tot meerdere kilometers. Wij hebben waarnemingen gedaan

[5]Een spectrum laat zien hoeveel licht er van elke golflengte binnenkomt. Het zichtbare spectrum loopt van rood via oranje, geel, groen, blauw en indigo naar violet, de zeven kleuren van de regenboog. Het spectrum loopt daarbuiten nog door naar langere golflengten (infrarood en radiogolven) en aan de andere kant naar kortere golflengten (ultraviolet, röntgenstraling en gammastraling). De zon geeft op alle golflengten licht, maar het meeste in geel en daarom lijkt zij geel.

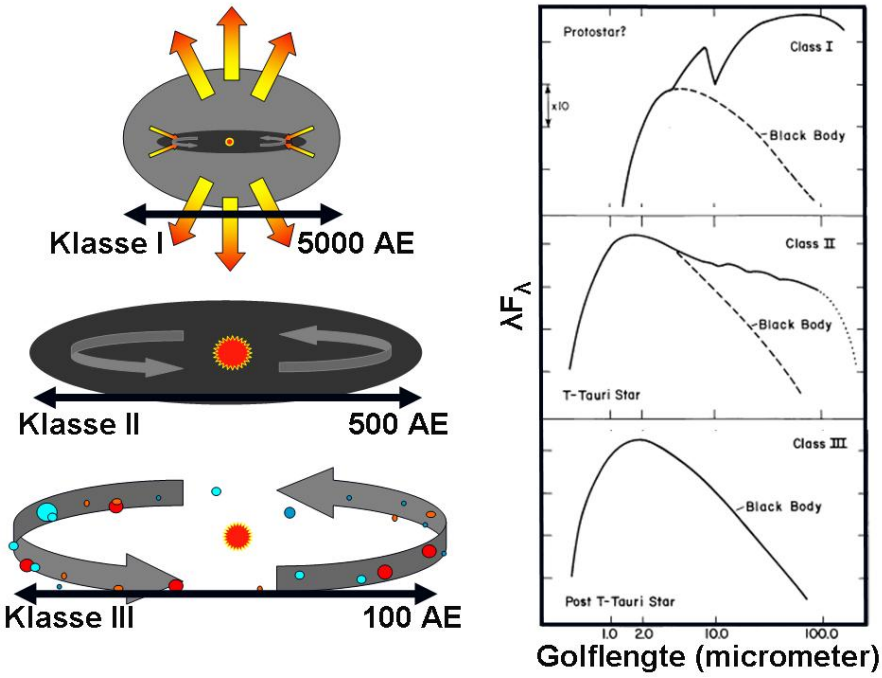


Figure 5.9: Van boven naar beneden zijn hier weergegeven de drie verschillende fasen in het leven van een jonge ster volgens de Lada-classificatie. Links staan schematische tekeningen van de verschillende klassen met een indicatie voor de grootte van het systeem in AE[6]. Rechts staan de bijbehorende infrarood-spectra. *Klasse I*: de vormende ster en protoplanetaire schijf zijn nog omgeven door een omhulsel en het spectrum wordt volledig gedomineerd door dit omhulsel. *Klasse II*: het omhulsel is verdwenen en de centrale protoster is inmiddels zichtbaar. Het infrarood-spectrum wordt echter nog gedomineerd door de schijf van stof en gas die zich rond de jonge ster bevindt. *Klasse III*: het gas is nu uit de schijf verdwenen. Het spectrum wordt gedomineerd door de centrale ster met op de langere golflengten nog wat extra straling afkomstig van de stoffige schijf.

bij golflengtes van ongeveer 1 millimeter tot 6 centimeter.

Voor het werk in dit proefschrift zijn waarnemingen gebruikt van verschillende radio-telescopen, zoals de Submillimeter Array op Hawaii en de Australia

[6]AE staat voor Astronomische Eenheid, de afstand tussen de Aarde en de zon. Deze is 149,6 miljoen km.

Telescope Compact Array in New South Wales. Dit zijn zogenaamde interferometers. Bij een interferometer wordt een aantal telescopen aan elkaar gekoppeld om één grotere telescoop te simuleren, zodat een heel scherp beeld gevormd kan worden. Een extra voordeel van deze radio-interferometers is dat ze omliggende materie kunnen wegfilteren. Ze zijn vooral gevoelig voor structuren op een relatief kleine schaal en dit geeft ons de gelegenheid om in te zoomen op de planeetvormende schijf.

## Dit proefschrift

Zoals gezegd is het centrale onderwerp van dit proefschrift de vorming van planeten in schijven rond jonge sterren. Meer specifiek kijken we naar de eerste stappen van planeetvorming, waarbij stof moet groeien van kleiner dan een micrometer tot millimeters en centimeters. De belangrijkste techniek die daarbij gebruikt wordt, is de radio-interferometrie.

In Hoofdstuk 2 presenteren we waarnemingen van twee klasse I-objecten, gedaan met de Submillimeter Array. De jonge systemen IRS 63 en Elias 29 bevinden zich in het sterrenbeeld Slangendrager, op zo'n 400 lichtjaar van de Aarde[7]. Door onze nieuwe waarnemingen te combineren met waarnemingen van een klassieke schotel-antenne, kunnen we de straling van de schijf en die van het omhulsel van elkaar scheiden en de massa van de verschillende componenten bepalen. Het blijkt dat bij IRS 63 de schijf ongeveer vijf keer zo zwaar is als het omhulsel, terwijl bij Elias 29 juist het omhulsel zo'n zes keer zo zwaar is als de schijf. Elias 29 is dus nog grotendeels verborgen in het omhulsel en IRS 63 is al bijna bij de klasse II-fase aangeland. Door te kijken naar de beweging van het gas in de schijf, kunnen we ook de massa van de centrale ster bepalen. Die bleek ongeveer 0,4 maal die van de zon te zijn voor IRS 63 en zo'n 2,5 maal de massa van de zon voor Elias 29. Hieruit maken we op dat, alhoewel de systemen nog vrij jong zijn, de centrale ster bijna zijn uiteindelijke massa heeft bereikt.

In 2005 hebben we vijftien jonge sterren, verdeeld over de sterrenbeelden Kameleon en Wolf, waargenomen met de Australia Telescope Compact Array. De vijf sterren in het sterrenbeeld Wolf hebben we bovendien nog waargenomen met de Submillimeter Array. Deze waarnemingen worden gepresenteerd in Hoofdstuk 3. We combineren deze waarnemingen met gegevens uit de literatuur om het spectrum van de systemen bij lange golflengten te bepalen. We vinden hieruit

[7]Een lichtjaar is de afstand die licht in een jaar aflegt. Licht reist met zo'n 300.000 km/s, dus 1 lichtjaar komt overeen met ongeveer 9.500.000.000.000 kilometer, ruim 60.000 keer de afstand tussen de Aarde en de zon.

dat zich in een groot deel van de schijven een flinke hoeveelheid stof moet bevinden dat al gegroeid is tot zeker enkele millimeters. Voor ongeveer de helft van de bronnen die we met deze radio-telescopen hebben waargenomen bezitten we ook infrarood-waarnemingen, waarmee we het warme toplaagje van het binnenste deel van de schijf kunnen bestuderen. Er lijkt een verband te zijn tussen de verschillende waarnemingen en dus ook tussen tussen de twee verschillende gebieden in de schijven die we bestudeerd hebben. Dit kan erop wijzen dat stofgroei in protoplanetaire schijven snel moet plaatsvinden.

Om het verband dat we in Hoofdstuk 3 hebben gevonden te controleren, hebben we een grotere groep klasse II-sterren waargenomen met vier verschillende radio-interferometers en met de Spitzer Space Telescope. Deze waarnemingen hebben we bovendien nog samengevoegd met gegevens uit de literatuur om dezelfde informatie voor zo veel mogelijk bronnen te krijgen. Op deze manier hebben we het verband tussen de infrarood- en de millimeterwaarnemingen kunnen bevestigen, zoals uiteengezet in Hoofdstuk 4. Om dit verband te kunnen verklaren, hebben we diverse computer-simulaties uitgevoerd. De waarnemingen lijken erop te wijzen dat er erg veel turbulentie in de schijf aanwezig is, meer dan oorspronkelijk gedacht werd. Stofgroei vindt namelijk vooral in het koude binnenste van de schijf plaats, want daar zijn de dichtheden het grootst. We zien de grotere deeltjes echter vrijwel direct aan het oppervlak van de koude binnenschijf. Uit onze waarnemingen en modelleerwerk maken we verder nog op dat de evolutie zich in het ene stervormingsgebeid sneller lijkt te voltrekken dan in het andere.

In het vijfde en laatste hoofdstuk presenteren we waarnemingen van de Australia Telescope Compact Array op golflengten van 7 mm en langer voor drie jonge systemen. Voor de systemen WW Cha en RU Lup hadden we vanuit ons werk in Hoofdstuk 3 al duidelijke aanwijzingen dat er stof van een millimeter of groter aanwezig moet zijn. CS Cha is een dubbelster-systeem met daaromheen een schijf van stof en gas. Voor alledrie de systemen zien we ook op 7 mm nog straling afkomstig van stofdeeltjes, wat betekent dat het stof al gegroeid moet zijn tot meerdere centimeters. We zien hier dus eigenlijk kiezelstenen in schijven rond jonge sterren op honderden lichtjaren afstand! WW Cha is ook nog gedetecteerd bij een golflengte van 3 cm en RU Lup zelfs nog bij 6 cm. Uit ons onderzoek blijkt echter dat deze straling niet meer van stof afkomstig is. Misschien is het het gevolg van magnetische activiteit op het oppervlak van de jonge sterren of van winden van geladen deeltjes die door de systemen worden uitgezonden. Om dit nieuwe probleem op te lossen zouden we de systemen met een nog grotere scherpte moeten waarnemen en daarvoor zouden we dan telescopen op verschillende continenten met elkaar moeten verbinden.

# Curriculum vitae

Op 11 februari 1977 werd ik geboren in het Limburgse Grubbenvorst. Op twaalfjarige leeftijd ging ik naar het Thomascollege. Niet veel later begon ik bij Festina met atletiek. In 1994 nam ik deel aan een sterrenkunde-zomerschool in Dwingeloo onder leiding van Dr. Walter Jaffe. In datzelfde jaar begeleidde Carel van Nisselroij mij naar het Zuid-Nederlands Kampioenschap op de 5000 meter.

Na het vwo-examen leek het universiteitsleven niet voor mij weggelegd en in januari 1996 begon ik als administratief medewerker bij TIP Trailer Rental BV. Daarnaast deed ik een part-time studie Informatica aan de Open Universiteit. Na twee jaar volgde een full-time baan als systeembeheerder bij Origin in Eindhoven en liep ik in Rotterdam mijn eerste marathon in 2:48. In 1999 begon ik alsnog met een voltijds studie aan de Universiteit van Amsterdam. De propedeuses Wiskunde en Natuurkunde en ook het kandidaats Natuurkunde behaalde ik *cum laude* om vervolgens te beginnen aan de Master Sterrenkunde. Prof. Dr. Rens Waters liet me kennismaken met de observationele sterrenkunde en stuurde me op waarneemreizen naar La Palma en Mauna Kea. Mijn eerste echte wetenschap deed ik onder begeleiding van Prof. Dr. Michiel van der Klis en Drs. Steve van Straaten aan "the dipping low-mass X-ray binary 4U 1624-49." Mijn afstudeeronderzoek was onder begeleiding van Prof. Dr. Ed van den Heuvel en Dr. Lev Yungelson aan "Cygnus X-3 and the problem of the missing Wolf-Rayet X-ray binaries." In mijn laatste jaar als student coachte Bram Wassenaar mij naar een tijd van 2:40 op de Amsterdam Marathon.

In april 2005 begon ik aan een promotie-project aan jonge sterren onder begeleiding van Prof. Dr. Ewine van Dishoeck in Leiden. Ik deed waarnemingen op Hawaii en in Australië en werkbezoeken en conferenties brachten mij naar Engeland, Frankrijk, Portugal, Massachusetts en Californië. Tijdens mijn promotie begeleidde ik het college Interstellar Medium, assisteerde ik bij het Pre-University College en organiseerde ik zeven ISM/CSM-meetings. Daarbuiten was ik nog actief als docent aan de Weekendschool en als coördinator van de Brainpower-klas. In 2008 voltooide ik mijn eerste volledige triatlon op het eiland Elba.

Na mijn promotie zullen mijn vrouw Cara en ik verhuizen naar Singapore. Ik hoop mij daar bezig te houden met het overbrengen van kennis op de volgende generatie. Mijn sportieve uitdaging is om nog eens deel te nemen aan de Kona Ironman op Hawaii.

# Nawoord

Zonder de hulp van velen had ik deze promotie nooit tot een goed einde kunnen brengen. Ik ben erg blij dat ik de kans heb gekregen om dit project te doen en dat ik ook steeds gesteund ben, ook al ben ik geregeld de moed en mijn geduld verloren. Rens, Michiel en Ed, zonder jullie was ik er misschien wel nooit aan begonnen!

To all the staff in Narrabri and on Mauna Kea I would like to say: keep up the good work! Jes, Tony, David, Tyler, Stuartt, Michiel, Joanna, Demerese, Stephen, and Fred without your help I would never have been able to reduce all those ATCA, SMA, OVRO, CARMA, VLA, and Spitzer data. Kirsten, Anita, Liesbeth, Jeanne, David, Tycho, Erik en Aart, jullie hebben mijn werk op de Sterrewacht mogelijk gemaakt. To all the students, postdocs, and professors: you made it fun. In that context I would especially like to mention all the people of the AstroChem Group. There are too many of you, so I will not try to name you all, since I would be sure to miss a few. Ik heb ook aardig wat kamergenootjes gehad over de afgelopen vier jaar. Saskia, Vincent, Floor, Stefan, Jeanette en Remco, het was erg gezellig! Chris, your wisdom still has a prominent place on my wall. Sarah, it was a pleasure to work with you. Lars, Jort, Richard, Ruud, Remco, and Vincent, your proof readings were very useful and to whom it may concern: both swimming and playing table tennis helped tremendously in lowering my blood pressure!

Lest best. Pap en mam, jullie hebben me altijd gesteund en ik heb de dingen die ik bereikt heb voor een groot deel aan jullie te danken. En lieve Cara, jij bent het allermooiste dat ik aan deze promotie heb overgehouden. Wo ai ni! ;-)

*Das Verstehen kommt immer erst nach dem Ärgernis*